THE UNIVERSITY *of* EDINBURGH

UNIVERSITY OF EDINBURGH

Measuring energy levels in bacterial dormancy

Leonardo Mancini

A thesis submitted in fulfillment of the requirements
for the degree of Doctor of Philosophy

in the

February 3, 2020

Abstract

Bacteria are evolving strategies to survive antibiotic treatments at a pace that is not matched by the one at which new drugs are discovered. Beyond the more notorious antimicrobial resistance, other survival mechanisms such as tolerance and persistence are today thought to play a major role in infections. Whether resistant, tolerant or persistent, cells that stop growing seem to have a survival advantage over replicating ones. These cells are conventionally referred to as dormant and very little is known about their physiology and the mechanistic reasons behind their remarkable survival capabilities. Because cell growth is intimately linked to cell physiological traits such as energy availability, this work seeks to investigate cellular energetics at the single cell level using *E. coli* as a model system. In particular the focus is addressed to two of the most important energy parameters in all life forms: ATP concentration and proton motive force (PMF).

The PMF, further than participating in ATP synthesis, fuels a number of cellular processes that play prominent roles in cellular homeostasis. Regulation of each of its two components, the pH difference across the plasma membrane and the membrane voltage, is in turn essential for cell survival. Because cytoplasmic pH can be assayed at the single cell level with the genetically encoded fluorescent sensor pHluorin and PMF as a whole can be quantified from bacterial flagellar motor speed, the focus of this work was first addressed to membrane voltage estimation techniques. Nernstian reporters have in the past been used for the purpose, but their characterization never reached the depth of detail necessary for the measurement of membrane voltage of cells in physiological conditions. Using both an experimental and mathematical approach, I explored and described the parameter landscape in which these reporters can be used as sensors and when instead they influence cell physiology. Having built and validated such a preliminary interpretative framework, I formulated an algorithm for the characterization of novel dyes with respect to their interactions with the physiology of the cell. I applied the workflow to the characterisation

of a Nernstian dye that had never been used before in *E. coli*. Although, in my conditions, none of the Nernstian dyes available were found suitable for (Vm) estimation, the workflow I developed is in the position to offer a simple and robust method to benchmark novel dyes and test the results obtained with old ones.

ATP dynamics represent another fundamental aspect of cellular energetics and measurements at the single cell level have been sought for more than a decade. The most promising approach published suffered of low signal intensities that were not compatible with the exposure times required for time series measurements. By optimizing sensor expression and performing structural modifications, I obtained improvements in the signal intensity which rendered the sensor available to time lapse measurements. To further improve signal-to-noise ratio I installed a laser in our custom-built microscope.

Coupling the ATP sensor with measurements of bacterial flagellar motor speed, which correlates to PMF, and the pH sensor pHluorin, I could investigate the main energy parameters of *E. coli* cells in vivo, in real time and with single cell resolution. To study these physiological traits in dormant cells I first established a definition of dormancy that lies on simple axioms such as viability and growth halt. I then individuated conditions capable to sharply induce dormancy, such the presence of bacteriostatic antibiotics, quorum sensing molecules or starvation.

Opposed to the classical view that sees dormancy as an energetically poor state, my results show that the observation of growth arrest alone is scarcely informative on the physiological state of the cell. Dormant cells can be both high and low in energy, depending on the conditions that induced growth halt. While highly energetical cells might be better suited at surviving antibiotics via active means, scarcely energetical ones might have less targets to offer to antibiotics to carry out their function. In any of these scenarios, this work suggests that the environmental cues that lead to dormancy are likely to dramatically alter bacteria's susceptibility to the different antibiotic classes.

Lay summary

Bacteria, like many other organisms, can survive the challenges that the environment presents them by stopping growth and entering in an energy-saving state known as dormancy. This strategy is also very efficient against the current antibiotic treatments and some evidence indicates that it may play a role in the acquisition of antimicrobial resistance. Despite the worldwide antibiotic crysis and the high clinical relevance of dormancy, very little is known about its physiology. In this work I address this knowledge gap by focusing on energetics. Energy is indeed necessary to the maintenance of all life forms - the curious reader can learn more about it in the classic "What is life?" by Erwin Schrödinger - and a lack of energy sources is one of the environmental signals that are capable of inducing dormancy. Here, I ask questions such as: do dormant cells store energy? Do all dormant bacteria share the same energetic traits no matter the environment? To address these questions, I first develop and optimise a set of sensors of cellular energy. I then use them to assay the energy levels of cells that have gone dormant in response to different environmental cues. The results show that the reasons that induced dormancy matter. In facts, in some conditions, dormant cells are energetically seemingly undistinguishable from growing ones, in others, they show different degrees of energy loss. Interestingly, depending on the specific molecular mechanism, antibiotic accumulation in the cell can be both increased and decreased by high energy levels. While future work will verify the association between a particular molecular mechanism, the energetic state of a cell and survival to antibiotics, the results I present in this work lay the ground for a deeper understanding of the physiological reasons allowing antibiotic survival during dormancy.

Declaration

Except where otherwise stated, the research undertaken in this thesis was the work of the author. Where work was done in collaboration with others, a significant contribution was made by the author. Collaborative work is indicated as such at the beginning of the relevant section. Appropriate credit has been given within this thesis where reference has been made to the work of others. The work has not been submitted for any other degree or professional qualification.

Leonardo Mancini,
February 3, 2020

Acknowledgements

My gratitude goes to my mentor Teuta for her wisdom, support and contagious excitement for scientific problems. Thanks also to the present and past members of her lab, versed in many of the things I was not and willing to share their knowledge. I am grateful to Meriem and the members of her lab for useful discussions, to Alex and to Sophie for help with proofreading the manuscript. Lastly, I am thankful to my parents Antonella and Gianni, to whom this work is dedicated.

List of abbreviations

ABC	ATP-binding cassette
ADP	Adenosine diphosphate
AMP	Adenosine monophosphate
ATP	Adenosine triphosphate
BFM	Bacterial flagellar motor
BRET	Bioluminescence resonance energy transfer
CW	Clockwise
CCW	Counterclockwise
DC	Direct current
DNA	Deoxyribonucleic acid
$DiBAC_4(3)$	Bis-(1,3-Dibutylbarbituric acid) trimethine oxonol
$DiSC_3(5)$	3,3′-Dipropylthiadicarbocyanine iodide
EGFP	Enhanced green fluorescent protein
EMCCD	Electron multiplying charge-coupled device
FRET	Fluorescence resonance energy transfer
GTP	Guanosine triphosphate
LB	Lysogeny broth
LED	Light emitting diode
MATE	Multidrug and toxic compound extrusion
MDK	Minimum duration of treatment for killing
MFS	Major facilitator superfamily
MIC	Minimum inhibitory concentration
MNC	Maximum non-inhibitory concentration
NMR	Nuclear magnetic resonance
OD	Optical density
PI	propidium iodide
PBMH	Potassium benzoate methyl hydroxide
PMF	Proton motive force
RBS	Ribosome binding site
RDM	Rich defined medium
RNA	Ribonucleic acid
RND	Resistance/nodulation/division
RPM	Revolutions per minute
SMR	Small multidrug resistance
TA	Toxin-antitoxin
ThT	Thioflavin T
TMRM	Tetramethylrhodamine, methyl ester
V_m	Membrane voltage
WT	Wild-type

Contents

Chapter 1

Introduction

1.1 Microbial survival to antibiotics

Microbes live in communities often made up of different species. Limited amounts of substrate make their habitats highly competitive, prompting the evolution of a number of fitness enhancing strategies (Stubbendieck et al., 2016). Some microorganisms, for example, are capable of outcompeting others by synthesising toxic substances like antibiotics. Competitors that are susceptible to these agents undergo a strong selective pressure and mutants that present defensive traits, such as antibiotic resistance genes, experience an advantage and undergo fixation. This in turn applies a selective pressure on the antibiotic producing species in what can be considered an arms race. Since the discovery of penicillin in 1929 (Fleming, 1929), antibiotics have proven an invaluable ally against bacterial infections and are today frequently used in clinical contexts and in food production (Schwarz et al., 2001; Graham et al., 2007; McManus et al., 2002). As it happens in the framework of community interactions however, the selective pressure imposed by antibiotics facilitates fixation of resistant mutations. The rapid emergence of such genotypes bears forebodings of a possible return to a pre-antibiotic era and therefore requires urgent countermeasures, such as stricter regulation of antibiotic usage (Cars et al., 2008).

Survival of antibiotic treatments, however, is not only an outcome of resistance. Research carried out following global concerns on antibiotic uneffectiveness has uncovered two further survival mechanisms: tolerance and persistence. Because the three categories eventually yield the same result, the survival of a microbe to antibiotics, the individuation of their hallmarks and definitions are subject of intense debate (Kim et al., 2016; Brauner et al., 2016;

Balaban et al., 2019).

1.2 Resistance

Antibiotic resistance is probably the best defined of the three phenomena. Resistant microbes are different from the susceptible ones because they carry advantageous mutations in their DNA, such as genes encoding for enzymes that can digest the drug or for slightly different drug targets that are less likely to bind the antibiotic. Importantly, these mutations allow the cell to cope with higher concentrations of drug. The standard to assay microbial survival depending on antibiotic concentration is the minimum inhibitory concentration (MIC). The MIC is the minimum concentration of drug necessary to totally stop microbial growth. Resistant mutants can cope with higher drug concentrations and therefore have a higher MIC (Brauner et al., 2016).

1.3 Tolerance and persistence

In contrast to resistant cells, tolerant and persistent cells have the same MIC as susceptible cells, but they differ in the length of treatment they can survive. The difference between tolerance and persistence is subtler, the two terms are often used interchangeably and this has caused even further debate (Kim et al., 2016). The element that perhaps most contributes to the confusion is the fact that microbes undertaking the two strategies seem to share the same macroscopical hallmark: a reduction of the growth rate. Because most bacteriolytic antibiotics target replicating cells, for example by perturbing DNA replication or cell wall synthesis, slow growing or non-growing cells are more suited to surviving treatments, as they offer less drug targets and these are less essential. The most widely accepted distinction between persister and tolerant cells is made on the grounds of the shape of their antibiotic killing curves. While the curve is unimodal for tolerant cells, it is bimodal for persisters (Fig. 1.1), the underlying idea being that persister cells arise from phenotypical heterogeneity (Brauner et al., 2016). According to the current view, persisters are tolerant cells that have been generated in a context of phenotypical heterogeneity (Balaban et al., 2019).

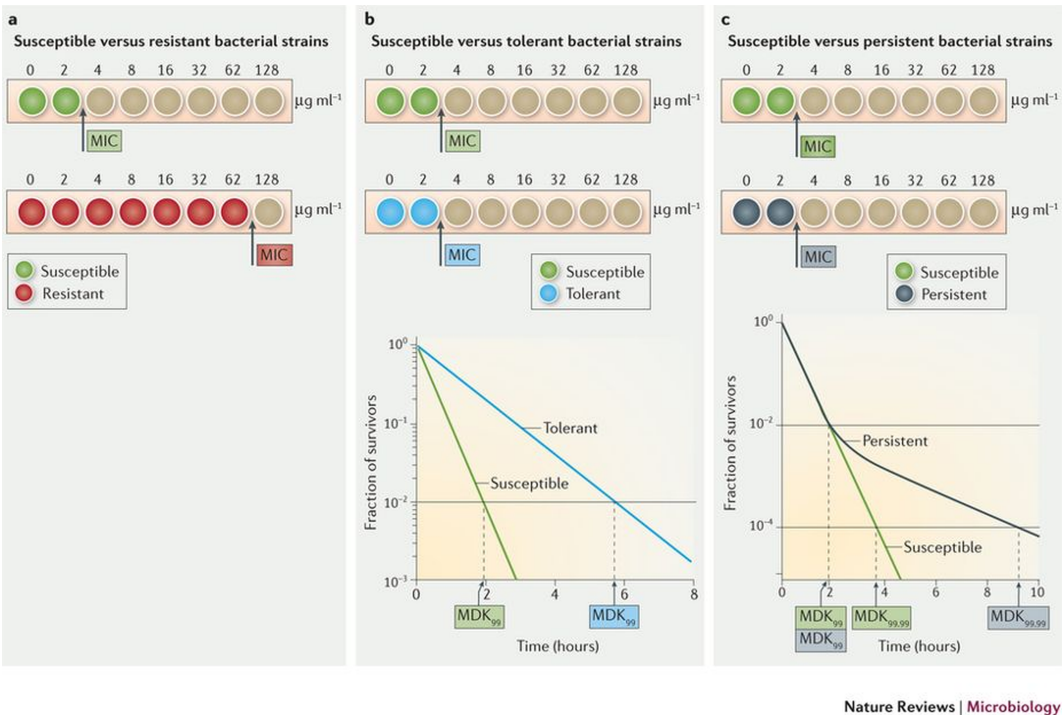

FIGURE 1.1: Drug response of resistant, tolerant and persistent bacteria. a) Resistant bacteria grow and survive at antibiotic concentrations above the MIC. b) Tolerant and susceptible strains are equally affected by the concentration of antibiotic, but tolerant bacteria can withstand the presence of the drug for longer. The minimum duration of treatment for killing 99% of their population (MDK_{99}) is indeed longer. c) Persisters are a subgroup of the population. The killing curve of a population with persisters initially resembles that of a fully susceptible one. When the susceptible subopulation has been killed, persisters start appearing in the killing curve, because, like tolerant bacteria, they can sustain the treatment for longer as indicated by the longer MDK. In this example, the MDK of persisters is $MDK_{99.9}$, remarking that persisters are often only a subpopulation of small size. The image is from (Brauner et al., 2016).

1.4 Phenotypical heterogeneity in bacteria

Bacteria are unicellular organisms that replicate by binary fission. Because of their relatively low mutation rate (1x10^{-3} per genome per generation (Lee et al., 2012)) the monoclonal division of a single bacterial cell tends to give rise to a population of genotypically identical individuals. Organisms can survive in a range of conditions without the need to alter their genotype. Such capability arises both from the fact that phenotypes are relatively robust meaning they can function across a certain spectrum of conditions and from the fact that the same genotype can give rise to multiple phenotypes that cells can adopt in

response to environmental changes. Therefore, all life forms capable of adaptation are capable of attaining phenotypical heterogeneity in heterogeneous environments. Interestingly, bacteria can attain such heterogeneity also in homogeneous environments through various molecular mechanisms (Ackermann, 2015). The sphero-cylindrical *E. coli*, for example, divides by forming a septum across its long axis, giving rise to two cells of very similar size (Macara et al., 2008). Despite the geometrical symmetry, such strategy yields some functional asymmetry. Indeed each cell inherits a newly formed pole at the septum and an old pole from the mother. After some divisions a population is thus made up of a mix of cells having a freshly made pole and a variably old one (Macara et al., 2008). Studies have shown that the age of the pole can alter a cell's phenotype, because, for example, protein aggregates (Lindner et al., 2008) and multidrug efflux pumps (Bergmiller et al., 2017) tend to accumulate in cells bearing the older poles. Such asymmetries originating at the time of cell division are sometimes referred to as biased segregation. This mechanism is at the basis of phenotypical heterogeneity in cell lineages not just in *E. coli*, but in a variety of organisms, including multicellular ones (Macara et al., 2008).

Another source of phenotypical heterogeneity is stochasticity in cell processes. Many cellular reactions involve molecules present in low numbers, which are particularly prone to stochastic fluctuations (Elowitz et al., 2002). These variations in abundance can be amplified by genetic circuits such as positive feedback loops, eventually resulting in the establishment of different phenotypes. While the precise regulation of genetic circuits is a desirable property, a certain amount of noise in the pathway leading from genotype to phenotype is thought to be advantageous (Ackermann, 2015). This indeed allows the undertaking of so called bet-hedging strategies, in which part of the fitness in optimal conditions is sacrificed to increase survival chances in sub-optimal ones (Ackermann, 2015). In the classic bet-hedging scenario, two phenotypically different subpopulations can be distinguished. One specializes in maximising yield and is highly competitive for resources, the other specializes in stress survival. Bet-hedging can be seen as a form of prevention and is particularly important in rapidly fluctuating environments in which adaptation cannot be performed fast enough (Ackermann, 2015). One interesting and highly debated mechanism bacteria are thought to use to activate bet-hedging strategies encompasses toxin-antitoxin (TA) modules and may rely on gene circuit noise (Balaban et al., 2004). TA modules are small gene circuits that encode

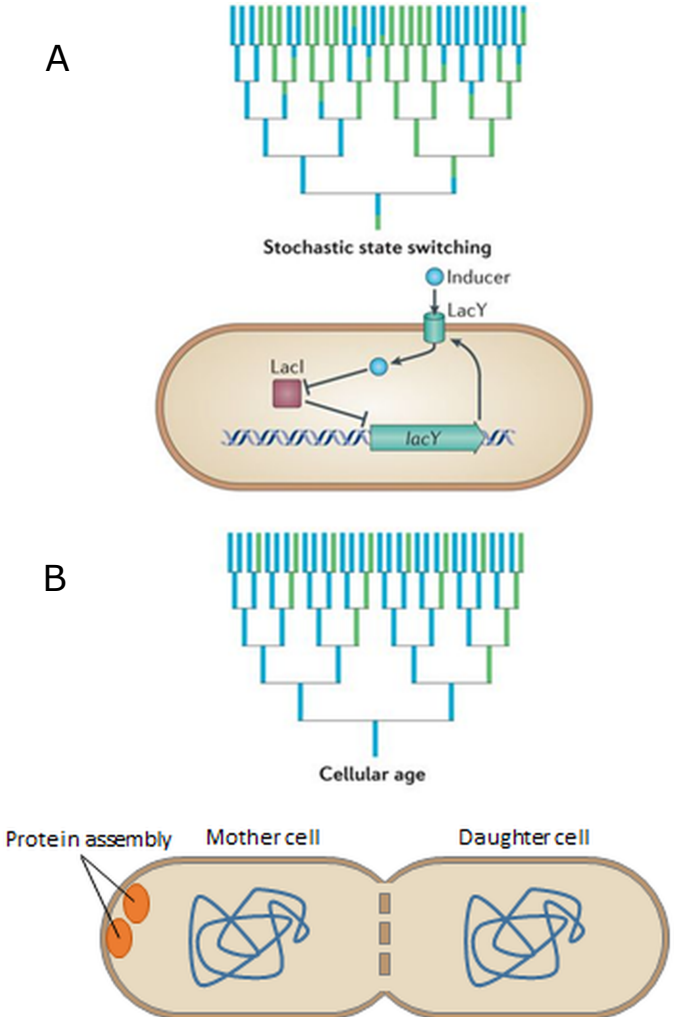

FIGURE 1.2: Cartoon explanation of some of the mechanisms of phenotypic heterogeneity involved in persistency. In these examples, lineage trees originate from one founder cell and produce two different phenotypes indicated in blue and green. a) stochasticity in gene expression at the level of the promoter, exemplified by the lactose utilization system. Increased expression of the importer LacY, increases the concentration of the inducer, which inhibits the repressor LacI producing a positive feedback loop that increases LacY expression. b) phenotypic heterogeneity due to cellular age exemplified by the asymmetric distribution of a protein assembly at one of the mother cell poles. Upon cell division, the mother cell retains the assembly while the daughter does not. The image was adapted from (Ackermann, 2015).

for a protein toxin that interferes with certain cell functions, and an antitoxin (an RNA or a protein). Their first discovery was in the context of plasmid maintenance (Gerdes et al., 1986). In the absence of specific selective pressure,

plasmids can get lost during cell replication. Certain plasmids however encode for TA modules in which a stable toxin is accompanied by an unstable antitoxin that is rapidly degraded. Because upon division daughter cells inherit cytoplasm containing the toxin, their survival depends on whether they also inherit the generic material to produce the antitoxin (Gerdes, 2000). However, it was also proposed that the concentrations of toxin and antitoxin could undergo some stochastic fluctuations and thereby have a role in producing phenotypical heterogeneity. Coherent with this vision, mutations increasing the toxin's effectiveness and decreasing the antitoxin's have been seen to increase persister appearance rate (Aakre et al., 2013). A large number of TA modules has been found in *E. coli* and several different molecular mechanisms identified. The fact that they target distinct vital cellular processes and functions, such as replication, translation, cell wall biosynthesis and membrane integrity (Page et al., 2016) supports the idea that the persistent phenotype is a multifaceted phenomenon even when heterogeneity is obtained via the same overarching mechanism. Although conceptually and in several cases experimentally plausible, the importance of the role of TA's in persistence is debated (Goormaghtigh et al., 2018).

1.5 Drug tolerance in persister cells

Several mechanisms of drug tolerance have been described. Increases in multidrug-efflux pumps expression are linked to tolerance, because they result in lower antibiotic levels (Lee et al., 2010; Amini et al., 2011). Reduced respiration rates (Amini et al., 2011) are thought to limit aminoglycosidic antibiotic uptake, although the exact mechanism by which these drugs are imported is not fully understood (Taber et al., 1987). Prolonged lag times (Fridman et al., 2014) and dormancy or slow growth (Helaine et al., 2010) enable survival because many antibiotics are scarcely effective against non-proliferating microbes. Interestingly, the same mechanisms are also thought to be behind the survival of persisters (Pu et al., 2016; Allison et al., 2011; Balaban et al., 2004) which suggests that treatments that are effective against tolerant microbes may also kill persistent ones. In a definition that clearly summarizes the similarity between tolerant and persistent bacteria in the context of drug survival mechanism, persister cells can be defined as heterotolerant (Balaban et al., 2019). The

word was coined in accordance with the term heteroresistant, used to describe cells which are only transiently resistant to antibiotics because of DNA changes highly likely to revert (Nicoloff et al., 2019). Persisters are therefore cells which are only transiently tolerant to antibiotics. While tolerance can be genotypically acquired, persistence, by definition, cannot. Therefore eliminating persistent bacteria should potentially be easier than killing tolerant ones, because their antibiotic surviving state is only transitory. Indeed, it has been shown that administering nutrients to dormant persister cells allows their eradication with antibiotics that are commonly effective against replicating ones (Allison et al., 2011).

1.6 Dormancy

Whether tolerant or persistent, bacterial cells with a reduced or zero growth rate seem to have an advantage over fast replicating cells in terms of survival to the most common bactericidal antibiotic classes. In nature, suspended growth is often a synonym of extreme survival strategies. Depending on the organism considered, terminology varies substantially. In bacteria, an extreme state of reduced growth in which cells are viable but are not replicating is defined interchangeably as dormancy or quiescence. Environmental bacteria that do not grow on synthetic medium but stay viable are sometimes called unculturable (Lewis, 2006). Some bacteria are also capable of a process called sporulation, which through an asymmetric division produces a specialized, highly stress resistant and metabolically inactive body: the spore (Rittershaus et al., 2013). Growth and metabolism slow down in periods of stress are also common in superior organisms. Plants, as particularly evident in deciduous ones, enter into a winter rest when environmental conditions start indicating the approaching of the cold season. During the winter rest, growth of most plant parts and cambial activity are reduced as classically shown by growth rings (Perry, 1971; Srivastava, 1973). Many endotherm animals are also capable of periods of hibernation, characterised by reduced energy requirements and metabolism. The opportunistic use of this strategy allows them to adapt their foraging needs to environmental conditions (Geiser, 2011). Despite the vast array of organisms using growth arrest as a response to stress, the mechanisms by which such

a physiological state enables survival broadly boils down to two strategies: avoidance and resources reallocation.

In the case of bacteria, dormancy is a particularly effective avoidance strategy against some of the major antibiotic classes, because these tend to target processes which are essential during cell growth. Fluoroquinolones for example inhibit DNA topoisomerases which are needed during DNA replication (Blondeau, 2004) while β-Lactam antibiotics (penicillins, cephalosporins and vancomycin) inhibit cell wall synthesis (Drawz et al., 2010). When growth is suspended, the production of new cell wall or DNA ceases and therefore the molecular targets of these drugs become non-essential. During growth, the production of new biomass is heavily reliant on ribosomes. In *E. coli*, in balanced growth conditions at 37°C in minimal glucose medium, for example, more than half of the cellular dry weight is made up of proteins, while the RNA content, most of which is used to make up ribosomes (Bremer H, 2008), amounts to one fifth (Neidhardt et al., 1990). Because the ribosome pool has limited size and its protein production has a limited rate, cells have to make decisions regarding the composition of their proteome. In fast replicating cells, an important portion of the total ribosomes is used to double protein content (Scott et al., 2014). When growth is halted, such portion can be reallocated for the production of stress resistance molecules.

Both in the case of stress avoidance and in the case of resource reallocation, timing is key. While cells can remain dormant for long periods, antibiotic treatments in clinical settings are hard to perform for extensive periods of time because of their side effects and increased risk of evolving resistance. When treatments are intermittent and produce a fluctuating environment instead, bacteria demonstrated the capability to evolve suitable dormancy lengths that matched treatment times (Fridman et al., 2014). Because dormant cells are hard to treat, one potential approach is waking them up before antibiotics are administered (Allison et al., 2011). However, the time of growth resumption of dormant cells is notoriously variable (Pin et al., 2008; Niven et al., 2008; Vulin et al., 2018). In addition, as seen previously, not all bacteria enter into dormancy in response to environmental stimuli, but they can stop growing because of internal stimuli such as toxins or waste products accumulation.

While significant efforts have been devoted to the study of bacterial exit from dormancy, only a limited number of works have focused on the entrance

into such a condition and on the characterization of its physiology. The investigation of these questions is potentially promising. Knowing the conditions that induce growth arrest could for example be important in preventing their realization, while knowledge of the physiology that accompanies growth arrested states could be helpful for the individuation of dormancy-specific drug targets. Studies that attempted to investigate the entrance of cells into an antibiotic tolerant condition have had mixed results. Some of the most important contributions came from Natalie Balaban and colleagues, that showed the mechanism of acquisition of certain genetically enabled drug tolerances (Levin-Reisman et al., 2017) and proposed a mechanism for the acquisition of persistence Balaban et al., 2004. Others, that proposed a general model for the acquisition of persistence through TA modules via the mediation of the stringent response, were instead less successful (Maisonneuve et al., 2011; Maisonneuve et al., 2018; Germain et al., 2015; Ramisetty et al., 2016; Harms et al., 2017), perhaps suggesting that more than one pathway exists. Evidence of the mechanisms behind viability maintenance of growth-halted cells is scant. *E. coli* dormant cells are thought to maintain protein synthesis for a certain amount of time after growth stops (Gefen et al., 2008) and to possess significantly altered cytoplasm dynamics (Parry et al., 2014), while *M. tubercolosis* is believed to maintain its cellular energetics by rearranging its lipid metabolism during dormancy (Raghunandanan et al., 2019). Such a knowledge gap regarding the maintenance of viability in non-growing conditions also leads to misinterpretations of experimental results. One of the best known of these is the erroneous assumption that dormant cells resume growth quickly after favourable conditions arise. Instead, cultures grown from an initial inoculum of stationary phase cells, require an appropriate number of dilutions or subculturing before carry over dormant cells disappear (Wood et al., 2013; Brauner et al., 2016; Kim et al., 2016). This is important for example, when one attempts the estimation of persister cell frequencies (Orman et al., 2013).

Finally, dormancy states of extreme length, despite being of lower clinical interest, have enjoyed some popularity and should be noted. Cells with such phenotype are sometimes called viable but non-culturable (VBNCs) and are thought to be at the edge between life and death. Whether these cells are capable of resuming growth and cause infections is debated, as well as whether their entrance into such state is due to irreparable molecular damage or to a precise cellular program (McDougald et al., 1998; Mukamolova et al., 2003;

Kell et al., 1998). Their physiology is intriguing as it challenges our definition of life.

1.7 The energetics of antibiotic survival

Dormant bacteria can reallocate the resources that would otherwise be used for growth, towards stress resistance mechanisms. This probably has profound effects on the cellular metabolism. The key to understanding antibiotic survival due to tolerance could therefore be in cellular energetics. Indeed at least in certain conditions, there seems to be an association between reduced intracellular ATP concentration and physiological states that enable antibiotic survival (Shan et al., 2017; Conlon et al., 2016; Cameron et al., 2018). The fact that some reports fail to observe such association (Leszczynska et al., 2013; Braetz et al., 2017; Svenningsen et al., 2019) might however be symptomatic that the mechanism is more complicated than a simple direct regulation of physiology by ATP or that more than one mechanism exists. Energetics, in the form of proton motive force (PMF) for example, regulate a vast array of cellular processes that could potentially be involved in antimicrobial survival. Some examples are multi-drug efflux pumps, which are fuelled by PMF or ATP, and that are actively involved in the control of cytoplasmic antimicrobial concentration (Anes et al., 2015) or membrane voltage (V_m), which is thought to enable aminoglycoside antibiotics uptake (Davis, 1987). Knowledge concerning the energy maintenance and usage of dormant bacteria is therefore of paramount importance to grasp the reasons of their antibiotic survival capabilities.

1.8 ATP

The maintenance of life relies on endergonic reactions, that is reactions in which the free energy of the products is higher than that of the reactants. Because of this energy gap, endergonic reactions are not spontaneous and their occurrence depends on the coupling with exergonic ones, in which reactants are more energy-rich than the products. To fuel the endergonic reactions needed to make up the building blocks of life, certain organisms take direct advantage of the exergonic reactions occurring in nature, such as the fusion of hydrogen nuclei in the sun that yields photons, and are called phototrophs.

Others harvest energy by processing molecules in the environment and are called chemotrophs. In all life forms, these primary energy-producing reactions are often not directly coupled to the final energy-requiring ones necessary for anabolism. Instead energy is temporarily stored in mediator molecules. These can then be sent to the various cellular districts effectively serving as an energy-currency. This has several advantages. From a spatial point of view, it allows compartmentalisation and specialization because energy can be produced in one district and used in another one. From a temporal point of view, it allows the desynchronization of catabolism and anabolism because the mediator molecule has a certain lifespan. A unique currency, such as this, also limits the number of different protein structures and motifs needed to handle it, meaning that the same set of proteins can carry out anabolic reactions whether the organism is feeding on, for example, glucose or ammonium. From the point of view of energy efficiency, using intermediary molecules has both pros and cons. On the upside, dividing energy in small quanta reduces the amount of energy that is wasted for small tasks. On the downside, energy transformation is always performed at the price of some energy dissipation.

Adenosine triphosphate (ATP), one of the precursers of RNA and DNA, is the molecule of choice as an energy currency for all life on Earth. Other NTPs, such as GTP are used homologously by certain cellular processes (Orelle et al., 2018), but they are relatively rare exceptions. Interestingly, even flavin adenine dinucleotide (FAD) and nicotinamide adenine dinucleotide (NAD^+), molecules undertaking other energy carrying duties during catabolism, count an adenine in their structures. The reason for such preference towards adenine based compounds is uncertain (Bloch, 1996), although some evidence points towards the fact that adenine might have appeared by spontaneous synthesis in the primitive Earth (Oró et al., 1961). ATP was first isolated independently by Fiske and Subbarow and by Lohmann in 1929 (Maruyama, 1991) from liver and muscle tissue. Its structure was proposed by Makino in 1935 and confirmed by Lythogoe and Todd in 1945 (Maruyama, 1991). In 1941 Lipmann recognised that the molecule was capable of releasing significant amounts of energy owing to its phosphate bonds (Lipmann, 2006). The hydrolysis of ATP to adenosine diphosphate (ADP) and adenosine monophosphate (AMP) is in fact a strongly exergonic process, mostly because the loss of phosphate groups produces increasingly stable molecules. The energy produced by the hydrolysis of 1 mole of ATP under standard conditions (1 atm,

298K, [ATP]=[ADP]=[Pi]=1M) is around 30 kJ ("The value of G for the hydrolysis of ATP" 1972; Frey et al., 1995) but it can vary significantly depending on magnesium concentration and pH (Alberty, 1968; Shikama, 1971) (Fig. 1.3). Magnesium is thought to coordinate with the three phosphates of ATP stabilising its structure (Dudev et al., 2017), therefore lowering the free energy release associated with ATP hydrolysis. In living beings however, the concentrations of the three reagents, ATP, ADP and Pi, are far from the standard conditions. In exponentially growing *E. coli*, the ATP and Pi concentrations are often reported in the mM range while ADP is maintained one order of magnitude lower. The three concentrations vary depending on growth conditions and cellular physiological state and thus so does the energy provided by ATP hydrolysis.

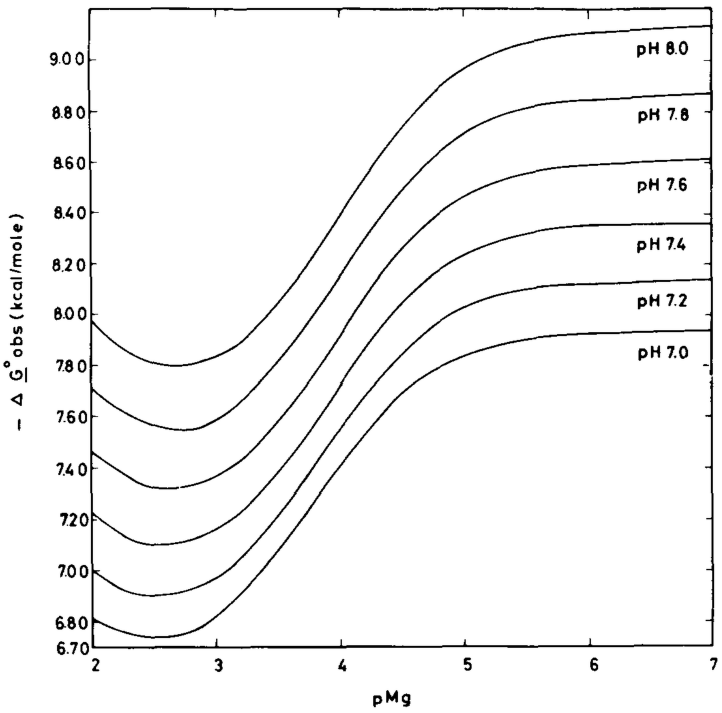

FIGURE 1.3: Energy provided by ATP hydrolysis at different pHs and concentrations of magnesium. From (Shikama, 1971).

1.8.1 ATP production

E. coli can catabolise substrates for the production of energy using various strategies of different efficiency. The most efficient, which is often portrayed in biochemistry books, is a three stage pathway commonly said to yield 38 molecules of ATP from the oxidation of one of glucose. The first stage is

called glycolysis a ten steps process, in which glucose initially undergoes ATP-consuming transformations that prepare it to be split in two molecules of glyceraldehyde 3-phophate (G3P). Each G3P is then further processed to pyruvate yielding, at the net of previous energy investments, one molecule of ATP and one molecule of NADH from NAD^+ such that from one molecule of glucose, two NADH and two ATP are produced (Fig. 1.4).

In some conditions such as anaerobiosis and overflow metabolism, glycolysis is sufficient to sustain *E. coli* growth when coupled to one or more of the many mechanisms that reconvert NADH to NAD^+. The combination of glycolysis with one of these NADH-NAD^+ conversion mechanisms is known as mixed-acid fermentation (Basan et al., 2015).

If higher efficiency is needed and oxygen is available, pyruvate can progress to the second stage of metabolism: the citric acid cycle, also known as tricarboxilic acid (TCA) cycle or Krebs' cycle, after the name of its discoverer (Krebs et al., 1937). In this series of reactions, the pyruvate transformed with the production of one NADH to acetyl-coenzyme A, a two carbon metabolite, reacts with citric acid, a four carbon metabolite. The resulting six carbon molecule is then processed yielding two molecules of CO_2, one of GTP or ATP, three NADH, one $FADH_2$ and citric acid to restart the cycle. It is interesting to note that practically all the macromolecules that *E. coli* can use as energy sources, such as carbohydrates, protein or lipids are eventually catabolised in the Krebs's cycle (Berg et al., 2002a). In the presence of oxygen, the NADH and $FADH_2$ produced are then oxidised replenishing the pool of NAD^+ and FAD and donating electrons to a series of transmembrane proteins that constitute the so called electron transport chain from which they are eventually passed on to oxygen. During the movement along such a chain of enzymes, the energy from the electrons is used to pump protons from the cytoplasm to the periplasm. This gradient of protons, together with the cell's membrane voltage (V_m) constitutes the proton motive force (PMF) that fuels the F_1F_o ATP synthase as originally proposed by Mitchell (Mitchell, 1961). This remarkable protein complex is made up of two motors from which it takes the name: the subunits F_1 and F_o. F_o sits in the plasma membrane and converts the flux of protons into rotation, which is in turn transferred to the cytoplasmic F_1 subunit that catalyzes ATP synthesis (Ballmoos et al., 2009). Notably, the ATP synthase can work in reverse, hydrolysing ATP to export protons to the periplasm (Capaldi et al., 2002). The transfer of a phosphate group through a high energy

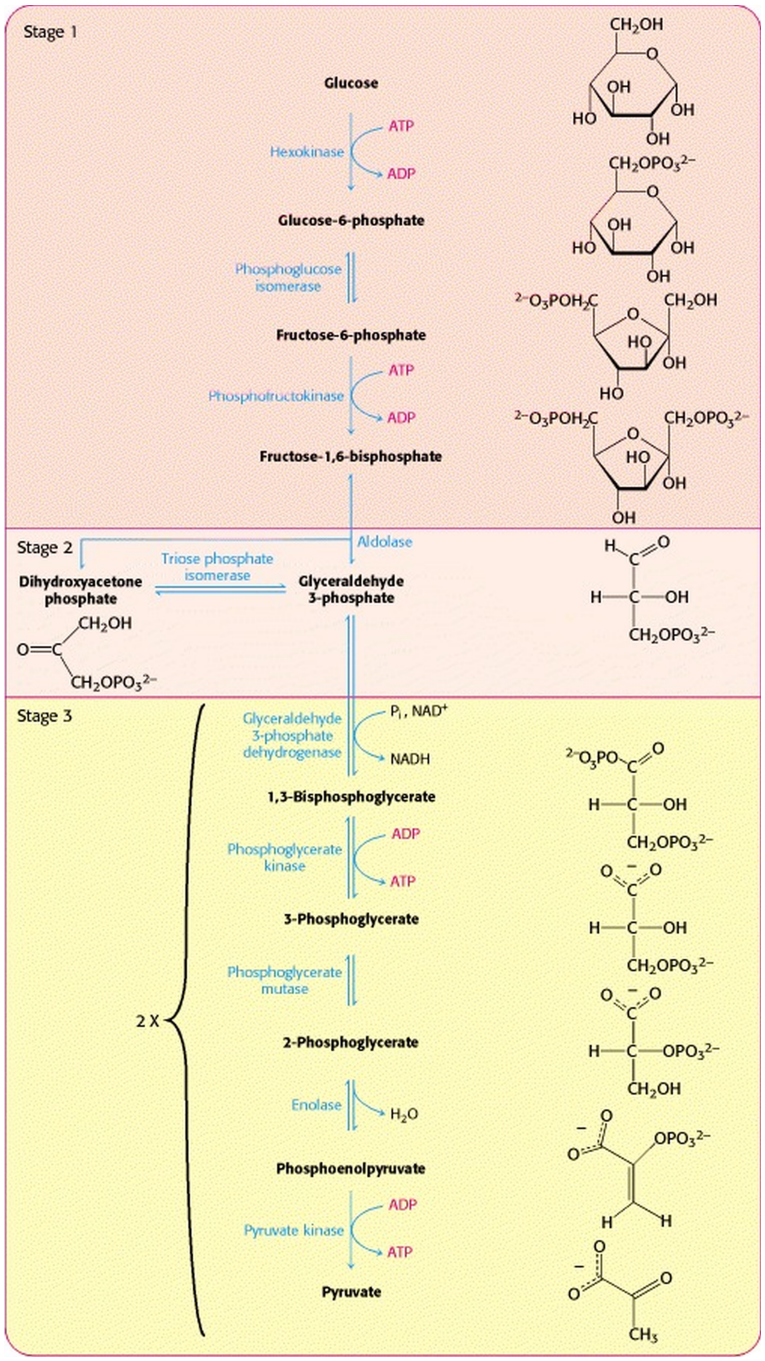

FIGURE 1.4: Glycolysis is a three stage process. In the first stage glucose, a 6-carbon sugar, is transformed in Fructose-1,6-biphosphate at the price of two ATP molecules. In the second stage, this is split in two 3-carbon compounds. In the third stage, the 3-carbon compounds are transformed into pyruvate yielding two ATP molecules and reducing one NAD^+ each. From (Berg et al., 2002a).

molecular intermediate which happens during the TCA cycle and glycolysis is commonly referred to as substrate level phosphorylation, while the synthesis of ATP according to Mitchell's chemiosmotic theory is known as oxidative phosphorylation (Prebble, 2001).

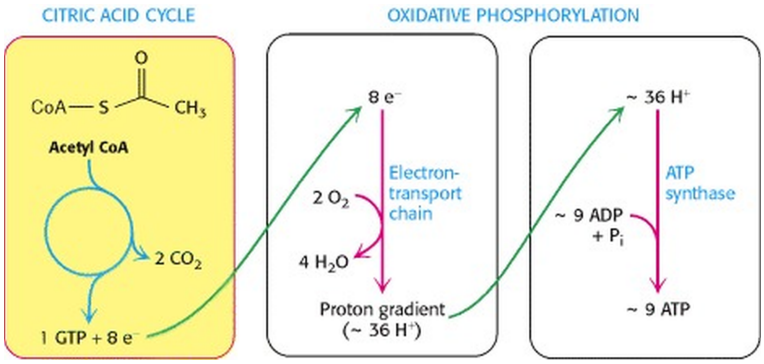

FIGURE 1.5: In the presence of oxygen the pyruvate produced during glycolysis can then be transformed in acetyl-coenzyme A which enters into the citric acid cycle producing one ATP or GTP and reducing NAD^+ and FAD. These are then oxidised by the electron-transport chain excreting protons from the cytoplasm and creating a PMF. The energy potential thus stored is used by the ATP synthase to produce ATP. From (Berg et al., 2002a).

1.9 PMF

The PMF fuels ATP synthesis through the F_1F_o ATP synthase (Bokranz et al., 1985; Rondelez et al., 2005), but also a number of other cellular processes such as the functioning of influx (Pao et al., 1998) and efflux pumps (Anes et al., 2015) and the bacterial flagellar motor (Fung et al., 1995; Gabel et al., 2003a). The PMF is the electrochemical potential of protons and it is made up of two components: the membrane voltage (V_m) and a term proportional to the ratio between the concentrations of protons (pH) across the membrane.

As explained in (Nicholls et al., 2002), the ΔG, which is the Gibbs free energy change in $kJ{\cdot}mol^{-1}$, produced by the movement of one mole of protons as a consequence of the membrane voltage is given by:

$$\Delta G = -FV_m \tag{1.1}$$

where F is the Faraday constant. While the ΔG produced by the movement of one mole of protons as a consequence of the proton gradient is given by:

$$\Delta G = RT \ln \frac{[H^+_{in}]}{[H^+_{out}]} \tag{1.2}$$

where R is the gas constant, T is the temperature and H^+_{out} and H^+_{in} are the proton concentrations on the outside and inside of the membrane. Since the two components are additive, the PMF is given by:

$$\Delta G = -FV_m + RT \ln \frac{[H^+_{in}]}{[H^+_{out}]} \tag{1.3}$$

While other kinds of ion motive force such as the sodium motive force can fuel the ATP synthase in other organisms (Schulz et al., 2013), in the case of *E. coli* that exclusively uses protons, the PMF can also be written in terms of the pH gradient:

$$\Delta G = -FV_m + 2.3RT(pH_{in} - pH_{out}) \tag{1.4}$$

and expressed in volts as originally done by Mitchell (Mitchell, 1961; Nicholls et al., 2002):

$$-\Delta G/F = -FV_m + 2.3RT(pH_{in} - pH_{out}) \tag{1.5}$$

E. coli is said to maintain a membrane voltage of around -150mV (Lo et al., 2007a) which is the result of charge separation across its inner membrane obtained by the combined action of the various cytochromes composing the electron transport chain and of several transporters of multiple ionic species (Loukin et al., 2005; Rhoads et al., 1978; Arkin et al., 2007a; Papanastasiou et al., 2013). Although this is probably far from being reached, the membrane's capability to withstand a potential before dielectric breakdown sets a physical limit to the value of the voltage achievable around 1.1-1.6V (Zimmermann et al., 1974). *E. coli* is a neutrophilic organism that tends to maintain its cytoplasm's pH homeostasis around 7.5 in external conditions ranging from 4.5 to 9 (Slonczewski et al., 1981; Zilberstein et al., 1984) but it is thought capable of withstanding pHs as low as 2.5 (Jonge et al., 2003). Such homeostatic capabilities are thought to be ascribable to the buffering capabilities of the cytoplasm and to the action of protonic pumps (Zilberstein et al., 1984). Because the contribution of the pH difference across the membrane (ΔpH) to the PMF roughly corresponds to 59mV per unit difference (Nicholls et al., 2002), in neutral and

alkaline conditions, *E. coli*'s PMF is mostly made up of V_m.

1.10 Measurement of the energy parameters of E. coli

E. coli largely fuels its reactions via the energy provided by ATP hydrolysis. The PMF, with its two components: V_m and ΔpH, in turn fuels many reactions happening close to the membrane, including oxidative phosphorylation, which is the most important ATP production mechanism of the cell in some conditions. NADH and $FADH_2$ are also energetically interesting molecules as they link metabolism and membrane carrying the electrons necessary for making up the PMF. As a result, the rates at which these molecules get oxidised and reduced must match, as their pool is relatively small and it is probably not capable of buffering big imbalances (Graef et al., 1999). Deviations from the optimal ratio are potentially frequent during environmental fluctuations and have sometimes been linked to halted growth and antibiotic survival (Chowdhury et al., 2016; Zhang et al., 2018). In this work, the focus was addressed to PMF and ATP, as changes in the NADH and $FADH_2$ oxidative states are likely reflected on the two. Examining such a state during dormancy is nevertheless an interesting research avenue, which, together with the measurements presented in the following chapters, has the potential to allow a global understanding of cellular energy fluxes.

1.10.1 Estimation of the PMF

One way to measure an energy source is by examining the rate of the reactions it fuels. In *E. coli*, among other processes, the PMF causes rearrangements of a protein complex which have repercussions observable at the micron scale and are therefore relatively easy to monitor: the bacterial flagellar motor. *E. coli* swims by rotating its peritrichous flagella that come together forming a bundle. Spatial navigation is achieved via the change in rotational direction, clockwise (CW) and counterclockwise (CCW), of one or more flagella, which causes a temporary disbandment of the bundle, an event macroscopically described

as tumble, that causes a reorientation of the cell (Turner et al., 2000). The frequency of tumble is governed by a chemotactic network. Substances characteristic of a favourable environment such as aspartate are called chemoattractant and their sudden appearance causes a reduction in the tumbling rate. Appearance of chemorepellents such as serine instead increase it (Adler, 1975). Flagella up to 10μm in length are connected to a motor by an universal joint referred to as the hook. The motor encompasses two sections: the rotor and the stator. Protons driven by the PMF flow through the stator units producing torque via a mechanism that has only recently been proposed (Fig. 1.6). According to such a model, stator units perform a two-stage power stroke on the rotor. In the first stage, in the presence of a PMF, a proton binds to the binding site of one of the two stator subunits: MotB. This causes a conformational rearrangement in the other subunit, MotA, which delivers a steric force to the rotor and particularly to one of its components named FliG. In the new conformation, the proton is free to flow to the cytoplasmic side of the inner membrane. This restores the initial conformation delivering the second stage of the power stroke (Mandadapu et al., 2015). The PMF value correlates linearly with flagellar motor speed (Gabel et al., 2003a) (Fig. 1.6), which in turn correlates linearly with bacterial swimming speed (Magariyama et al., 1995; Magariyama et al., 2001). Thus, measurements of bacterial swimming speed and of flagellar motor speed can be used as a proxy for PMF. To assay the latter, it is possible to rely on cameras with high acquisition rate capabilities (Magariyama et al., 2001) or back focal plane interferometry (Svoboda et al., 1993), which was the favoured technique in this work and will be discussed further in the following chapters. Because the spinning of single flagella is hard to measure, motor speed is commonly assayed by either attaching flagella to a coverslip and measuring the rotational speed of the cell body, or by attaching small latex or polystyrene beads to flagellar stubs that carry a mutation making them sticky (Scharf et al., 1998) (Inset Fig. 1.6D) (Gabel et al., 2003a).

Because the PMF is made up of ΔpH and membrane voltage, another possibility for its estimation is measuring its two components. Techniques for assaying membrane voltage are reviewed and examined in detail in Chapter 2.

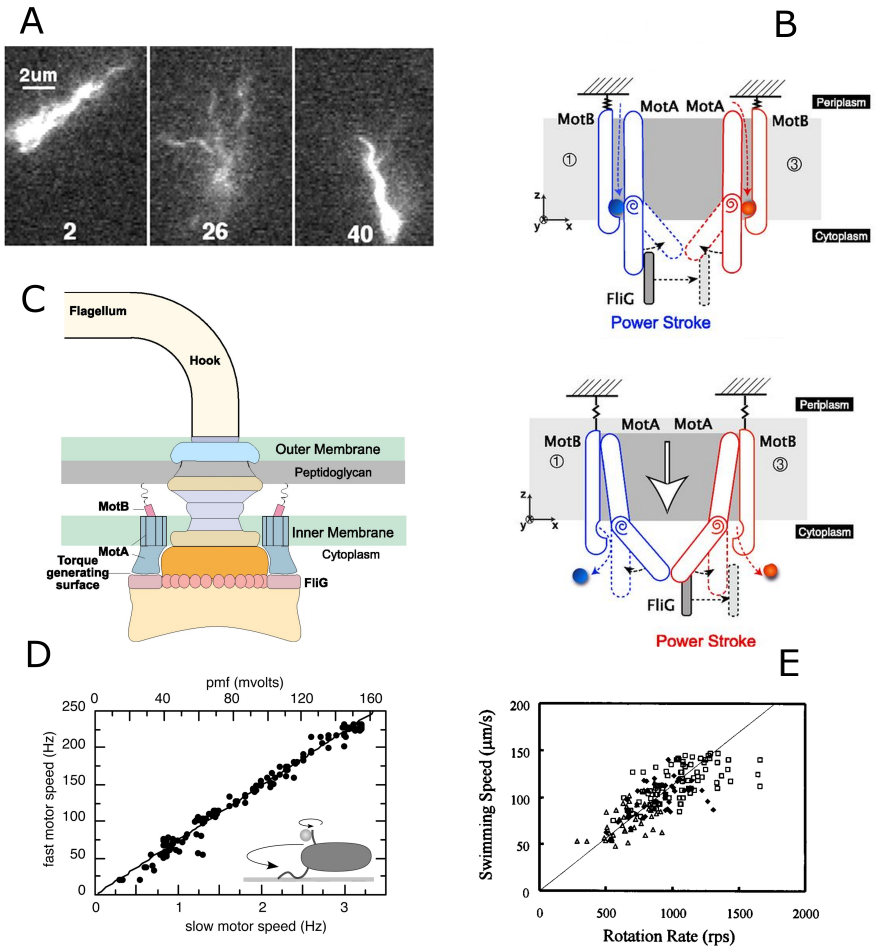

FIGURE 1.6: The bacterial flagellar motor as a proxy for PMF. a) *E. coli* swimming using a bundle of flagella. Change in rotational direction by one or more flagella causes bundle disbandment and run resumption in a new direction. The images are taken from the same cell over a certain time span. Adapted from (Turner et al., 2000). b) Model illustrating the mechanism of power stroke delivered from the stators (made up of MotA and MotB) to the rotor (here only represented by its subunit FliG). Adapted from (Mandadapu et al., 2015). c) Structure of the bacterial flagellar motor (BFM). The motor spans the whole cell envelope of *E. coli*, while the protons making up the PMF cross the inner membrane during flagellar rotation. Adapted from (Mandadapu et al., 2015). d) Correlation between BFM speed and PMF at high and slow load on the motor. Measurements were performed by simultaneously measuring the speed of two motors of the same cell. The slow motor was propelling a flagellum tethered to a microscope coverslip and therefore driving the rotation of the cell body. The fast one was spinning a 0.4 micron latex bead (as depicted in the inset). The PMF is rescaled on the assumption that fully energised *E. coli* has a PMF of -150mV. Adapted from (Gabel et al., 2003a). e) Proportionality of flagellar motor and bacterial swimming speed measured by laser dark-field microscopy. Adapted from (Magariyama et al., 1995)

.

1.10.2 Measurements of ΔpH

Knowing the pH of the cellular milieu is relatively easy, in facts, if fresh medium is continuously replenished to the sample or if the cells are sufficiently diluted, knowledge of the initial pH of the medium is normally sufficient. However, measuring the cytoplasmic value is more complex. Probes of intracellular quantities share common problems such as the necessity of permeating the cell envelope, the need for low toxicity and the impracticality of their calibration. These common experimental limits are extensively discussed in Chapter 2 for membrane voltage probes and Chapter 3 for ATP probes and most of the concepts can be applied to pH measurements. As was the case for the assay of other cellular parameters, the first intracellular pH measurements were obtained at the population level using techniques such as ^{31}P-NMR (Slonczewski et al., 1981). Only later and particularly with the advent of genetically expressed indicators the focus could be shifted to single cells. Nowadays, more than one pH sensitive protein probe exists that can be used in *E. coli*. pHluorin and cpYFP, for example, are ratiometric sensors whose optical properties are sensitive to the molecule's protonation state and upon appropriate calibration can easily be used to estimate cytoplasmic pH at the single cell level and as a function of time (Fig. 1.7). The constitutive expression of these probes has pre-

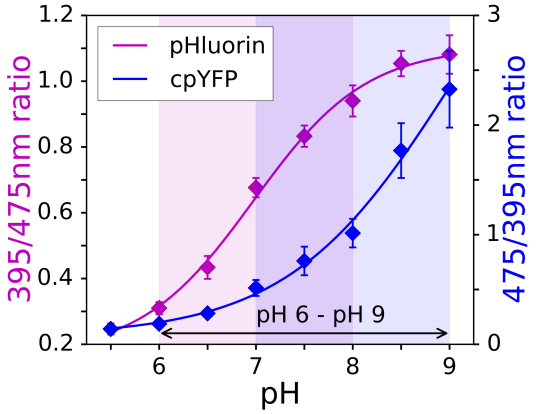

FIGURE 1.7: pHluorin and cpYFP are ratiometric protein sensors that change their optical properties depending on the pH. In the lab, Krasnopeeva optimised their constitutive expression for use in *E. coli*. Image from (Krasnopeeva, 2018)

.

viously been optimised for *E. coli* in the lab (Krasnopeeva et al., 2019). pHRed is also an interesting option for its longer excitation and emission wavelengths

(Tantama et al., 2011), which would limit toxicity due to illumination during imaging (Krasnopeeva et al., 2019), but its constitutive expression in *E. coli* at the moment requires further work (Krasnopeeva, 2018).

1.11 Aims and overview

This work aims at addressing the urgent need to understand the mechanisms of antibiotic survival during bacterial dormancy. In particular, it examines the hypothesis that the physiological state and the cellular energetics during dormancy might have an the intimate link with survival. To this end, single cell tools for the assay of energy parameters were first considered and developed and later complemented to existent ones for the assay of dormant states.

- In Chapter 2 the focus is addressed towards membrane voltage measurements in bacteria and particularly towards nernstian dyes and their usage in physiological conditions;
- Chapter 3 describes the development of a single cell technique for the measurement of ATP concentration in the bacterial cytoplasm at the single cell level and over time;
- In Chapter 4 single cell measurements of energy parameters performed during dormancy are presented. The results show that energetics vary depending on the reasons for the acquisition of dormancy, suggesting not only that dormancy is not a univocal physiological state, but that not all dormant states might be equally susceptible to antibiotic treatments;
- Because energy is involved in the exchanges cells have with the environment, in chapter 5 I propose a preliminary model of antibiotic accumulation in the cytoplasm that takes into account said energy parameters. The model moves a step towards the ambitious goal of understanding the connection between bacterial physiological state, antibiotic dynamics and cell survival. In addition, because antibiotic killing in given physiological states and for given antibiotic mechanisms might produce signature survival rates, it may be possible to use the model to predict accumulation and killing mechanisms of uncharacterised antibiotics.

Chapter 2

Membrane voltage estimation

2.1 Introduction

2.1.1 Electrode-based techniques

Electrode based techniques for measuring membrane voltage were the first to be developed. Their application to biology traces back to the experiments performed by Hodgkin and Huxley on squid axons (Hodgkin et al., 1939), which relied on the physical insertion of a 100μm glass tube with a silver wire within, into the squid's nerve fibers that have a 0.5mm section. The method went through several rounds of improvement, particularly in terms of capillary size reduction (Ling et al., 1949), eventually becoming applicable to mammalian neurons (Sakmann et al., 1984). The size of bacteria and the presence of a cell wall limit the usability of these techniques to giant spheroplasts, which are bacterial cells that have been deprived of the cell wall via antibiotic treatment. Because the cell wall sustains a substantial amount of turgor pressure, these treated cells swell to a diameter of 5μm (Felle et al., 1980), thereby solving both of the assay's technical issues. Although measurements obtained with spheroplasts are precious to understand some aspects of bacterial functioning, the removal of part of the cell envelope likely causes important changes to cell physiology and it is not ideal for assaying bacterial responses to antimicrobials.

2.1.2 Conformation-change-based sensors

Molecular sensors overcome the need of using electrodes and can be used to quantify relative changes in membrane voltage in physiological conditions. They are typically based on either fluorescent dyes or proteins whose optical properties change in response to changes in V_m. For this to happen, they

need to be positioned in the close proximity of the membrane, such that the potential can alter their conformation or electron distribution. Because these changes happen on very short timescales, these molecules are sometime referred to as fast probes. One example of conformation-changing voltage sensitive dyes is di-8-ANEPPS. This fluorescent molecule belongs to a class of dyes that have fast response speed, but that change their optical properties by only small amounts as a result of changes in V_m (Fluhler et al., 1985), a downside shared by many conformation-change based sensors (Manno et al., 2013). Genetically expressed probes have the advantage of not having to permeate the cell envelope to perform their function and a number of them has been developed, varying in spectra, speed and signal intensity (Xu et al., 2017). One exponent of this class that has been used in *E. coli* is PROPS (Kralj et al., 2011). The main downside of these tools is that they cannot be used to estimate absolute voltage values unless they are calibrated via other techniques.

2.1.3 Nernstian sensors

Like conformation-change based sensors, Nernstian sensors are capable of overcoming the limitations imposed by the presence of the cell envelope. The molecules permeate into the cell cytoplasm in concentrations that are defined by their electrochemical potential, of which the membrane voltage is a component. This confers them an intrinsic calibration against membrane voltage, because the relationship between their concentration and the V_m is described by Nernst equation. Among the main members of this class of probes which will be treated in detail in this chapter, there are the anionic $DiBAC_4(3)$ (Adams et al., 2012), the self-quenching $DiSC_3(5)$ (**TeWinkel2016**), the scarcely permeant in growth medium TMRM (Lo et al., 2007a), TPP^+ (Felle et al., 1980) and Thioflavin T (ThT) (Prindle et al., 2015).

Because I wanted to assay the physiology of dormant cells in conditions as realistic as possible and I wanted to obtain membrane voltage values that could be used to calculate its contribution to PMF, in this work I chose to focus on Nernstian sensors. In the following paragraphs of this chapter, I present a work that was carried out with colleagues in an international collaboration, whose contributions are specified in the paragraph *Author contributions*, that investigates the common pitfalls encountered during the use of Nernstian dyes. In the discussion, we propose a simple experimental algorithm that

aims at enabling the correct characterization of novel nernstian dyes in their interaction with the cell and its physiology. We inaugurated the procedure for the characterization of the dye ThT, that had been never used in *E. coli* before (Mancini et al., 2020).

A general work-flow for characterization of Nernstian dyes and their effects on bacterial physiology

Authors

Leonardo Mancini[1], Guillaume Terradot[1,*], Tian Tian[2,*], YingYing Pu [2], Y Li[2], Chien-Jung Lo[3], Fan Bai[2], Teuta Pilizota[1,+]

Affiliations

[1] Centre for Synthetic and Systems Biology, University of Edinburgh, Edinburgh, UK
[2] Biomedical Pioneering Innovation Center (BIOPIC), School of Life Sciences, Peking University, Beijing 100871, China
[3] Department of Physics and Graduate Institute of Biophysics, National Central University, Jhongli, Taiwan 32001, ROC
[*] these authors contributed equally to this work
[+] Corresponding author:teuta.pilizota@ed.ac.uk

Abstract

The electrical membrane potential (V_m) is one of the components of the electrochemical potential of protons across the biological membrane (proton motive force), which powers many vital cellular processes. As V_m also plays a role in signal transduction, measuring it is of great interest. Over the years a variety of techniques has been developed for the purpose. In bacteria, given their small size, Nernstian membrane voltage probes are arguably the favourite strategy, and their cytoplasmic accumulation depends on V_m according to the Nernst equation. However, a careful calibration of Nernstian probes that takes into

account the trade-offs between the ease with which the signal from the dye is observed, and the dyes' interactions with cellular physiology, is rarely performed. Here we use a mathematical model to understand such trade-offs, and apply the results to asses the applicability of the Thioflavin T dye as V_m sensor in *Escherichia coli*. We identify the conditions in which the dye turns from a V_m probe into an actuator, and, based on the model and experimental results, propose a general work-flow for the characterization of Nernstian dye candidates.

Significance Statement

The phospholipid bilayer of a biological membrane is virtually impermeable to charged molecules. Much like in a rechargeable battery, cells harness this property to store an electrical potential that fuels life reactions but also transduces signals. For the case of bacteria, which are small in size and possess a stiff cell wall, arguably the most popular approach to measuring membrane voltage are Nernstian probes that accumulate across the bacterial membrane according to the Nernst equation. The present study characterizes the undesired effects Nernstian probes can have on cell physiology, which can be crucial for the accurate interpretation of experimental results. Using mathematical modelling and experiments, the study provides a general, simple work-flow to characterize and minimize these effects.

Introduction

Living cells maintain an electric potential difference (V_m) across the plasma membrane that acts like a capacitor. This is achieved by active transport of ions:

$$V_m = F \cdot \frac{Q_{in}}{C} \tag{2.1}$$

where Q_{in} is the intracellular charge (in moles), C the membrane capacitance and F the Faraday constant. Membrane potential stands at the basis of fundamental biological processes, such as signal transduction and energy production (Del Castillo et al., 1954; Mitchell, 1961). For the latter, V_m adds up to the chemical potential of protons, arising from their concentration difference

across the membrane, to result in the proton electrochemical gradient, so called proton motive force (PMF). The PMF drives numerous cellular processes, most notably the production of ATP (Mitchell, 1961), import of nutrients or osmolites (Ramos et al., 1977; Bradbeer, 1993; Jahreis et al., 2008; Wood, 2015) rotation of the bacterial flagellar motor (Sowa et al., 2008), and it is necessary for cell division (Strahl et al., 2010).

The notion that V_m lies at the very basis of life motivated decades long efforts to measure it (Bernstein, 1868). The first direct technique dates to 1939 and relies on the mechanical insertion of microelectrodes into squid giant axons (Hodgkin et al., 1939). The method led to the development of the patch-clamp technique, which advanced the understanding of neuron signal transduction (Neher et al., 1976; Sakmann et al., 1984; Ling et al., 1949). However, applicability of microelectrodes for the measurement of bacterial V_m is limited, owing to the small size of the organisms and the presence of the cell wall (Martinac et al., 1987; Martinac et al., 2013). Some of the subsequently developed methods overcome such limits with the use of molecular sensors (Felle et al., 1980), grouped in two categories: conformational-change-based sensors and Nernstian sensors. The former are static molecules or proteins that sit inside the membrane, or in its close proximity, and change conformation or electron distribution in response to changes in V_m, which in turn affect the optical properties of the chromophores (Tsutsui et al., 2008; Fluhler et al., 1985; Kralj et al., 2011). Here we focus on the latter, the Nernstian sensors, and on the parameter range in which they serve as V_m indicators, using *Escherichia coli* as the model organism.

Nernstian sensors are charged molecules that can diffuse across the biological membranes and distribute according to the Nernst equation:

$$V_m = \frac{RT}{zF} \ln\left(\frac{c_{out}}{c_{in}}\right) \tag{2.2}$$

where R, T, z, F, c_{out}, c_{in} denote respectively gas constant, temperature, valence of the charged molecule, Faraday's constant, external and internal concentration of the charged molecule. For a measurement to be attained, these molecules need to emit a signal that is a proxy for their number. Therefore, Nernstian V_m dyes are usually radio-labeled or fluorescent molecules (Felle et al., 1980; Sims et al., 1974), and V_m is calculated from equation (2.2) by measuring the cytoplasmic (c_{in}) and the external dye concentration (c_{out}) (Lo et al.,

2007b).

However, Nernstian dyes are used in complex biological systems and a number of factors can be responsible for an incomplete adherence to a fully Nernstian behavior. In Fig.2.1 we give a cartoon representation of the trade-offs imposed on a Nernstian dye by plotting the dye intensity inside *E. coli's* cytoplasm against the time. The chosen dye concentration should be such that the signal is sufficiently above the background (ΔI is sufficiently large). Yet, with increasing dye concentration, cell's V_m is more likely to be affected by the dye. This caveat is inherent to positively charged dyes as these directly lower V_m and more so at higher concentrations (Kashket, 1985). The first requirement for a Nernstian dye is, thus, existence of a range of concentrations that give sufficient signal without extensively affecting the V_m. Likewise, cellular processes should not interfere with the Nernstian behavior of the dye, for example by actively importing or exporting it. Instead, the dye should be able to diffuse across the membrane and its diffusion constant will determine the time it takes for the dye to equilibrate across the membrane in agreement with equation (2.2) (τ_{eq} in Fig. 2.1). All phenomena that occur quicker than τ_{eq} are beyond the dye's temporal resolution, and all the measurements taken before τ_{eq} do not faithfully report V_m. Lastly, different dyes bind to the membrane or form aggregates to a different extent (Lo et al., 2007b; Ehrenberg et al., 1988)). However, as long as the dyes do not self-quench at any point (Te Winkel et al., 2016), or undergo signal enhancements, a constant and well defined correlation function between the free dye concentration and the signal can be obtained, thus enabling quantitative V_m measurements (most commonly this is done by separating the signal from the free and bound dye with careful calibration (Lo et al., 2007b; Ehrenberg et al., 1988)).

To summarize, to be used as an ideal Nernstian sensor, a cationic dye should: (i) give a sufficiently high signal without affecting cell's V_m; (ii) diffuse through the membrane with τ_{eq} on the order of minutes; (iii) stay inert, despite being charged, and not form bonds or in any way interact with cell; (iv) have constant signal per molecule. Yet, when using such dyes these requirements are rarely assessed in a systematic manner before measurements commence. In this work we identify a work-flow that should be adopted, for a given choice of the dye, organism and external environment, in order to identify the parameter range in which Nernstian dyes act as sensors, rather than actuators,

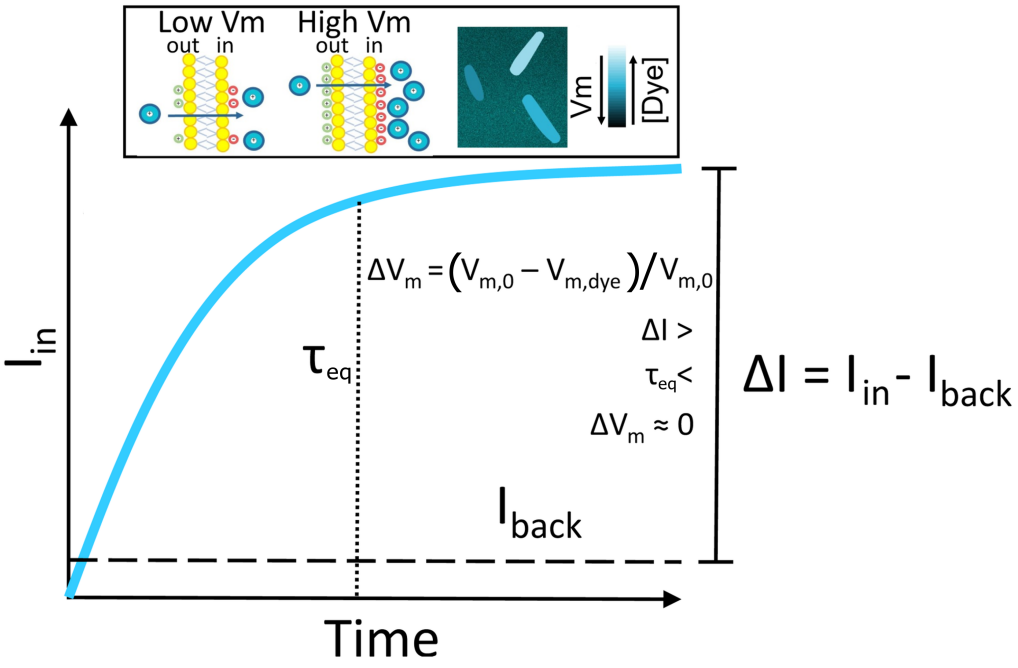

FIGURE 2.1: A schematic plot of a Nernstian dye equilibration curve. Equilibration time, τ_{eq}, is defined as the time at which the dye internalized by the cell, dye I_{in}, reaches the 90% of its final value. $V_{m,0}$ and $V_{m,dye}$ indicate the membrane potential before and after the addition of the dye, respectively. I_{back} is the fluorescence intensity of the background. Inset: cartoon showing the mechanism of accumulation of cationic dyes, which accumulate more in cells with a more negative V_m.

i.e. molecules that actively decrease or increase the V_m. We start with a mathematical model that helps us understand relationships and define trade-offs between dye working concentration and signal intensity, equilibration time and V_m perturbation. We then show how the identified work-flow can be used to benchmark new Nernstian dyes by characterizing the recently reported dye Thioflavin T (ThT) used in *Bacillus subtilis* (Prindle et al., 2015), for use in *E. coli*. We describe the physiological range in which ThT enables V_m sensing in *E. coli*, and, in the range where we find it turns into an actuator, we investigate the mechanistic reasons. Our work-flow can be applied to the characterization of other Nernstian dyes and provide novel insights for the established ones.

Methods

Bacterial strains

All experiments where no mutation is explicitly indicated were carried out in the MG1655 strain. For the BFM speed assay we used MG1655 carrying the FliC-sticky mutation from (Krasnopeeva et al., 2019). Δ*tolC* mutants were obtained from the Keio collection (Baba et al., 2006). Kanamycin resistance of the Keio deletion strain was removed via one-step inactivation with the plasmid pCP20 (Datsenko et al., 2000). Kanamycin resistance inactivation and elimination of the pCP20 plasmid were confirmed via Kanamycin (50 μg/ml), Chloramphenicol (31 μg/ml) and Ampicillin (100 μg/ml) sensitivity tests. Both the strain carrying the Δ*tolC* mutation and MG1655 wild-type were transformed with plasmid pTP20-mKate2 (Fig. SI1) for cytoplasmic volume measurements. pTP20-mKate2 contains the red fluorescent protein mKate2 and the ribosomal binding site (RBS) of mCherry. The plasmid was constructed as follows: the backbone from pWR20 (Pilizota et al., 2012) and the sequence containing the RBS of mCherry and mKate2 were PCR amplified. The products were purified, cleaved with the restriction enzymes AvrII and NotI (NEB, UK) and ligated using T4 DNA ligase (Promega, UK). Chemically competent cells were transformed with the ligation mixes and transformants were confirmed by colony PCR and subsequently sequenced. A map of the plasmid and the primers are given in SI (Fig. SI1 and Table SI1). All the strains used in the study are summarized in the Table SI2.

Bacterial growth conditions

Cells for fluorescence microscopy were grown from an overnight culture by diluting it 1:80 times in LB (0.5% Yeast Extract, 1% Bacto tryptone, 1% NaCl). The culture was shaken at 220 rpm at 37°C and harvested at OD_{600}=0.3-0.5. Cells were then washed into fresh LB or MM9 + glucose medium (50mM Na_2HPO_4, 25mM NaH_2PO_4, 8.5mM NaCl, 18.7mM NH4Cl, 0.1mM $CaCl_2$, 1mM KCl, 2mM $MgSO_4$, 1x MEM essential amino acids (Gibco, UK) and 0.3% glucose). For the simultaneous BFM speed and ThT fluorescence measurements cells were grown from an overnight culture by diluting it 1:80 times in TB (1% Bacto tryptone, 0.5% NaCl) at 200 rpm and 30°C. Cells were harvested at OD_{600}=0.8 as before (Rosko et al., 2017) and washed to fresh MM9 via centrifugation.

Growth curves in the presence of ThT were obtained in a Spectrostar Omega microplate reader (BMG, Germany) using a flat-bottom 96-well plate that was covered with a lid during the experiments (Costar, UK). Each well contained 200μl of growth media, either MM9 + glucose or MM9 + glycerol (50mM Na_2HPO_4, 25mM NaH_2PO_4, 8.5mM NaCl, 18.7mM NH4Cl, 0.1mM $CaCl_2$, 1mM KCl, 2mM $MgSO_4$, 1x MEM essential amino acids (Gibco, UK) and 0.3% glycerol), and was inoculated with 2μl (1:100 dilution) of an overnight culture and a given concentration of ThT. Plates were grown at 37°C with 300 rpm shaking (double orbital mode). ThT (Acros organics, USA) solutions were prepared from a 10 mM stock of ThT in water made at least monthly and stored at 4°C in the dark.

Fluorescence microscopy

Imaging was carried out in a custom-built microscope with a 100x oil immersion objective lens (Nikon, Japan), Neutral White LED as a source of illumination (Cairn Research Ltd, UK) and images were taken with an iXon Ultra 897 EMCCD camera (Andor, UK) (Rosko, 2017; Krasnopeeva, 2018). ThT fluorescence was measured with ZET436/20x and ET525/40m, and mKate2 and PI fluorescence with ET577/25x and ET632/60m (Chroma Technology, USA) excitation and emission filters, respectively. Images were taken at 1 min intervals, exposure time was 50 ms and Andor camera gain 25. We note that ThT undergoes a spectral shift and intensity increase when highly concentrated or when spatially constricted, either by binding to amyloid fibrils or by viscosity (Sulatskaya et al., 2017; Maskevich et al., 2007; Maskevich et al., 2015). Our choice of filters aims at minimizing these effects and the damage that shorter wavelengths cause to *E. coli* (Vermeulen et al., 2008). Cells were imaged in a custom-built flow-cell (Fig. SI2, (Krasnopeeva et al., 2019)), and attached to the coverslip surface as before (Rosko et al., 2017; Krasnopeeva et al., 2019). Briefly, 1% Poly-L-Lysine (Sigma, UK) is flushed through the flow cell and washed with 3-5 ml of growth media after 10 s. Polystyrene particles (beads) with a diameter of 1 μm (Bangs Laboratories, USA), were delivered into the flow-cell and allowed to attach to the coverslip surface. After 10 min unattached beads were flushed away with 1-2 ml of growth media. Next, 200 μl of cells were delivered to the flow-cell and allowed to attach for 10-30 min, after which the unattached cells were removed with 1 ml of growth medium. 10 μM ThT in

growth media was delivered with a peristaltic pump (Fusion 400, Chemyx, USA) using 50 μl/min flow rate while imaging. We deliver 5 μM of PI stain (MP Biomedicals, USA) in the same way. 5mM PI stock solution (in water) was stored at 4°C in the dark. Images were stabilized in x, y and z position using a bead attached to the cover-slip and back-focal-plane interferometry (Pilizota et al., 2012; Buda et al., 2016). Cells grow attached to the Poly-L-Lysine surface with expected growth rates (given the medium), as previously reported (Wang et al., 2019) and seen in SI Video 1 and 2.

Motor speed measurements

Single motor speeds were measured as before (Rosko et al., 2017; Krasnopeeva et al., 2019). Briefly, we sheared flagellar filaments by passing them through two syringes with narrow-gauge needles (26 gauge) connected by plastic tubing. The cell attachment protocol was as above, except 0.5 μm beads (Polysciences, USA) were delivered after cell attachment allowing them to attach to filament stubs. Motor speed was measured during continuous flow that delivered MM9 + glucose medium supplemented with 10 μM ThT. Back-focal-plane interferometry setup and recording conditions are as before (Rosko et al., 2017).

Data analysis

Motor speed traces

Raw traces of the position of the bead attached to the filament stub were analyzed by a moving-window discrete Fourier transform as in (Rosko et al., 2017). From the obtained motor speed traces DC frequency (50 Hz) was removed, speeds lower then 5 Hz ignored, and subsequently a median filter (window size 11) was applied (Krasnopeeva et al., 2019). We note that we use a wild type strain for which the BFM can change rotational direction, which appears as a negative speed after application of the moving-window Fourier transform. However, for the purpose of the PMF measurements, these short intervals can be disregarded, and we only show the speed values above 0 Hz.

Fluorescence images

The image analysis was carried out with a custom written software. From fluorescence images, rectangles containing 'flat' cells, i.e. cells that are uniformly attached to the coverslip surface, as well as background rectangles within each cell-containing rectangle, were manually selected (Buda et al., 2016; Pilizota et al., 2012). The edge of the cell was identified within the cell-containing rectangle by applying a global threshold via the Otsu's method (Otsu, 1979). Total cells' intensity values were obtained by summing up and averaging pixel belonging to the cells. Values obtained from the background rectangles at the time points when ThT was loaded in the channel but cells had not taken it up yet, were subtracted from the cell intensity values. The beads used for image stabilization stain easily with ThT, and were used as a point of reference for dye entry (which in our case occurred 7 to 10 min from the start of imaging). We show fluorescence intensity traces that start at the point of ThT entry, but note that cells were exposed to fluorescence illumination in the 7-10 min interval before. For the low fluorescence values characteristic of the early stages of dye equilibration, our script fails to identify cells, in which case we linearly interpolate values between two closest events of successful cell identification. Cell area was measured from intensity profiles, by normalizing them and counting the pixels above 30% of maximum intensity as described previously (Pilizota et al., 2012; Buda et al., 2016)

Plate reader data

Individual growth curves were analyzed with the software deODorizer from (**Swain2016**). To extract the maximum growth rate, 3 or more repeats in the same condition were aligned by the chosen OD value (usually OD$\sim$0.4) using the growth curve that reached it first (in the given condition). The maximum growth rates given in Fig. 2.3C were normalized by the maximum growth rate in $[\text{Dye}]_{out}$=0 condition.

Results

Mathematical model of Nernstian dye's behavior defines its working parameter range

To predict and understand the mutual effects of dye concentration and cell physiology we turn to a mathematical model. We assume that the cytoplasmic and extracellular liquids are electrical conductors separated by a membrane, which we treat as a parallel-plate capacitor (equation 2.12) (Rybak et al., 1997; Grabe et al., 2001). We model the membrane as a single lipid barrier and do not distinguish between the inner and outer membrane of *E. coli*. In the SI we discuss a more detailed model that includes both membranes and allows for the existence of a small V_p across the outer membrane, in addition to the V_m across the inner membrane. We account for four types of charge carriers and assume that all are monovalent to simplify the model without altering the results with respect to V_m dye behavior: *(i)* negatively charged molecules to which the membrane is close to non-permeable denoted Y (this includes surface charges on the inside of the membrane), *(ii)* cationic species actively pumped outward denoted C^+, *(iii)* anionic species, which equilibrates across the membrane A^- and *(iv)* cationic species that equilibrate across the membrane (playing the part of a cationic dye). Thus Q_{in} is:

$$Q_{in} = V_{cell} \cdot \underbrace{\sum_x z_x [x]_i}_{\text{General Form}} = V_{Cell} \cdot \underbrace{\left([Dye]_{in} + [C^+]_{in} - [A^-]_{in} - [Y]_{in}\right)}_{\text{This manuscript}} \tag{2.3}$$

where V_{cell} is the intracellular volume, z_x valency of species x and $[x]_i$ its intracellular concentration (we only consider $z_x = \pm 1$). The extracellular concentrations and $[Y]_{in}$ are constants set by the initial conditions (we assume that the cell does not affect the ionic composition of its environment and we treat $[Y]_{in}$ as unable to cross the membrane). We also assume that the cell uses only one type of pumps for cations, and note that $[Dye]_{in}$ and $[Dye]_{out}$ are experimentally determined from fluorescence intensity signal (see Fig. 2.6 later in the text).

The charge separation, and thus V_m, is achieved in the close proximity of the bilayer, so that the rest of the cell's cytoplasm stays electroneutral (Grabe

et al., 2001; Nelson, 2003), and in two ways. First, by pumping C^+_{in} outwards and thus creating a negatively charged intracellular environment, and second by maintaining $[Y]_{in}$. Pumping C^+ outwards against its electrochemical gradient requires free energy, which we consider a constant and label ΔG_E (where $\Delta G_E < 0$). For example, in the case of a proton:ion antiporter with 1:1 exchange stoichiometry the free energy is the PMF itself, for a similar antiporter with 2:1 proton:ion stoichiometry it is $2 \times$ PMF, and for ATP hydrolysis, ΔG_E is the amount of work given by hydrolyzing one ATP.

The rate at which C^+ is pumped out of the whole cell, given in mol/m^3/s, is:

$$j_P = k_P \cdot \left(1 - e^{\Delta G_P/(RT)}\right) \tag{2.4}$$

where k_P is a function that describes the specifics of the transport mechanism by a given pump, here, we keep it a constant. ΔG_P depends on the electrochemical potential of the pumped cation (ΔG_{C^+}) and ΔG_E. Therefore, the rate of pumping (positive flux means C^+ is extruded) depends on the intracellular ionic composition via V_m and $[C^+]_{in}$:

$$\Delta G_P = \Delta G_E - \Delta G_{C^+} \tag{2.5}$$

$$\Delta G_{C^+} = F \cdot V_m + RT \cdot \ln\left(\frac{[C^+]_{in}}{[C^+]_{out}}\right) \tag{2.6}$$

Note that in order for the pump to move C^+ outward $j_P > 0$, and consequently $\Delta G_E < \Delta G_{C^+}$, i.e. the free-energy providing reaction has to be able to overcome the electrochemical gradient of the C^+. The chosen functional dependency of j_P gives the simplest pump kinetics, sufficient for our purpose, which can be expanded to include more complex pumping scenarios (Keener et al., 2009).

Finally, the dye, the anion and the cation leak through the membrane (positive flux means x is moved inward) at the rate:

$$j_{L,x} = k_{L,x} \cdot \left(1 - e^{\Delta G_x/(RT)}\right), x \in \{Dye, C^+, A^-\} \tag{2.7}$$

$$\Delta G_x = F \cdot V_m + RT \cdot \ln\left(\frac{[x]_{in}}{[x]_{out}}\right) \tag{2.8}$$

Similarly to k_P, $k_{L,x}$ is a function whose shape depends on the mechanisms

by which an ion leaks across the *E. coli* membrane, which in turn depends on the electrostatic potential at a position z within the membrane, $V(z)$. To the best of our knowledge, $V(z)$, and consequently $dV(z)/dz$, are not known for *E. coli*. Therefore, we chose Eyring's model that has been verified for cationic leakage across the mitochondrial membrane (Garlid et al., 2003), and which assumes $V(z)$ abruptly changes in the middle of the lipid bilayer, such that $dV(z)/dz = 0$ everywhere but at the geometrical middle of the membrane where $dV(z)/dz = V_m$ (Garlid et al., 1989). We then have:

$$k_{L,x} = \frac{S_{cell}}{V_{cell}} \cdot P_x \cdot [x]_{out} \cdot e^{-\frac{F \cdot V_m}{2 \cdot RT}}, \text{ with } x \in \{Dye, C^+, A^-\} \tag{2.9}$$

where S_{cell} denotes the cell's surface area and P_x the permeability of the membrane for $x \in \{Dye, C^+, A^-\}$ (obtained by assuming the solubility-diffusion model (Shinoda, 2016)).
At steady-state Dye and A^- equilibrate across the membrane according to Nernst equation ($d[Dye]_{in}/dt = j_{L,Dye} = 0 \Leftrightarrow \Delta G_{Dye} = 0$, leading to (2.2)), whereas for the monovalent cation $d[C^+]_i/dt = 0 \Leftrightarrow j_{L,C^+} = j_P$. Next we introduce a new variable ("*pump-leak ratio*") defined as:

$$\rho = k_P/k_{L,C^+} = k_P \cdot \frac{V_{cell}}{S_{cell} \cdot P_{C^+} \cdot [C^+]_{out}} \cdot e^{\frac{F \cdot V_m}{2 \cdot RT}} \tag{2.10}$$

and re-write the steady-state condition for C^+ as:

$$\left(1 - e^{\Delta G_{C^+}/(RT)}\right) = \rho \cdot \left(1 - e^{(\Delta G_E - \Delta G_{C^+})/(RT)}\right) \tag{2.11}$$

Given a certain extracellular composition ($[Dye]_{out}$, $[C^+]_{out}$ and $[A^-]_{out}$), and taking into account that $[Dye]_{in}$ and $[A^-]_{in}$ are defined by the Nernst equation at steady-state, equation (2.11) gives us a unique solution for steady-state V_m for a set of $\{[Y]_{in}, \rho, \Delta G_E\}$ values, while reducing the number of computational steps needed to reach it (see also the later paragraph describing computational steps of the model further).

We note from Eq. (2.11) that changing the functional dependency of k_{L,C^+} or k_P does not affect how the steady-state $V_{m,0}$ depends on ρ. However, the dynamics of dye equilibration and the steady-state potential after addition of the dye, relative to the steady-state potential in absence of the dye, ($\Delta V_m = (V_{m,0} - V_{m,Dye})/V_{m,0}$) do. For example, had we assumed that the mechanism by

which the ions leak across the *E. coli* membrane is better described by the Goldman–Hodgkin–Katz flux equation for $k_{L,x}$ Goldman, 1943, we would have obtained a slightly different dye equilibration profile (Fig. SI3). However, the conclusions we reach based on our model predictions will not change, because we are interested in the changes of the intracellular dye concentration dynamics at different extracellular dye concentrations, $V_{m,0}$ or P_{Dye}. These partial derivatives of the intracellular dye concentration are invariant to the choice of $k_{L,x}$ and k_P.

Having constructed the model, we obtain the computational data in Fig. 2.2 in two steps. In the first step we allow the ODE system described by Eqs. SI 20, 21 to reach the steady-state ($V_{m,0}$) for a 3-D grid of $\{[Y]_{in}, \rho, \Delta G_E\}$. We note that in this step we do not need to specify cation permeability nor the rate function for leakage k_{L,C^+}, because we define the values of ρ, which is the ratio of the two (ρ=0 for the anion and the dye). We then use the obtained $V_{m,0}$ as the initial condition for the second step of the numerical experiment, which requires us to specify: *(i)* the rate function for leakage (Eq. (2.9)), *(ii)* the permeability of the membrane to the dye P_{Dye} and *(iii)* the concentration of the dye in the extracellular space $[Dye]_{out}$, which does not affect the cation pumping rate in our model.

To explore the trade-offs imposed on a Nernstian dye (Fig. 2.1), we first look at the choice of the working concentration. Increasing the $[Dye]$ gives better signal-to-noise ratio, but can affect $V_{m,0}$, as depicted in Fig. 2.2A. For a fixed $V_{m,0}$, $[Y]_i$ and ΔG_E, changing the external dye concentrations ($[Dye]_{out}$) improves the signal-to-noise ratio and shortens τ_{eq}, but at the same time increasingly depolarizes the membrane. The extent by which ΔV_m drops does not solely depend on the $[Dye]_{out}$, but also on the initial $V_{m,0}$. Fig. 2.2B shows dye equilibration profile for a fixed $[Dye]_{out}$, but for different $V_{m,0}$ indicating that highly polarized cells are more susceptible to V_m loss. Apart from the value of $V_{m,0}$, ΔV_m will also depend on the charged permeable and non-permeable species that are generating it, as shown in Fig. SI4. If a given $V_{m,0}$ value is generated in the presence of a higher concentration of charged, impermeable intracellular species or at a higher energetic cost, ΔV_m will increase for the same $[Dye]_{out}$. Thus, the extent to which a given $[Dye]$ becomes an actuator and affects the ΔV_m is context dependant and the dye working concentration should be determined for each specific physiological condition. Additionally, Fig. 2.2A shows that increasing $[Dye]_{out}$ shortens τ_{eq}, but only when $V_{m,0}$ is

affected, as seen in Fig. SI5.

Lastly, we look at the dye equilibration profile for different permeabilities of the membrane to the dye (P_{Dye}) in Fig. 2.2C, and show that for higher P_{Dye} same concentration of the dye lowers $V_{m,0}$ more. Fig. SI4 shows τ_{eq} as a function of P_{Dye} for different $V_{m,0}$.

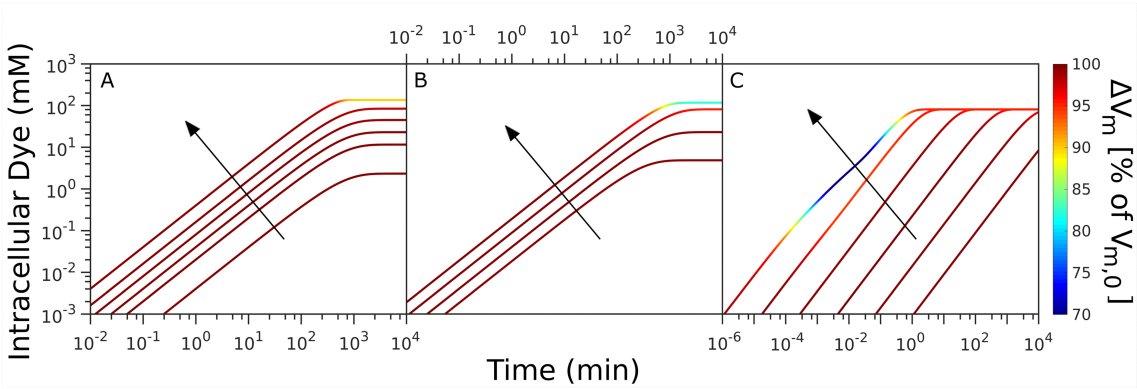

FIGURE 2.2: Computational data describing the parameter landscape associated with cationic dye usage as Nernstian sensors. (A) $V_{m,0} = -140$ mV, $Y_i = 150$ mM, $I_{Na} = 210$ mV. Intracellular Dye concentration as a function of time, for extracellular dye concentrations 10, 50, 100, 200, 400 and 1000 μM. The arrow indicated increasing $[Dye]_{out}$. (B) Extracellular dye concentration of 100 μM, $Y_i = 150$ mM, $\Delta G_E = -210$ mV. Intracellular dye concentration as a function of time, for different $V_{m,0}$: -220, -180, -140 and -100 mV. The arrow indicates increasing absolute value of the $V_{m,0}$. (C) Extracellular dye at 100 μM, $V_{m,0} = -180$ mV, $Y_i = 150$ mM, $\Delta G_E = -210$ mV. Intracellular dye concentration as a function of time, for different apparent permeabilities of the membrane to the dye: 10^{-12}, $10^{-10.8}$, $10^{-9.6}$, $10^{-8.4}$, $10^{-7.2}$, 10^{-6} m/s. The arrow indicates increasing permeability.

The working concentration of Nernstian dye Thioflavin T for *E. coli* is in μM range

Guided by the model predictions we devise an experimental work-flow for assessing the parametric range in which a candidate cationic dye behaves like an ideal Nernstian sensor. We choose Thioflavin T (ThT) for the purpose, it has recently been used as a V_m dye in *B. subtilis* (Prindle et al., 2015), but it has not been characterized for use in *E. coli*. We start by identifying the working concentration that gives sufficiently large signal, yet minimizes the membrane voltage perturbation, ΔV_m. Because we do not have access to ΔV_m directly we

grow the cells in the presence of ThT and use the growth rate as a proxy for affected ΔV_m. We also know from our model predictions that ΔV_m is context dependant, so we perform the experiment in two different media. Fig. 2.3A and B show *E. coli* growth curves in MM9 media supplemented with glucose or glycerol respectively (see *Materials and Methods* for detailed media composition), and in the presence of a range of ThT concentrations. To asses the effect of different ThT concentrations in these two media, we plot growth rates, obtained from growth curves in Fig. 2.3A and B, against the ThT concentration. Fig. 2.3C demonstrates that 10 μM ThT or less does not significantly affect the growth rate in either media, and we call this concentration MNC (Maximum Non-Inhibitory Concentration). The growth rate reduction we observe for higher ThT concentrations is media dependent (Fig. 2.3C). The result is consistent with the finding of our model that the effect of the dye on cell's physiology is environment dependent. It could be caused by a different $V_{m,0}$, difference in charged permeable and non-permeable species that achieve the $V_{m,0}$, difference in the initial membrane permeability or any combination of these factors.

We next check that the highest ThT concentration, which does not affect the growth rate (MNC), 10 μM, gives sufficiently high signal-to-noise ratio by observing the dye equilibration in different media. For this purpose we no longer grow the cells in the presence of ThT (see also *Materials and Methods*). We note that if sufficient ΔI is achieved with 10 μM ThT we would further check that $\Delta V_m < 1\%$ by measuring the τ_{eq} with both 10 μM and a lower dye concentration. If $\Delta V_m < 1\%$, we expect τ_{eq} not to change based on the results of our model (Fig. 2.2A). Fig. 2.3D shows I_{in} in time in LB and Fig. 2.3E the same in MM9 media supplemented with glucose. In both cases fresh media with ThT is continuously supplied using a customized flow-cell (see *Materials and Methods*), and in both cases ΔI is sufficiently high. However, observed profiles are different from expected (Fig. 2.1), and show a characteristic initial peak and a subsequent large increase that plateaus (SI Video 3). We reasoned that the peak could either be a real fluctuation in V_m or it could indicate an unknown dye export mechanism.

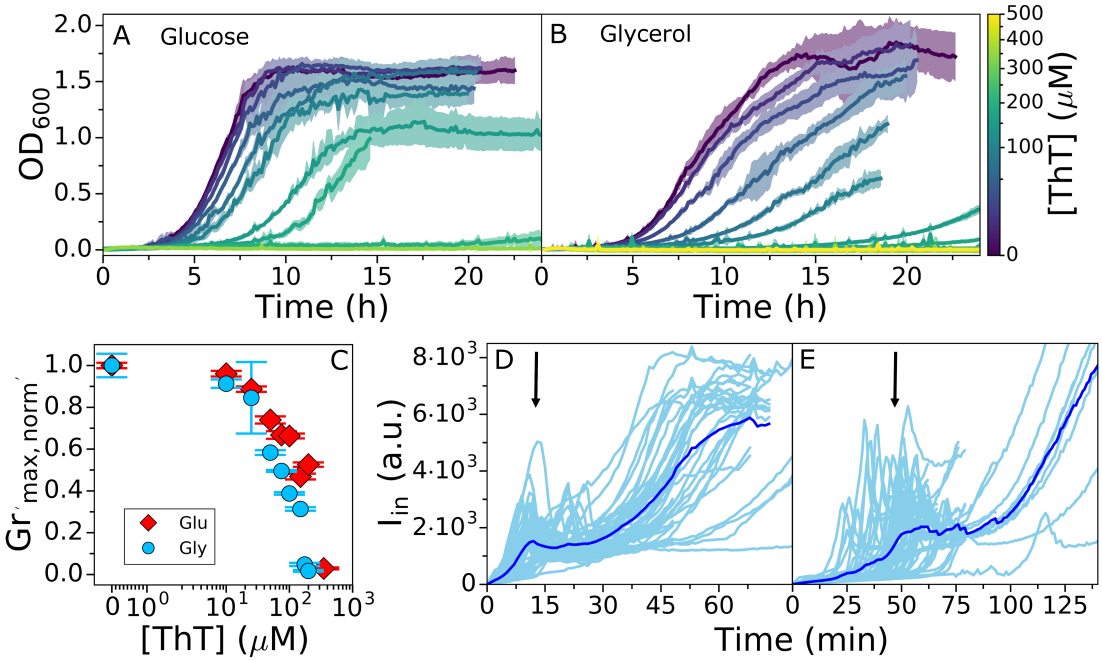

FIGURE 2.3: *E. coli* growth in the presence of ThT. *E. coli* growing in MM9 media supplemented with (A) glucose or (B) glycerol at increasing ThT concentration (colour-map). ThT concentrations in (A) are 10, 25, 50, 75, 100, 200, 350 μM and in (B) 10, 25, 50, 75, 100, 150, 175, 200 μM. The error bars are standard deviations. (C) Maximum growth rates from (A) and (B) for each ThT concentration are given in red and blue respectively. Each condition was done at least in triplicate and error bars are the standard deviation. (D) I_{in} against time in LB and in (E) MM9 + glucose media. Individual cells are shown in cyan (45 in (D) and 52 in (E) from at least 9 independent experiments), and the average trace is shown in blue. The imaging conditions and $I_{ex} = 10\mu M$ are the same for (E) and (D). The black arrows indicate the intensity peaks.

Deletion of the multi-drug efflux pumps component TolC influences ThT dynamics in *E. coli*

To determine whether the observed peak in I_{in} is due to active export of the dye we first check that in *E. coli* ThT is not a multi-drug-efflux pump substrate. We are motivated by previous reports that show dyes, such as ethidium bromide and Nile red, are substrates of pumps belonging to the five bacterial structural families: ABC (ATP-binding cassette), RND (resistance/nodulation/division), MATE (multidrug and toxic compound extrusion), MFS (major facilitator superfamily) and SMR (small multidrug resistance) (Alvarez-Ortega et al., 2013; Lubelski et al., 2007; Nikaido et al., 2009; Kuroda et al., 2009; Bay et al., 2008). Fig. 2.4A shows dye equilibration curves in a wild type (WT) strain compared

to the strain bearing a deletion of TolC, which is a gene encoding for an outer membrane protein (OMP) that is a ubiquitous component of multi-drug efflux pumps (Anes et al., 2015). The I_{in} peak in the deletion mutant did not disappear, instead the intensity level of the peak was even higher, suggesting that the qualitative difference between the expected (Fig. 1) and the observed equilibration curve (Fig. 4A) is not due to ThT export by TolC. Interestingly, in the mutant, the peak also occurred earlier in time during the loading and with less cell-to-cell variability. We next tested the effect of the ThT dye on the Δ*TolC* mutant growth rates, and for this purpose we again grew the two strains in the presence of ThT, Fig. 2.4B. We found that at the MNC for the WT, the mutants' growth was inhibited over the course of our experiment. Two different mechanisms could explain the results in Fig. 2.4: (i) ThT is a substrate of the multi-drug efflux pumps or (ii) membrane permeability of the TolC mutant is higher (Dhamdhere et al., 2010). In the first scenario, the strain lacking TolC accumulates more ThT than the WT (Fig. 4A), and is therefore more affected by it (Fig. 4B). In the second scenario, based on our model, we expect the intensity peak to appear earlier and at a higher $[Dye_{in}]$ (Fig. SI12 C and D), which is what we observe in Fig. 2.4A. We currently cannot distinguish between the two hypothesis, which could be contributing to the observed equilibration profiles at the same time.

Changing the membrane permeability during ThT loading can lead to loss of V_m

We next tested our second hypothesis that the I_{in} peak is due to a decrease in V_m. To this end, we performed measurements of bacterial flagellar motor (BFM) speed (Krasnopeeva et al., 2019) during ThT loading. BFM is a rotary molecular motor roughly 50 nm in size that enables bacterial swimming (Sowa et al., 2008) via PMF driven rotation (**Manson1980**; Matsuura et al., 1977; Meister et al., 1987; Fung et al., 1995). The motor speed (ω) varies linearly with PMF (Fung et al., 1995; Gabel et al., 2003b), which enables its use as a PMF indicator, and when $pH_{in} = pH_{out}$, as a V_m indicator as well (Krasnopeeva et al., 2019). In our conditions, pH_{out} is 7 and pH_{in} is 7.86 (Fig. SI7) making the contribution to the PMF from ΔpH ∼50 mV. Thus, even if during our experiment ΔpH goes to 0, we can learn about the V_m behaviour from the PMF measurements via the motor speed. We measure ω as before, using back-focal-plane interferometry

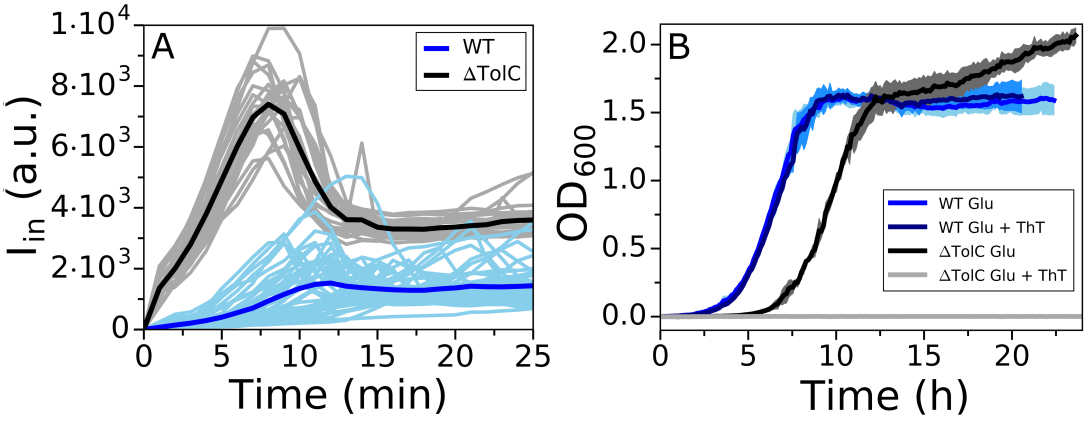

FIGURE 2.4: Comparison of WT and ΔTolC mutant response to ThT. (A) I_{in} versus time for the WT (cyan) and ΔTolC (gray) loaded in LB. WT traces are reproduced from Fig. 3D and ΔTolC traces were obtained from 5 independent experiments to give 23 single cell traces. Averaged traces for the WT and ΔTolC are given in blue and black respectively. (B) Growth curves of WT and ΔTolC in MM9 + glucose media are given in blue (reproduced from Fig. 2.3A) and black, respectively. Growth curves in the same media, but in the presence of 10 μM ThT, are given in cyan (WT) and gray (ΔTolC). The shaded areas show standard deviation and cyan and blue growth curves for the WT overlap.

(Svoboda et al., 1993) and a polystyrene bead attached to a short filament stub (see *Materials and Methods*) (Krasnopeeva et al., 2019; Rosko et al., 2017; Ryu et al., 2000; Bai et al., 2010).

Fig. 2.5A and Fig. SI8 show simultaneous measurements of ThT intensity and normalized motor speed during dye equilibration in MM9 + glucose. The motor speed decreases during ThT equilibration and BFM stops at the point of I_{in} peak. Furthermore, BFM does not resume spinning even as I_{in} further increases, suggesting that the second ThT intensity increase that culminates in a plateau, is not driven by V_m. To confirm the result, during ThT equilibration, we supplemented the medium with propidium iodide (PI). PI permeates bacterial membrane that lost its integrity and significantly enhances its quantum yield upon binding to DNA, which is commonly interpreted as an indication of cell death (Lopez-Amoros et al., 1995; Krämer et al., 2016). We found that the cells stained with PI although ThT intracellular concentration remained high, Fig. 2.5B and Fig. SI9. In addition, at the time point of I_{in} decrease cellular volume suddenly increases, and cytoplasmically expressed fluorescent protein mCherry-mKate2 hybrid (referred to as mKate2 for brevity) (Lord, 2014) starts leaking out of the cell, Fig. 2.5C, SI Video 4.

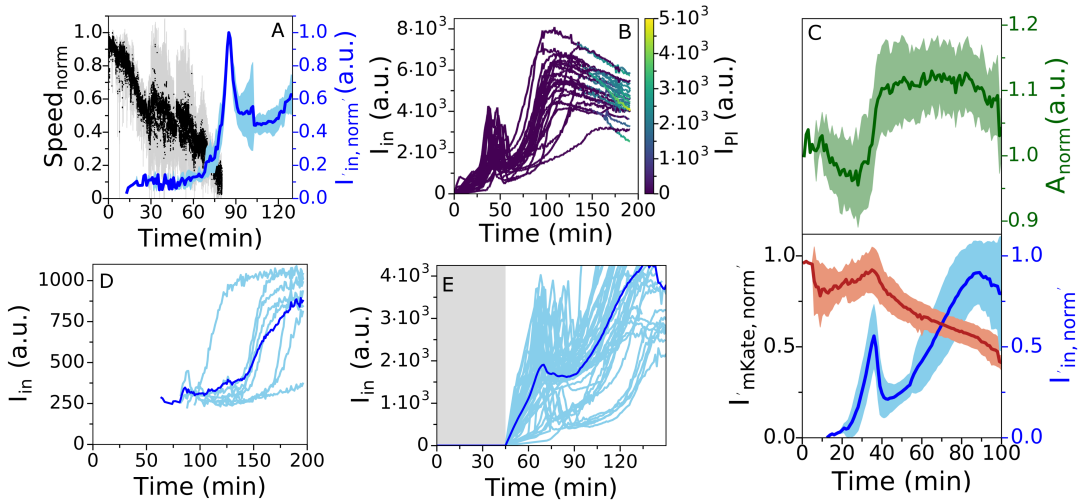

FIGURE 2.5: (A) Average traces of ThT fluorescence (in blue) and motor speed (in black) simultaneously measured in 5 individual cells (individual cell traces are given in Fig. SI6). The shaded areas show the standard deviation and the motor speed has been normalized to the initial value as described in *Materials and Methods*. (B) ThT (y axes) and PI (colour-map) equilibration profile in LB. 25 individual traces are given. (C) Average of ThT (in blue), mKate2 (in red) fluorescence and cell area (in green) simultaneously measured in 12 individual cells from 3 independent experiments. The shaded areas show the standard deviation. (D) Equilibration profile of 1 μM ThT in LB. 8 single cell traces and average trace are given in cyan and blue, respectively. (E) Equilibration profile of 10 μM ThT in LB in the absence (gray shaded area) and presence of epifluorescent illumination (light area). The dye was flown in the flow cell for the whole length of the experiment, imaging conditions in the light area were the same as in Figure 3 and 5D. 44 cells from 8 independent experiments are given.

These results are in contradiction with our estimate of dye working concentration, and we wondered, based on Fig. 2.2C, if the changes in P_{Dye} could be the explanation. The cell culture in Fig. 2.3 was briefly exposed to light at 600 nm every 7.5 min, whereas cells in our flow-cell were exposed to light of 435 nm every minute for the purpose of imaging the ThT dye. We have previously reported loss of V_m and PMF due to light-induced decrease of *E. coli* membrane's resistance at effective powers higher than ~ 17 mW/cm^2, and for a combination of 395 and 475 nm wavelengths (Krasnopeeva et al., 2019). Light damage is wavelength dependent (Vermeulen et al., 2008), and we therefore characterized the light damage caused by our imaging conditions, i.e. 435 nm wavelength and effective power of $P_{eff} \sim 11$ mW/cm^2. Fig. SI10 shows a decrease in BFM motors' speed, and thus cell's PMF. However, the PMF is not

fully lost, indicating that the loss of PMF observed in Fig. 2.5A is likely caused by the combination of light induced increase in P_{Dye} and exposure to 10 μM ThT.

To prove it, we exposed the bacteria to 10 μM ThT in LB as before, but this time we observe the cells under bright-field illumination for 45 min, at which point we turn on the 435 nm light used for epifluorescence imaging of ThT. Fig. 2.5E shows that after 45 min, cells not exposed to 435 nm light did not take up ThT. This is in contrast to Fig.2.3D where cells exposed to 435 nm light from the start, took up ThT in the first 30 min.

Actively changing membrane permeability has been used to facilitate loading of Nernstian sensors (Lo et al., 2007b), and Fig. 2.5E shows that this can change the dye into an actuator because it can influence V_m. Our mathematical model predicts that if a given concentration of the dye is lowering V_m, an even lower concentration of the dye will result in a change of τ_{eq} (Fig. SI5). Because the dye equilibration profiles in Fig. 2.3D do not follow the theoretically expected curve (Fig. 2.1) we cannot calculate τ_{eq}. However, from Fig. 2.5A we know that initial rise in the dye intensity is still driven by V_m, therefore we can qualitatively compare the timing of the initial rise at different $[Dye]_{out}$. Fig. 2.5D shows that for 1 μM concentration of ThT the rise in I_{in} happens later in time than at $[Dye]_{out} = 10\mu$M (Fig. 2.3D). Thus, 10 μM ThT in LB, under 435 nm light, affects V_m. Assessing the suitability of the dye working concentration by confirming that a lower dye concentration does not alter τ_{eq} is a suitable additional control we propose, especially if P_{Dye} is being altered as part of the experiments.

We note that in our plate reader experiments (Fig. 2.2) we observed the effect of the dye (above 10μM) on cell growth, while in our microscopy experiments, in the absence of light damage, ThT does not permeate WT cells. We thus wanted to confirm that at higher concentrations ThT permeates the cells on a longer time scale, and for the purpose we imaged the cells from the wells at representative ThT concentrations in MM9+glucose (10, 50 and 100 μM) and MM9+glycerol (10 μM). As expected, we found that on a longer time scale in MM9 glucose cell brightness increases with the extracellular dye concentration and that in MM9+glycerol, at 10μM, ThT signal from the cells is overall greater than in glucose (Fig. SI11).

Having identified the mechanisms behind the shape of the ThT loading curve we observed in Fig. 2.3 we should now be able to reproduce it with our

mathematical model. We focus only on the part of the equilibration curve that is V_m driven, i.e. up to the point V_m drops to zero (as indicated in Fig. Fig 2.5A). Beyond, the increase in I_{in} is not driven by Nernstian equation, and thus not accounted for in our model. Based on Fig 2.5A we assume that V_m decays exponentially immediately after addition of the dye (Krasnopeeva et al., 2019): $V_m(t) = V_{m,0} \cdot 2^{t/t_{1/2}}$ where $t_{1/2}$ is the time at which voltage is half that of $V_{m,0}$. The dynamics of dye entry are then modelled by Eyring's rate law Eq. (2.9) taking into account $V_{m,0}$, $t_{1/2}$ and P_{Dye} (see *Supplementary Information* for further details on the model). Fig. SI12 shows that the model reproduces the peak in $[Dye]_{in}$ observed in Fig. 2.3. Immediately upon addition, the positively charged dye moves inwards because its extracellular concentration is higher than the intracellular and the cell is negatively polarized. Thus, $[Dye]_{in}$ increases and becomes greater than $[Dye]_{out}$ until the electrochemical potential reaches $\Delta G_{Dye} = 0$ (at the peak). As the V_m decays and since $[Dye]_{in} > [Dye]_{out}$, the dye now starts moving outwards and its intracellular concentration decreases. In Fig. SI12B $[Dye_{in}]$ decreases to zero, while experimental I_{in} starts increasing after the peak and never reaches zero. The difference is explained by the fact that cells with high I_{in} after the peak are no longer viable (Fig. 2.5A and Fig. 2.5B) and thus the behaviour of the dye is no longer governed with Nernstian equation. In Fig. SI12E and F we indicate the part of the experimental equilibration curve to which our model is applicable.

The time at which the peak occurs as well as its intensity depend on P_{Dye} as follows: *(i)* the time of the peak decreases with increasing P_{Dye} and increases with increasing $t_{1/2}$, and *(ii)* the intensity of the peak increases with increasing P_{Dye} and $t_{1/2}$, Fig SI9 C and D. The dye still equilibrates according to equation (2.2), however, this is achieved transiently at the time of the peak, which is the time point at which V_m can be calculated from equation (2.2). Since the V_m varies during the course of the experiment, the V_m measured at the peak is not equal to the $V_{m,0}$. Nonetheless, if we measure $V_m(t)/V_{m,0}$ as well as calculate the V_m at the time of the peak using eq. (2.2), in principle we can estimate $V_{m,0}$ as well. Therefore, charged dyes can be used to estimate initial V_m even in conditions where they act as actuators and collapse V_m, if the dynamical shape of the V_m loss is known.

Discussion

Nernstian probes are a popular choice for estimating bacterial V_m, because the concentration of the free dye directly depends on V_m according to the Nernst equation. Despite the wide usage, the probes are often not sufficiently calibrated before use in different conditions. Here we present a mathematical model that shows trade-offs between requirements imposed on the dye: sufficient signal-to-noise ratio, sufficiently short dye equilibration time and minimum effect on the cells' physiology. Based on the model results we characterize in *E. coli* the fluorescent dye Thioflavin T, recently used in *B. Subtilis* (Prindle et al., 2015). Finally, we propose a general work-flow for the characterization of Nernstian dye candidates (Fig. 2.6).

Results of our model show that the dye working concentration which does not affect V_m is context dependant, e.g. it can be different for different external media. The model also predicts that if $\Delta V_m = 0$ at a chosen dye working concentration, lower dye concentration should leave τ_{eq} unchanged. The finding offers a simple test to confirm the suitability of the chosen dye working concentration.

For the case of *E. coli* and ThT as the candidate Nernstian dye, we experimentally find that the dye equilibration profile does not follow the theoretical expectation (Fig. 2.1). We test two possible explanations for the shape of the equilibration profile we observe in Fig. 2.2: (a) involvement of active efflux pumps and (b) significant V_m decrease during ThT equilibration. While we find that the strain lacking one of the efflux pumps shows a different equilibration profile when compared to the wild type, it still does not behave as theoretically expected. Instead, we find that the permeability of *E. coli's* membrane to ThT is low. Permeabilizing the membrane by light of relatively short wavelengths to facilitate sufficient ThT entrance into the cell causes significant V_m reduction, which subsequently results in cell death. The finding is consistent with previous results that show that *E. coli*'s membrane needs to be permeabilized with EDTA to achieve experimentally reasonable loading times of TMRM dye (Lo et al., 2007b). EDTA is thought to increase the permeability of *E. coli* by chelating the metal ions that cross-link the LPS (Vaara, 1992). Some evidence also suggests that it might interact directly with lipids destabilizing the membrane (Prachayasittikul et al., 2007). The equilibration profiles we observe for the efflux pump mutant strain can be explained either by the change

in membrane permeability between the two strains or by active efflux.

We summarize the results from our model and experiments, as well as previous work on Nernstian V_m dye usage, in a work-flow (Fig. 2.6). We believe it is sufficiently simple and general to provide a common standard for benchmarking the cationic dye behavior and thus improve the robustness of V_m measurements. It starts with a protocol to identify the dye working concentration (Fig. 2.6, steps 1-4). This is first carried out by assaying the effect of the dye on bacterial growth, as we did in Fig. 2.3A-C, because it is a physiological variable that is easy to measure and it will likely be affected by changes in V_m (step 1). In step 1 we identify the Maximum Non-inhibitory Concentration (MNC), as the maximum dye concentration that does not affect growth. We use it to measure the dye equilibration profile in step 2. This allows us not only to make sure that with the MNC we are obtaining the expected shape of the equilibration profile, but also that the MNC gives sufficiently high intracellular signal. Next, we further test, as we did by comparing Fig. 2.3D and 2.5D, whether the MNC is affecting V_m by checking that τ_{eq} for the MNC and a chosen concentration below it, stay the same (step 3). If the below-MNC concentration and the MNC do not show the same τ_{eq}, steps 1 to 3 need to be repeated for progressively lower dye concentrations until either the signal from the intracellular dye becomes too low, or τ_{eq} do not differ between the two tested concentrations. In the second case, the higher concentration can be considered suitable. The next step in the work-flow is more commonly performed when assaying V_m dyes (Felle et al., 1980; Lo et al., 2007b), where cells' V_m is changed in a known way, e.g. by exposing the cells to ionophores and observing V_m collapse (step 5). Finally, quantifying V_m requires estimation of $[Dye]_{in}$ from I_{in} measurements, which can be done by distinguishing the free from the bound dye and by taking into account that the obtained I_{in} is a convolution of $[Dye]_{in}$ and the microscope point spread function (Ehrenberg et al., 1988; Lo et al., 2007b) (step 6). As the dye's behaviour is context dependent, steps 1-6 should be repeated for each new experimental condition. Furthermore, if the dye fails any of the steps in the proposed work-flow, it is not suitable for use as a Nernstian sensor. For example, ThT for the case of *E. coli* failed in steps 2 and 3, which is why we did not need to perform subsequent steps of the work-flow.

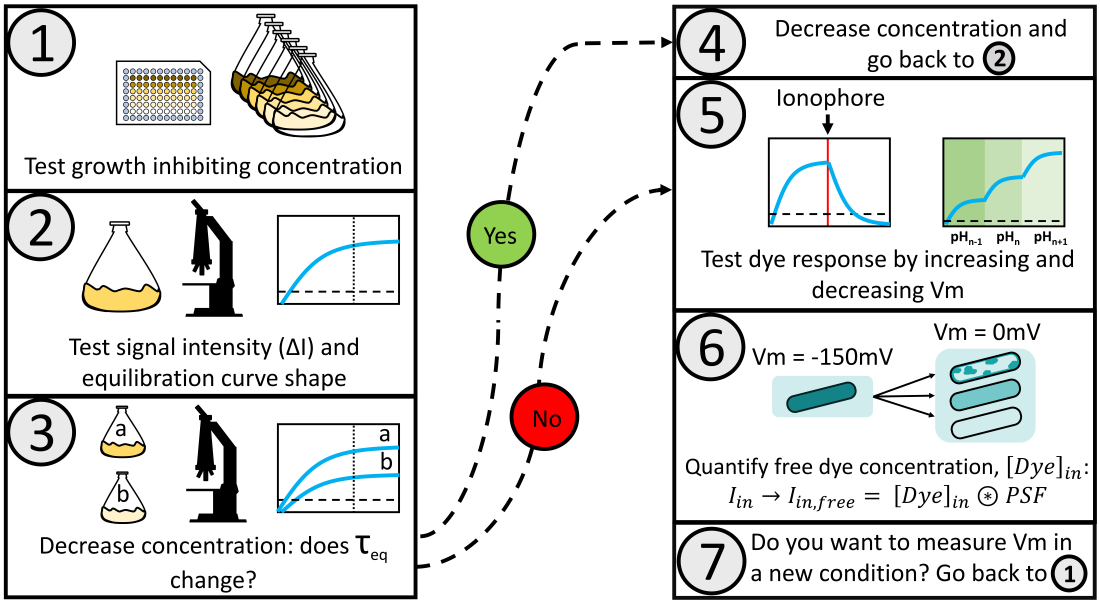

FIGURE 2.6: Proposed work-flow for characterizing the Nernstian behavior of a candidate cationic membrane voltage dye. The working concentration is estimated in steps 1 to 4, we define it as the maximum dye concentration that does not affect membrane voltage and that yields sufficient amount of signal. (1) The MNC is estimated. (2) The MNC is tested for sufficient signal intensity and the shape of the equilibration profile is inspected. (3) The effect of the dye on V_m is determined by measuring τ_{eq} at different below-MNC concentrations. (4) Different τ_{eq} for different dye concentrations indicate that the probe is altering V_m and the working concentration should be reduced and the protocol resumed from (2). Equal τ_{eq} indicates that the probe is not altering V_m. (5) Common procedures to test the expected Nernstian dye responses can then be applied, such as the introduction of a ionophore that neutralizes V_m, or changes in external pH that induce changes in V_m (Lo et al., 2007b). (6) I_{in} from the free dye should be separated from the I_{in} from the bound dye, and $[Dye]_{in}$ should be calculated from I_{in} by taking into account the microscope's points spread function. (7) Because the effects depend on the physiological state of the cell, the procedure should be repeated for every experimental condition.

Author Contributions

LM, GT, CJL, BF and TP conceived the experiments and the computational work. LM, TT, YP and YL performed experiments. GT performed computational work. LM analyzed experimental data, and LM, GT, CJL, BF and TP interpreted the results and wrote the manuscript.

Acknowledgements

We thank Dario Miroli for help with image analysis, Nathan Lord and Sebastian Jaramillo-Riveri for donating us the construct containing the hybrid mCherry-mKate2 sequence and Angela Dawson for retrieving the ΔTolC mutant from the Keio collection. This work was financially supported by the Cunningham Trust scholarship ACC/KWF/PhD1 to TP and LM, the National Natural Science Foundation of China under grants No. 31722003 and No. 31770925 to FB, the Ministry of Science and Technology, Republic of China, under contract No. MOST-107-2112-M-008-025-MY3 to CJL and Human Frontiers Program grant RGP0041/2015 to TP, FB and CJL. TP acknowledges the support of UK Research Councils Synthetic Biology for Growth programme and is a member of the BBSRC/EPSRC/MRC funded Synthetic Biology Research Centre (BB/M018040/1).

Supplementary Figures

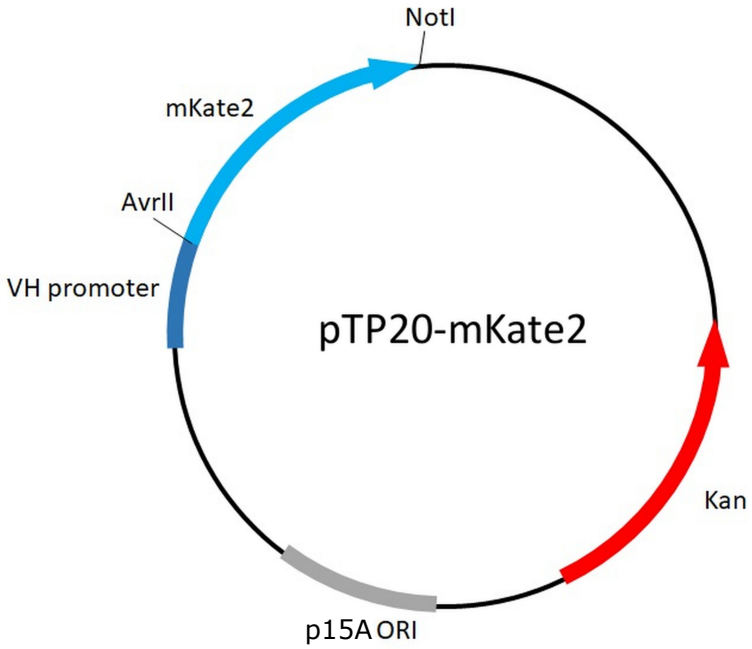

FIGURE 2.7: Plasmid map of pTP20-mKate2 showing the insertion site of mCherry-mKate2 hybrid (mKate2 for brevity) (Lord, 2014). The constitutive cytochrome oxidase promoter from *Vibrio Harveyi* (Pilizota et al., 2012), the origin of replication and the Kanamycin resistance cassette are indicated.

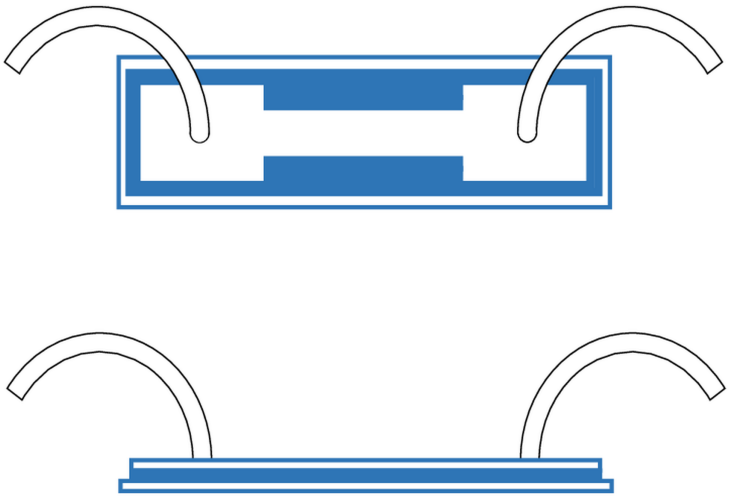

FIGURE 2.8: Schematic of our flow-cell. Microscope slide and coverslip are held together by custom cut Gene Frames (Thermo Fisher Scientific, UK). To exchange liquids, we drill two holes on the microscope slide and attach tubing using epoxy glue on the outside of the slide (Krasnopeeva et al., 2019).

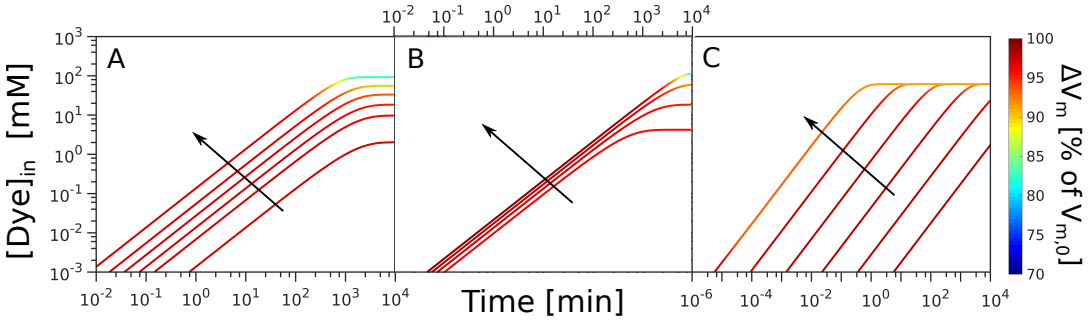

FIGURE 2.9: Dynamics of the dye loading assuming GHK rate law for leakage (Eq. (2.25)), where we assumed Eyring rate (law Eq. (2.24)) in Fig. 2 of the main text. (A) Intracellular Dye concentration as a function of time, for extracellular dye concentrations 10, 50, 100, 200, 400 and 1000 μM. The arrow indicated increasing $[Dye]_{out}$, and $V_{m,0} = -140$ mV, $Y_i = 150$ mM, $\Delta G_E = -210$ mV. (B) Intracellular dye concentration as a function of time for different $V_{m,0}$: -220, -180, -140 and -100 mV. The arrow indicates increasing absolute value of the $V_{m,0}$, and $[Dye]_{out} = 100$ μM, $Y_i = 150$ mM and $\Delta G_E = -210$ mV. (C) Intracellular dye concentration as a function of time for different apparent permeabilities of the membrane (with respect to the dye): 10^{-12}, $10^{-10.8}$, $10^{-9.6}$, $10^{-8.4}$, $10^{-7.2}$, 10^{-6} m/s. The arrow indicates increasing permeability, and $V_{m,0} = -180$ mV, $Y_i = 150$ mM, $\Delta G_E = -210$ mV and $[Dye]_{out} = 100$ μM.

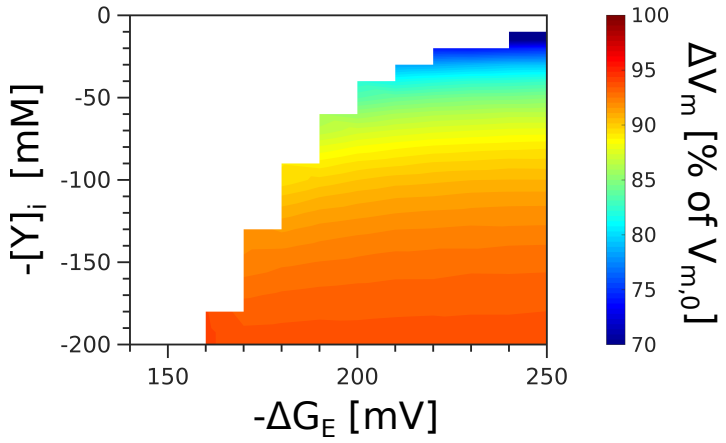

FIGURE 2.10: ΔV_m depends on the free energy available for transport of $[C^+]$ as well as on the contribution of charged impermeable species ($[Y_i]$), even for the same value of $V_{m,0}$. $[Dye]_{out} = 100$ μM. $V_{m,0} = -180$ mV. Colour scale on the right gives ΔV_m values.

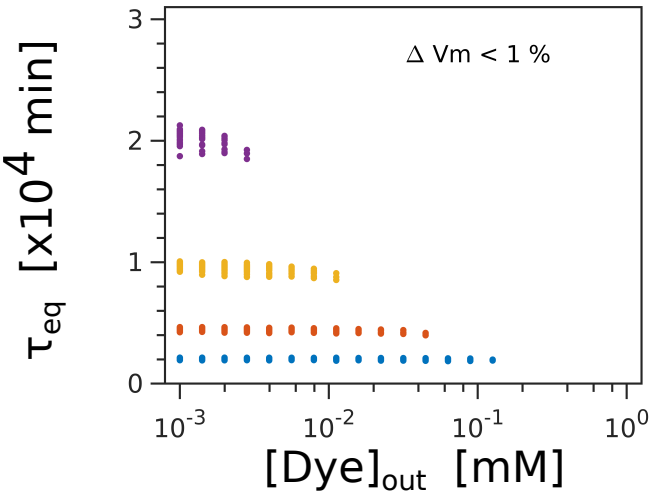

FIGURE 2.11: Equilibration time, τ_{eq}, as a function of $[Dye]_{out}$ for different $V_{m,0}$ values. The permeability of the dye was set to $P_{Dye} = 10^{-10}$ m/s. Purple, yellow, red and blue are $V_{m,0}$ of -220, -180, -140 and -100 mV (± 5 mV), respectively. For each value of $[Dye]_{out}$ we plot all the values of τ_{eq} that yield the desired $V_{m,0} \pm 5$ mV, where $\{[Y]_{in}, \rho, \Delta G_E\}$ were varied in the range specified in Table 2.4. The simulations that change $V_{m,0}$ by less than 1% mV are plotted, showing that when $\Delta V_m \sim 0$, τ_{eq} is a function of $V_{m,0}$ only.

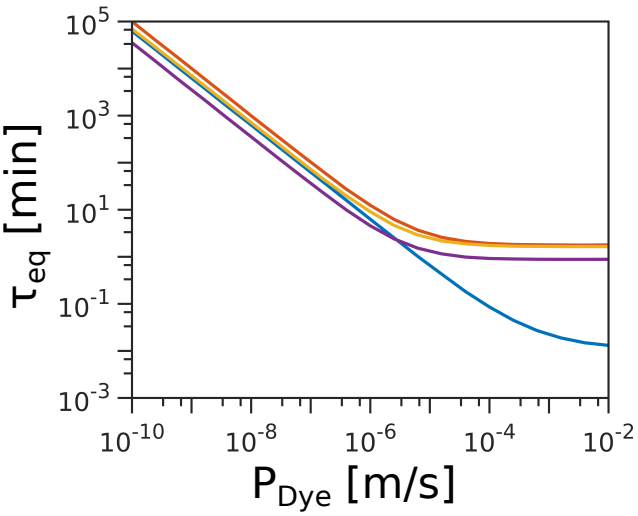

FIGURE 2.12: Equilibration time, τ_{eq}, as a function of the dye permeability. The following were set: $[Y]_i = 150$ mM, $\Delta G_E = -210$ mV, $[Dye]_{in} = 100$ μM. The blue, red, yellow and purple lines are for $V_{m,0}$ of -220, -180, -140 and -100 mV, respectively. For each of them, ΔV_m is permeability invariant and takes the respective values of 83%, 93%, 96% and 97%.

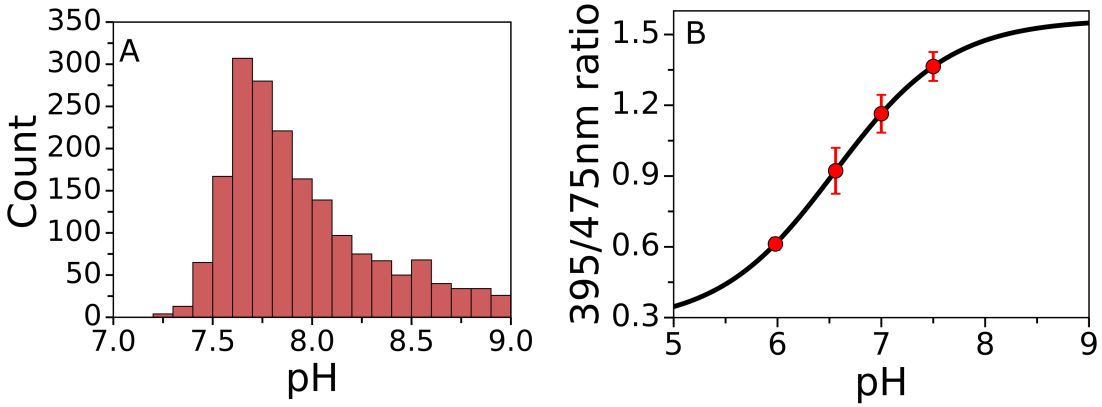

FIGURE 2.13: Intracellular pH measurements. (A) Using chromosomally expressed pHluorin (Krasnopeeva et al., 2019; Wang et al., 2019) we measure intracellular pH in 2346 individual cells. The median value of the distribution is 7.86. (B) *In vivo* pHluorin calibration curve where the cells were exposed to 40 mM potassium benzoate and 40mM methylamine hydrochloride in order to collapse internal pH (Wang et al., 2019). Data points are an average of ∼400 cells and error bars give the standard deviation.

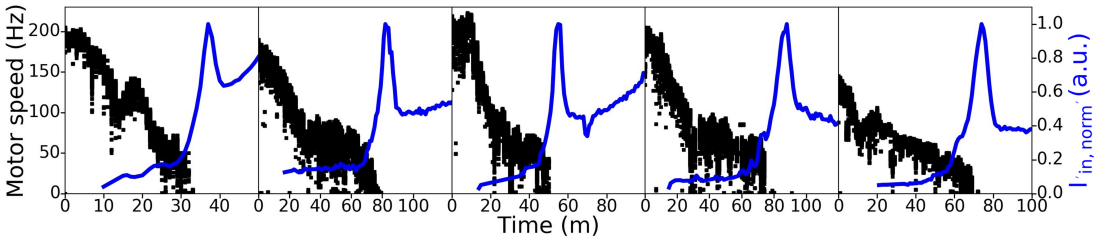

FIGURE 2.14: Individual motor traces (black) that were averaged in Fig. 5A. ThT intensity traces are given in blue, and imaging and exposure setting are as specified in *Material and Methods*.

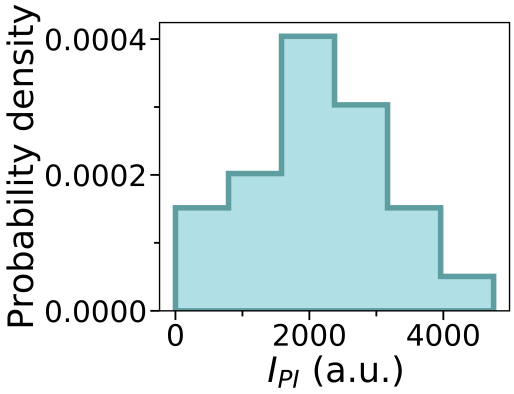

FIGURE 2.15: Probability density function of the final intensity values of propidium iodide from Fig. 5B ($I(t_f)$ with t_f = 185 min). Cell count is 25 from 3 different experiments.

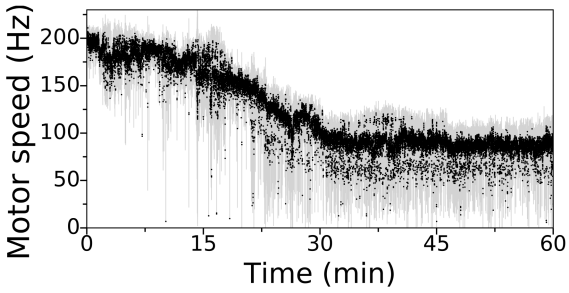

FIGURE 2.16: Light-induced damage quantified by measuring PMF loss via bacterial flagellar motor speed, over the length of an hour. The experiment was carried out as in Fig. 5A, but ThT was not added to the MM9 + glucose media, which was continuously supplied through out the experiment with a flow rate of 50 μl/min. Black shows the average of three individual motor speed recordings, each on a different cell, and grey area shows the standard deviation.

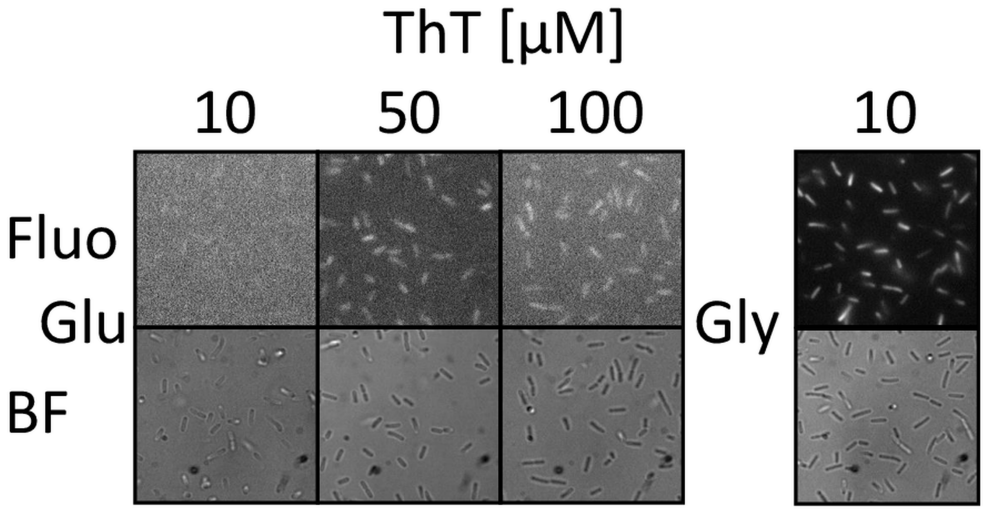

FIGURE 2.17: Cells grown in the plate reader (Fig 3A, B and C) in the presence of ThT were imaged, in order to estimate the extent of dye equilibration. "Fluo" abbreviation indicates fluorescence intensity and "BF", the brightfield image. Imaging conditions for ThT are the same as those used throughout the paper (Fig.3D E, 4A, 5A, B, C D). Cells were imaged after 7 h of growth in the plate reader (OD= 0.5- 0.6 when grown on glucose and 0.4 on glycerol) when 10 and 50 μM ThT was present, and after 8.5 h (OD 0.7 when grown on glucose) for the 100 μM ThT case.

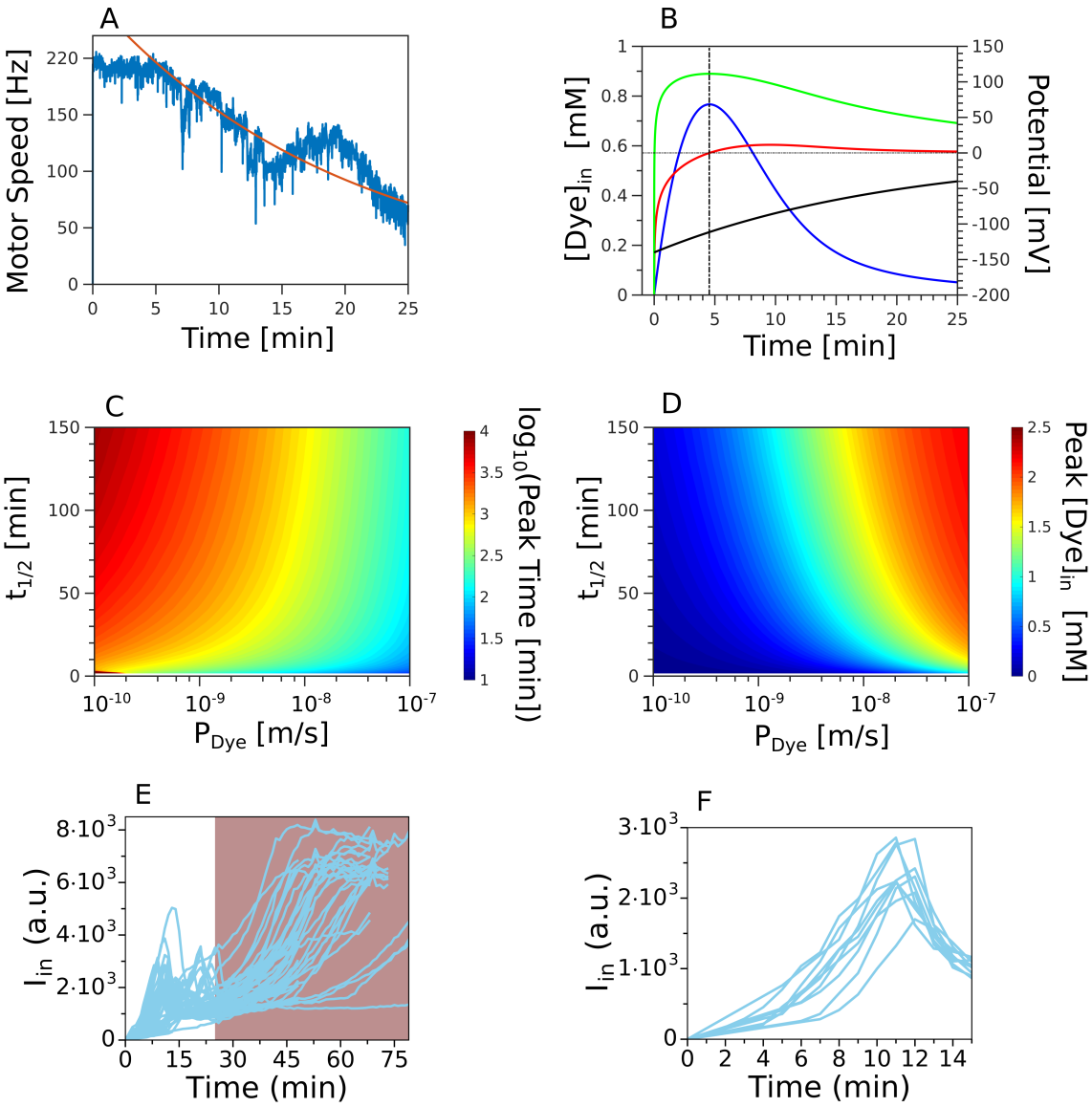

FIGURE 2.18: (A) Exponential decay of V_m during ThT loading leads to an intensity peak. Exponential fit (in red and starting from the time we observe the decay) to the first motor speed trace shown in Fig. SI5. The half-time of the decay is $t_{1/2} = 16.4$ min, which we use as the decay time of V_m. (B) Dye equilibration profile for the case of exponentially decaying V_m (black) is plotted in blue. The permeability of the dye was set to $P_{Dye} = 10^{-8}$ m/s, $[Dye]_{out} = 10^{-2}$ mM, and $V_{m,0} = -140$ mV. Green line depicts the contribution of the concentration gradient to the dye electrochemical potential $\ln([Dye]_{in}/[Dye]_{out})$ and red line the electrochemical potential of the dye. (C) Peak time (in log scale) and (D) peak intracellular dye concentration as a function of $t_{1/2}$ and the dye permeability. For both (C) and (D) we assumed $V_{m,0} = -140$ mV. (E) The model is relevant for the part of the equilibration profile that is driven by V_m. Subsequent increase in ThT intensity (shaded in red) does not obey Nernstian equation, because V_m is zero (Fig. 5A) and cell membrane is compromised (Fig. 5B). The traces are reproduced from Fig. 3D. (F) 10 example traces from Fig. 3D showing the portion of the equilibration curve described by our model.

Supplementary Tables

Plasmid	Fragment	Primers
pTP20-mKate2	pWR20 backbone (Pilizota et al., 2012)	5′ AAAGCGGCCGCGGTGATTGATTGAGCAAG 3′ 5′ AAACCTAGGATGTATATCTCCTTAACTAGGT 3′
pTP20-mKate2	mCherry-mKate2 hybrid (Lord, 2014)	5′ AATGCGGCCGCTTATCTGTGCCCCAGTTT 3′ 5′ ATACCTAGGATGGTTAGTAAAGGAGAAGAA 3′

TABLE 2.1: Plasmids and primers used in this work.

Strain	Origin	Figure
MG1655		3, 4A, 5B, 5E, 5D and SI 2, 9
MG1655-*pTP20-mKate2*	This work	5C
EK01	(Krasnopeeva et al., 2019)	5A and SI 4,5,7
EK07	(Krasnopeeva et al., 2019)	SI 10
BW25113 Δ*tolC* pTP20-mKate2	This work	4A, 4B

TABLE 2.2: List of *E. coli* strains used in this work.

Name	Symbol	Value	Units	Reference
Faraday constant	F	96485	C/mol	
Gas constant	R	8.31	J/mol/K	
Temperature	T	298	K	
Avogadro Number	N_A	6.02×10^{23}	mol^{-1}	
Cell length	l_{cell}	2.95×10^{-6}	m	Basan et al., 2015
Cell width	w_{cell}	1.07×10^{-6}	m	Basan et al., 2015
Cell surface	S_{cell}	9.91×10^{-12}	m^2	Eq. SI(2.14)
Cell volume	V_{cell}	2.33×10^{-18}	m^3	Eq. SI(2.15)
Membrane Specific Capacitance	C_m	6.5×10^{-3}	F/m^2	Bai et al., 2006
Total Membrane Capacitance	C	6.45×10^{-14}	F	Eq. SI(2.13)
Total Extracellular ionic concentration	Π_e	200	mol/m^3	
Membrane Permeability to C^+	P_{C+}	1.8×10^{-9}	m/s	Costa et al., 1989 (K^+)
Membrane Permeability to A^-	P_{A-}	1.4×10^{-10}	m/s	Costa et al., 1989 (Cl^-)

TABLE 2.3: Parameters used for the simulations. The cell length and width in MM9+glucose were obtained from our fluorescence microscopy measurements and are consistent with Basan et al., 2015.

Sampled parameters	Range of values	Spacing	Number of values
ΔG_E	$-250\text{mV} \leq \Delta G_E/F \times 10^{-3} \leq -50\text{mV}$	Linear	21
$[Y]_{in}$	$0 \leq [Y]_{in} \leq 200$ Moles/meter^3	Linear	21
ρ	$10^{-4} \leq \rho \leq 10^5$	$\log_{10}$	1000

TABLE 2.4: Value of parameters used when solving Eqs. SI 20 and 21 to obtain $V_{m,0}$.

Supplementary text

Supplementary methods

Intracellular pH estimation.

To estimate the intracellular pH we used *EK07* cells grown to OD 0.8 in TB at 30°C and transferred to MM9 + glucose media, as for the experiments in Fig. 5A and as in (Rosko et al., 2017). Imaging was carried out in a flow-cell with a 50 ms exposure time and gain set to 300. Illumination at 395 nm and 470 nm was provided by a narrow spectrum UV LED and a Neutral White LED (Cairn Research Ltd, UK), respectively (Krasnopeeva et al., 2019). The filters used were ET470/40x and ET525/40m (Chroma Technology, USA) for the excitation at 470 nm and the emission of both (Krasnopeeva et al., 2019). The *in vivo* calibration curve of *EK07* cells expressing pHluorin was obtained by collapsing cytoplasmic pH using 40 mM potassium benzoate and 40 mM methylamine hydrochloride (Martinez et al., 2012). The mixture was added to MM9 + glucose media and the pH of the solution was adjusted to 5.98, 6.56, 7 or 7.5, respectively. The media at different pH were introduced into the flow-cell and imaging was carried out 5 min after (Krasnopeeva, 2018). Data was fitted to a sigmoid: $R395/475 = \frac{a_1 e^{k(pH\breve{}pH_0)} + a_2}{e^{k(pH\breve{}pH_0)} + 1}$ where a_1, a_2, k and pH_0 are fitting parameters as in (Krasnopeeva et al., 2019) (a_1 = 1.56449665, a_2 = 0.27090295, k = 1.79203546 and pH_0 = 6.55202883).

Detailed description of the model

As mentioned in the main text we treat the *E. coli's* membrane as a parallel-plate capacitor and write the V_m as Grabe et al., 2001:

$$V_m = F \cdot \frac{Q_{in}}{C} \tag{2.12}$$

where Q_{in} is the intracellular total charge (in mole) and C the membrane capacitance that depends on the membrane specific capacitance and the cell's surface area:

$$C = S_{cell} \cdot C_m \tag{2.13}$$

To calculate S_{cell} we assume the cell is a spherocylinder with 3:1 length to width ratio (determined from our microscopy images and consistent with Basan et al., 2015) and write as in Buda et al., 2016:

$$S_{cell} = \pi w_{cell} \cdot l_{cell} \tag{2.14}$$

$$V_{cell} = \pi \left(\frac{w_{cell}}{2}\right)^2 \left(l_{cell} - \frac{w_{cell}}{3}\right) \tag{2.15}$$

where l_{cell}, w_{cell} and V_{cell} are cell length, width and volume respectively.

Equation (3) in the main text lists the ionic species that contribute to Q_{in} and we assume electroneutrality in the extracellular space such that:

$$[C^+]_{out} - [A^-]_{out} + [Dye]_{out} = 0 \tag{2.16}$$

We keep the total ionic concentration in the extracellular medium, Π_e, fixed in the simulations:

$$[C^+]_{out} + [A^-]_{out} + [Dye]_{out} = \Pi_e \tag{2.17}$$

Consequently from SI Eqs. (2.16) and (2.17), the ionic composition of the medium only depends on the choice of $[Dye]_{out}$ and follows:

$$[C^+]_{out} = \frac{\Pi_e}{2} - [Dye]_{out} \tag{2.18}$$

$$[A^-]_{out} = \frac{\Pi_e}{2} \tag{2.19}$$

Separation of charges, and thus V_m, is governed by two type of reactions: leakage and active pumping, which means that the intracellular concentration of charged species we consider, changes in time as follows:

$$\frac{d[A^-]_{in}}{dt} = j_{L,A^-} \tag{2.20}$$

$$\frac{d[Dye]_{in}}{dt} = j_{L,Dye} \tag{2.21}$$

$$\frac{d[C^+]_{in}}{dt} = j_{L,C^+} - j_P \tag{2.22}$$

where equations (4) and (7) in the main text give reaction rates $j_{L,x}$, j_P, respectively. Given that chemical species Y cannot cross the membrane, Y contributes to Q_{in} in time invariant manner determined by the initial conditions only. $k_{L,x}$, k_P in the equations (4) and (7) in the main text describe the detailed mechanism by which ions leak or are pumped across the biological membrane. In the main text we mentioned we chose k_P to be a constant and $k_{L,x}$ we base on Eyring's model Garlid et al., 1989 (equation (9) of the main text).

Choosing the forward rate of pumping k_P to be a constant implies the choice of a reversible rate function that describes at least a 2-step reaction operating always in the saturating regime for all its input variables (substrate/product concentrations and voltage), *i.e.* we assume $k_P \approx N_{Pump} \cdot v_{max}$ where N_{Pump} is the number of pumps and v_{max} the maximum rate per pump. In general, k_P is expected to depend on the input variables, and one can derive the specific functional dependency if one assumes a particular mechanism of action for the pump. To do so, we would also need to specify additional parameters characteristic for a given pump, such as affinities for its substrate, dependency on V_m, etc. This is out of the scope of this work, where we model a generic pump, and we refer the reader to Keener et al., 2009 to find some examples of other rate laws for electrogenic pumps.

Eyring's model for $k_{L,x}$ is a special case of the so-called trapezoidal energy barrier model, which is a general model for describing the dynamics of ionic leakage across the membrane and is given as

$$j_{L,x} = \frac{S_{cell}}{V_{cell}} P_x \cdot b \cdot u \frac{[x]_{out} \cdot e^{u/2} - [x]_{in} \cdot e^{-u/2}}{e^{bu/2} - e^{-bu/2}} \tag{2.23}$$

where $u = -\frac{F}{RT} \cdot V_m$, P_x the so-called apparent permeability of the membrane for species x, and b is the so-called fractional width of the trapezoid. The SI Eq. (2.23) is the Eq. 7 in Garlid et al., 1989, which we multiply by $\frac{S_{cell}}{V_{cell}}$ to have the flux in units mole/volume/time rather than mole/surface/time, and which was first derived in Hall et al., 1973; Morf, 1981.

The apparent permeability is defined as: $P_x = \overline{P}_x \cdot \frac{[x]_{out}^{(interface)}}{[x]_{out}^{(bulk)}}$ where $\overline{P}_x$ is the specific permeability of the membrane for x and $[x]_{out}^{(interface)}$, $[x]_{out}^{(bulk)}$ are respectively the concentrations of x at the interface of the membrane and in the bulk (far away from the membrane). When $V_m = 0$ we expect $[x]_{out}^{(interface)} = [x]_{out}^{(bulk)}$ and the apparent and specific permeabilities to be identical. When

$V_m \neq 0$ the ionic concentrations at the membrane is different compared to the bulk, ordinarily positive at the extracellular and negative at the intracellular interface, which can influence the *apparent* membrane permeability (see section 4 of Butt et al., 2003 for more details).

In Eq. (2.23) b is parameter that characterizes the shape of the voltage drop across the membrane ($0 \leq b \leq 1$). More specifically, b characterizes $\frac{dV(z)}{dz}$ where z denote the position within the membrane. If $b = 0$, $V(z)$ abruptly changes in the middle of the lipid bilayer such that $\frac{dV(z)}{dz} = 0$ everywhere but at the geometrical middle of the membrane. This is known as the single Eyring barrier assumption and taking into the account the equation for the electrochemical potential (8) given in the main text, it reduces the SI Eq. (2.23) to:

$$j_{L,x} = \frac{S_{cell}}{V_{cell}} P_x \cdot [x]_{out} \cdot e^{-\frac{F}{2RT} \cdot z_x \cdot V_m} \cdot \left(1 - e^{\frac{\Delta G_x}{RT}}\right) \tag{2.24}$$

which is equivalent to the equations (7) and (9) in the main text. If $b = 1$, $\frac{dV(z)}{dz} =$ constant across the membrane. This was assumed by Goldman to derive the Goldman–Hodgkin–Katz (GHK) flux equation, and it it reduces the SI Eq. (2.23) to:

$$j_{L,x} = -\frac{S_{cell}}{V_{cell}} P_x \frac{z_x F}{RT} \cdot V_m \frac{[x]_{out}}{1 - e^{\frac{z_x F}{RT} V_m}} \cdot \left(1 - e^{\frac{\Delta G_x}{RT}}\right) \tag{2.25}$$

If $V_m < 0$, $\Delta G_x < 0$, $j_{L,x} > 0$ species x moves from the outside to the intracellular environment, as expected. As mentioned before, we use Eyring's assumption for our simulations and, for simplicity, we also assume that the surface partition coefficient $\frac{[x]_{out}^{(interface)}}{[x]_{out}^{(bulk)}}$ is constant, thus P_x is a constant as well.

Detailed derivation of SI equations (13) and (14) To obtain Eqs. (2.24) and (2.25) from Eq. (2.23) we first notice that $\Delta G_x / RT = -u + \ln([x]_{in}/[x]_{out})$ so that Eq. (2.23) becomes:

$$
\begin{aligned}
j_{L,x} &= \frac{S_{cell}}{V_{cell}} P_x \cdot b \cdot u \frac{[x]_{out} e^{u/2}}{e^{bu/2} - e^{-bu/2}} \left(1 - \frac{[x]_{in}}{[x]_{out}} e^{-u}\right) \\
&= \frac{S_{cell}}{V_{cell}} P_x \cdot b \cdot u \frac{[x]_{out} e^{u/2}}{e^{bu/2} - e^{-bu/2}} \left(1 - e^{\frac{\Delta G_x}{RT}}\right) \\
&= \frac{S_{cell}}{V_{cell}} P_x \cdot b \cdot u \frac{[x]_{out}}{e^{(b-1)u/2} - e^{-(b+1)u/2}} \left(1 - e^{\frac{\Delta G_x}{RT}}\right)
\end{aligned}
\tag{2.26}
$$

When $b = 1$, Eq. (2.26) is equivalent to:

$$
j_{L,x} = \frac{S_{cell}}{V_{cell}} P_x \cdot u \frac{[x]_{out}}{1 - e^{-u}} \left(1 - e^{\frac{\Delta G_x}{RT}}\right) \tag{2.27}
$$

Which is equivalent to Eq. (8) in Garlid et al., 1989.

In order to show how to obtain Eq. (2.24) from Eq. (2.23) we first introduce the hyperbolic sinus: $2 \cdot \sinh(bu/2) = e^{bu/2} - e^{-bu/2}$ such that Eq. (2.26) is written:

$$
j_{L,x} = \frac{S_{cell}}{V_{cell}} P_x \cdot b \cdot u \frac{[x]_{out} e^{u/2}}{2 \sinh(bu/2)} \left(1 - e^{\frac{\Delta G_x}{RT}}\right) \tag{2.28}
$$

We then use the fact that $\lim_{b \to 0} \left(\frac{2 \sinh(bu/2)}{b}\right) = u$ and consequently when $b \to 0$ Eq. (2.28) reduces to Erying's rate equation (2.24).

Numerical simulations

The first step of our numerical experiment consists in finding parameter sets consistent with establishing a particular value of $V_{m,0}$, that is the membrane voltage in the absence of the dye. We assume that before the addition of the dye, the cell is in steady-state $\forall x : dx/dt = 0$ and consequently:

$$
\frac{d[A^-]_{in}}{dt} = 0 \Leftrightarrow \Delta G_{L,A^-} = 0 \tag{2.29}
$$

$$
\frac{d[C^+]_{in}}{dt} = 0 \Leftrightarrow j_P = j_{L,C^+} \tag{2.30}
$$

Thus, at steady-state, A^- equilibrates according to Nernst Eq. (2) in the main text and C^+ according to Eq. (11) in the main text. Consequently, to obtain the $V_{m,0}$ we solve the following ordinary differential equation system in a 3-dimensional grid $\{\Delta G_E, [Y]_{in}, \rho\}$ (see SI Table 2.4):

$$\frac{d[A^-]_{in}}{dt} = 1 - e^{\frac{\Delta G_{A^-}}{RT}} \tag{2.31}$$

$$\frac{d[C^+]_{in}}{dt} = 1 - e^{\frac{\Delta G_{C^+}}{RT}} - \rho \cdot \left(1 - e^{\frac{\Delta G_P}{RT}}\right) \tag{2.32}$$

As shown in Fig. SI1, the influence of the dye on ΔV_m depends on how $V_{m,0}$ was generated, and we can achieve the same value of $V_{m,0}$ by different parametrizations of $\{\rho, \Delta G_E, [Y]_{in}\}$.

The second part of the numerical experiment consists of choosing a starting steady-state set of values for $\{V_{m,0}, \Delta G_E, [Y]_{in}\}$ and a given $[Dye]_{out}$. We also select the values for the permeability of the membrane to cations, anions and the dye (P_{C^+}, P_{A^-} and P_{Dye}, respectively) and keep them fixed through out the experiment (values are given in SI Table 2.3). Lastly, to obtain the dye equilibration profile we need to implement the rate-laws for pumping and leakage we discussed above, and then solve the ODE system of SI equations (2.20) to (2.22) using the stiff solver "ode15s" from MATLAB R2018b. The initial *intracellular* concentration of the dye we chose is $[Dye]_{in} = 10^{-10} mM$, and the k_P value is chosen based on the steady-state solution for $V_{m,0}$ and using Eq. (10) in the main text. Specifically, for a chosen set of $\{V_{m,0}, \Delta G_E, [Y]_{in}\}$ we find ρ that gives $V'_{m,0} \approx V_{m,0}$ and use it to set k_P from the definition of ρ in Eq. (10) in the main text:

$$k_P = \frac{S_{cell}}{V_{cell}} \cdot P_{C^+} \cdot [C^+]_{out} \cdot \rho(V'_{m,0}) \cdot e^{-\frac{FV'_{m,0}}{2RT}}. \tag{2.33}$$

Distinguishing the inner from the outer membrane

In the main text we assumed cell's cytoplasm is separated from the environment by one membrane, effectively ignoring any potential charge separation across the outer membrane of *E. coli*. While active transport of cations proceeds across the inner membrane for the case of *E. coli*, e.g. NhaA Arkin et al., 2007b

or KefB/C Papanastasiou et al., 2013, surface charge on the outer membrane can lead to Donnan potential Nelson, 2003; Stock et al., 1977, and we call this trans-outer-membrane voltage V_p. In the absence of pumps moving cations between the periplasmic and extracellular space, the ions equilibrate across the outer membrane according to Nernst equation. Therefore, for the periplasmic concentrations we can write:

$$[C^+]_p = [C^+]_{out} \cdot e^{-\frac{F}{RT}V_p} \tag{2.34}$$

$$[Dye^+]_p = [Dye^+]_{out} \cdot e^{-\frac{F}{RT}V_p} \tag{2.35}$$

$$[A^-]_p = [A^-]_{out} \cdot e^{+\frac{F}{RT}V_p} \tag{2.36}$$

We used the measured value for $V_p \sim -30$ mV (negative in the periplasm) Stock et al., 1977 to estimate $[Dye^+]_p \approx 3.2 \times [Dye^+]_{out}$. Thus, in the presence of such a V_p, the overall membrane voltage $V_m^\star$ would become $V_m^\star = V_m + V_p$ Grabe et al., 2001 and the impact of the dye on V_m is as if there was no V_p but the $[Dye_{out}]$ was ~ 3.2 times greater. Similarly, to account for the effect of the trans-outer-membrane voltage, all the concentrations $[x]_{out}$ refered to in the main text should be corrected by a factor $e^{-z_x\frac{F}{RT}V_p}$.

2.2 Conclusions

In the previous paragraphs I demonstrated that, at least in the range of conditions tested, the nernstian dye Thioflavin T does not allow the estimation of V_m in *E. coli* for several reasons. In particular, the dye is poorly permeant in growth medium in wild-type MG1655 and only accumulates in the cells' cytoplasm at appreciable concentrations if the membrane has already been damaged or if the PMF has been reduced. In the work presented we could not distinguish between the two and offered mechanistic explanations for both hypotheses: membrane damage could increase dye permeability, while a reduced PMF could impair the function of multi-drug efflux pumps. It is also possible that the two mechanisms coexist, as membrane damage can induce PMF reduction (Krasnopeeva et al., 2019). As mentioned in the introduction

paragraph, other dyes do not allow absolute V_m estimation ($DiBAC_4(3)$ and $DiSC_3(5)$ or do not normally permeate *E. coli* (TMRM) and therefore at the moment no reliable technique exists for the estimation of the V_m values of *E. coli* in physiological conditions. As discussed further in this work however, V_m could be calculated from the PMF if ΔpH is known.

As for the case of the previous use of ThT in *Bacillus*, differences in experimental setup and in the overall anatomy of the barrier that encapsulates the cytoplasm of the two organisms prevent direct comparisons. In the first instance, experiments and theory shown in this chapter demonstrate that a cationic nernstian dye that faithfully reports membrane voltage would not have any significant impact on the growth of the organism or on its membrane voltage. As described in step 1 of the workflow (Fig. 6 of the research article presented in this chapter) therefore, at the concentration used for the measurements, *B. subtilis* should grow at a rate that is indistinguishable from a ThT free environment. As per step 3, a comparison between the equilibration time of said dye concentration and of a lower one, should also report no differences. Signal intensity should then also be responsive to treatments that neutralise membrane voltage, such as the use of ionophores (step 5). Leftover dye should then been quantified and its impact on the results considered (step 6).

Chapter 3

ATP concentration estimation

3.1 Introduction

3.1.1 ATP measurements at the population level

Methods for extraction and quantification of nucleotide pools were initially developed in the 50s, when cellular contents were systematically assayed at different growth rates in balanced growth conditions (Roberts et al., 1955; Franzen et al., 1961). At the time, ATP levels were found invariant with the growth rate, a concept that would spur some controversy in the following decades for its importance in the understanding of growth regulation (Schneider et al., 2004). In the 90s, the observation of a positive dependency between ATP concentration and transcription initiation *in vitro* raised the idea that ATP concentration could have been involved in transcription regulation. RNA concentration, indeed, increases with growth rate and it was postulated that ATP might increase too, therefore enhancing transcription levels (Gaal et al., 1997). In the turn of the 70s and 80s, nucleotide extraction techniques had been perfectioned with the emergence of two main methodologies: acid and alkali extraction (Jensen et al., 1979; Little et al., 1982). Interestingly, the two techniques systematically produced contradictory results, with the acid extraction method showing invariant concentrations of ATP with the growth rate (Petersen et al., 2000) and the alkali extraction showing increasing ATP concentration (Gaal et al., 1997). To solve the contradiction, Schneider and Gourse optimized a luciferase/luciferin bioassay based on the work of (Di Tomaso et al., 2001), which confirmed that ATP levels indeed do not vary according to the growth rate, but remain instead steady (Schneider et al., 2004). Most commercial assays of ATP concentration are nowadays based on the luminescence produced by the reaction between luciferin, ATP and oxygen, catalysed by the enzyme luciferase.

The increase of RNA content in accordance with the growth rate is instead now thought to emerge from reallocation of the proteome to an increased ribosome fraction with the alarmone ppGpp taking the role of mediator between nutrient availability, rRNA transcription and ribosomal protein translation (Scott et al., 2014).

3.1.2 ATP measurements at the single cell level

While precious for their relative ease of use, population level assays can only depict population averages, which limits their usage for the study of phenomena emerging form cell-to-cell variability. With the improvement of microscopy and molecular biology techniques however, it is now possible to assay the concentration of substances in real time, *in vivo* and at the single cell level. These single cell techniques rely on the use of protein and dye sensors that change optical properties mainly in response to changes in the concentration of the molecule sensed. Examples of such probes are membrane voltage sensors (Felle et al., 1980), calcium sensors (Russell, 2011), potassium sensors (Rimmele et al., 2014) and pH sensors (Han et al., 2010). The first steps towards the production of a single cell ATP sensor were moved by bringing the luciferase assay into single cells, initially via direct protein injection (Bowers et al., 1992; Koop et al., 1993) and later via genetically encoded expression (Kennedy et al., 1999). Luciferase was also conjugated to nanotubes, which can in turn be taken up by the cells (Kim et al., 2010). In all of these cases, the assays rely on the entrance of the substrate luciferin into the cells. In bacteria and particularly in gram negative ones, permeability of substances from the extracellular space is significantly lower than in mammalian cells (Vaara, 1992). Therefore, the research of a strategy for ATP sensing veered towards strategies that could be fully genetically encoded. Because this work focuses on *E. coli*, in the following lines I will review techniques that were either developed in bacteria or that could potentially be applied to single cell, time series, *in vivo* measurements in bacteria. General reviews of techniques for ATP estimation are available (Rajendran et al., 2016; Dong et al., 2016). The first report of a single cell technique that could potentially be applied to bacteria at the single cell level is relatively recent and concerns a fluorescent protein sensor capable of binding both ATP and ADP in a competitive fashion, therefore reporting ATP:ADP ratio: Perceval. The sensor is ratiometric and is based on a

circularly permuted fluorescent protein, cpmVenus, fused to an ATP-sensing protein, GlnK1 (Berg et al., 2009). A variant of the sensor exists, PercevalHR, with an extended sensitivity range and fluorescence spectrum response produced via random mutagenesis (Fig. 3.1) (Tantama et al., 2013). In this work, while screening for a possible way of assaying the cellular energetic state in the form of ATP, the expression of both Perceval and PercevalHR sensors was attempted in *E. coli* from a plasmid, downstream a constitutive promoter. At the best of my knowledge, the successful use of Perceval or PercevalHR for the estimation of the ATP:ADP ratio in *E. coli* is only reported in one work, in stationary phase cells after 16 hours induction (Wilmaerts et al., 2018). In the

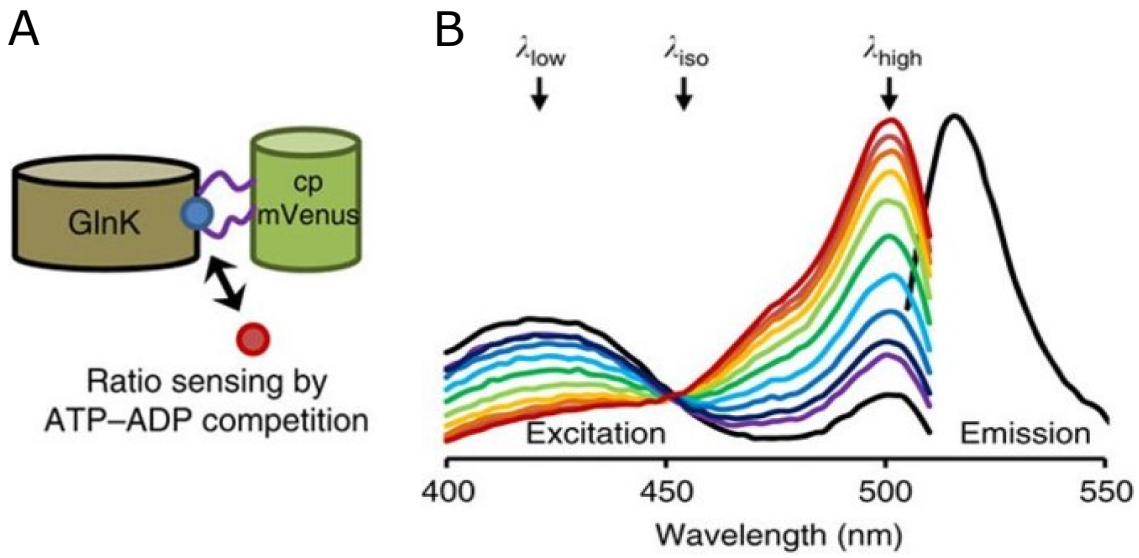

FIGURE 3.1: Schematic structure of the Perceval-based sensors and fluorescent spectra of PercevalHR from (Tantama et al., 2013). In right: colors from blue to red show increasing ATP to ADP ratio.

same year, Imamura et al. developed a FRET based sensor for the quantification of ATP concentration that has limited affinity for ADP: ATeam. ATeam has a sensing region made up of the subunit of the F_1F_o ATPase from *B. subtilis* which is then coordinated to a FRET couple that is a derivative of CFP and YFP. The authors produced variants with different sensitivities by replacing the subunit of *B. subtilis* with the one of *B. PS3*, that has higher affinity to ATP, and by exchanging amino acids between the two proteins (Fig. 3.2 (Imamura et al., 2009). As the same authors highlight in a subsequent work Yaginuma

et al., 2014, the signal from these FRET sensors is susceptible to changes in growth rate, because of the different, growth rate-dependent, maturation and degradation times of the two fluorophores.

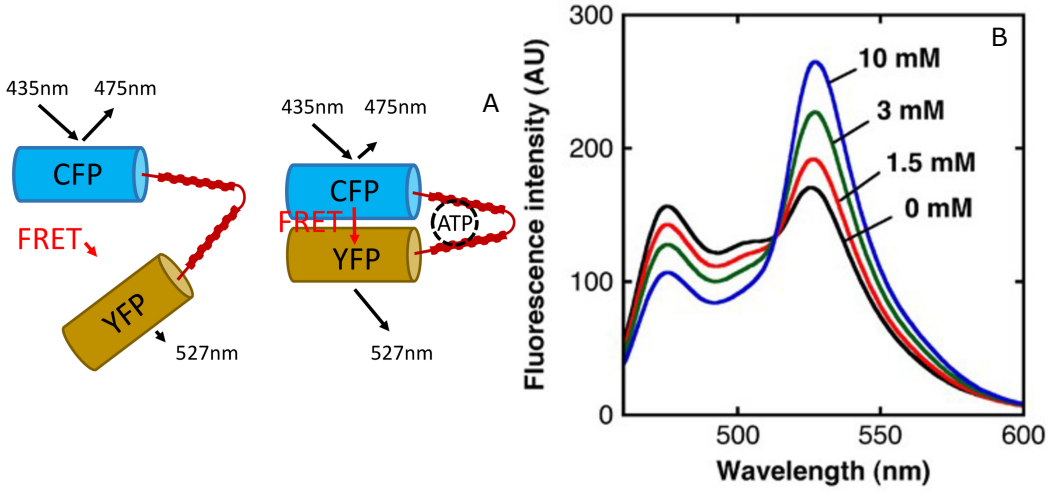

FIGURE 3.2: ATeam sensors structure and emission spectra in the presence and absence of ATP, adapted from (Imamura et al., 2009). Different arrow lengths symbolize different intensities. The ratio between the two emission peaks depends on ATP concentration.

Based on the same ATP-sensing protein, the ϵ subunit from the F_1F_o ATPase, the authors developed an ATP sensor with a single fluorescent protein: QUEEN. The probe relies on a circularly permuted EGFP, which is an EGFP in which the folded structure is maintained, but the N and C termini are positioned in a different, strategical location. In QUEEN, the permuted termini are linked to two portions of the subunit from one or more bacterial species (Fig. 3.11). Like in ATeam, ATP sensing leads to a change in conformation which in turn alters the optical properties of the EGFP (Yaginuma et al., 2014). Unfortunately, the sensor, particularly in its form that senses ATP in the physiological range, was very dim. In an attempt to improve the low signal problems from QUEEN, the same lab produced a variant of the ATeam sensor that is based on BRET (FRET but with bioluminescence), BTeam (Yoshida et al., 2016). Like other luciferase/luciferin probes, the sensor needs an external supplement of luciferin and is therefore hard to deploy in bacteria. Finally, very recently, a version of QUEEN that has been optimised for measurements in mammalian cells has been produced (Lobas et al., 2019).

3.2 Materials and methods

3.2.1 Strains

Strain	Genotype
MG1655-Perceval	pWR20-Perceval
MG1655-PercevalHR	pWR20-PercevalHR
MG1655-QUEEN7μ	pWR20-QUEEN7μ
MG1655-QUEEN2mM	pWR20-QUEEN2mM
MG1655-QUEEN7μ*	pWR20-QUEEN7μ*
MG1655-QUEEN2mM*	pWR20-QUEEN2mM*
EK01-QUEEN7μ*	ΔFliC, pWR20-QUEEN7μ*

TABLE 3.1: Strains used in the experimental work presented in this chapter. The EK01 strain was obtained from (Krasnopeeva et al., 2019) and transformed with the pWR20-QUEEN7μ* plasmid as indicated. It carries the FliC^{STICKY} mutation necessary for BFM speed assays (Krasnopeeva et al., 2019). In this chapter it was used in Fig. 3.17 and 3.16.

3.2.2 Culture conditions

For the production of cell lysates, cells from frozen stocks were inoculated at a 1:4000 dilution in LB (5 g/L Yeast extract, 10 g/L Tryptone and 10 g/L NaCl) (Fig. 3.13) or RDM (Neidhardt et al., 1974) (Fig. 3.14, 3.15, 3.18) and grown at 37°C with shaking at 200 rpm. Frozen stocks were kept at -80°C and prepared from stationary phase LB cultures grown overnight and diluted into 50% w/v glycerol with a 3:2 ratio (final glycerol concentration: 20% w/v). For intensity comparisons, single colonies from agar plates were first inoculated in LB in flasks and grown for 3-4 hours at 37°C with 200 rpm shaking (seed culture). Cells from the seed culture were then inoculated in RDM at a 1:10^7 dilution at 37°C with 200 rpm shaking such that they could reach steady state (Fig. 3.12). To assay illumination damage on the cells and compare it to previous work, cells were grown in LB from a frozen stock at 1:160 dilution to OD 2 as in (Krasnopeeva et al., 2019) and transferred to MM9 medium (7 g/L Na2HPO4, 3 g/L NaH2PO4, 0.5 g/L NaCl, 1 g/L NH4Cl, 0.3% w/v Glucose, 0.1 mM CaCl2, 1mM KCl, 2mM MgSO4) (Fig. 3.16). To assay whether the values reported by QUEEN7μ* depended on ATP concentration *in vivo*, cells were grown in M63 Glucose (13.6 g/L KH2PO4, 0.5 mg/L FeSO4·7H2O, 0.5 g/L MgSO4·7H2O,

1.27 mg/L Thiamine, 2.64 g/L (NH4)2SO4 and 0.5% w/v Glucose) to steady state.

3.2.3 Plasmids

Plasmid	Fragment	Template	Primers
pWR20-Perceval	pWR20 backbone	pWR20	5′ AAAGCGGCCGCGGTGATTGATTGAGCAAG 3′
			5′ AAACCTAGGATGTATATCTCCTTAACTAGGT 3′
	Perceval	Perceval	5′ TTAGCGGCCGCCCACAACGGTTTCCCTCTAG 3′
			5′ TATCCTAGGTCACAGTGCTTCCTTGCCC 3′
pWR20-PercevalHR	pWR20 backbone	pWR20	5′ AAAGCGGCCGCGGTGATTGATTGAGCAAG 3′
			5′ AAACCTAGGATGTATATCTCCTTAACTAGGT 3′
	PercevalHR	PercevalHR	5′ TTAGCGGCCGCCCACAACGGTTTCCCTCTAG 3′
			5′ TATCCTAGGTCACAGTGCTTCCTTGCCC 3′
pWR20-Q2*	pWR20 backbone	pWR20	5′ AAAGCGGCCGCGGTGATTGATTGAGCAAG 3′
			5′ AAACCTAGGATGTATATCTCCTTAACTAGGT 3′
	Q2*	Q2mM	5′ ATACCTAGGATGAAAACTGTGAAAGTGAAT 3′
			5′ AATGCGGCCGCTCACTTCATTTCCGCAAC 3′
pWR20-Q7*	pWR20 backbone	pWR20	5′ AAAGCGGCCGCGGTGATTGATTGAGCAAG 3′
			5′ AAACCTAGGATGTATATCTCCTTAACTAGGT 3′
	Q7*	Q7μM	5′ ATACCTAGGATGAAAACGATCCACGTGA 3′
			5′ AATGCGGCCGCTCACTTCATTTCCGCAAC 3′
pWR20-Q2	pWR20 backbone	pWR20	5′ AAAGCGGCCGCGGTGATTGATTGAGCAAG 3′
			5′ AAACCTAGGATGTATATCTCCTTAACTAGGT 3′
	Q2	Q2mM	5′ ATACCTAGGATGCATCACCACCATCATCACAAAA CTGTGAAAGTGAATAT 3′
			5′ AATGCGGCCGCTCACTTCATTTCCGCAAC 3′
pWR20-Q7	pWR20 backbone	pWR20	5′ AAAGCGGCCGCGGTGATTGATTGAGCAAG 3′
			5′ AAACCTAGGATGTATATCTCCTTAACTAGGT 3′
	Q7	Q7μM	5′ ATACCTAGGATGCATCACCACCATCATCAC AAAACGATCCACGTGAGC 3′
			5′ AATGCGGCCGCTCACTTCATTTCCGCAAC 3′

TABLE 3.2: Plasmids constructed by restriction-ligation for the experiments shown in this chapter. Fragments and primers are indicated. The pWR20 backbone was obtained from (Pilizota et al., 2012) and carries the pBR322 origin of replication and a kanamycin marker. Perceval and PercevalHR templates were obtained from (Berg et al., 2009) and (Tantama et al., 2013) while the QUEEN sensors from (Yaginuma et al., 2014).

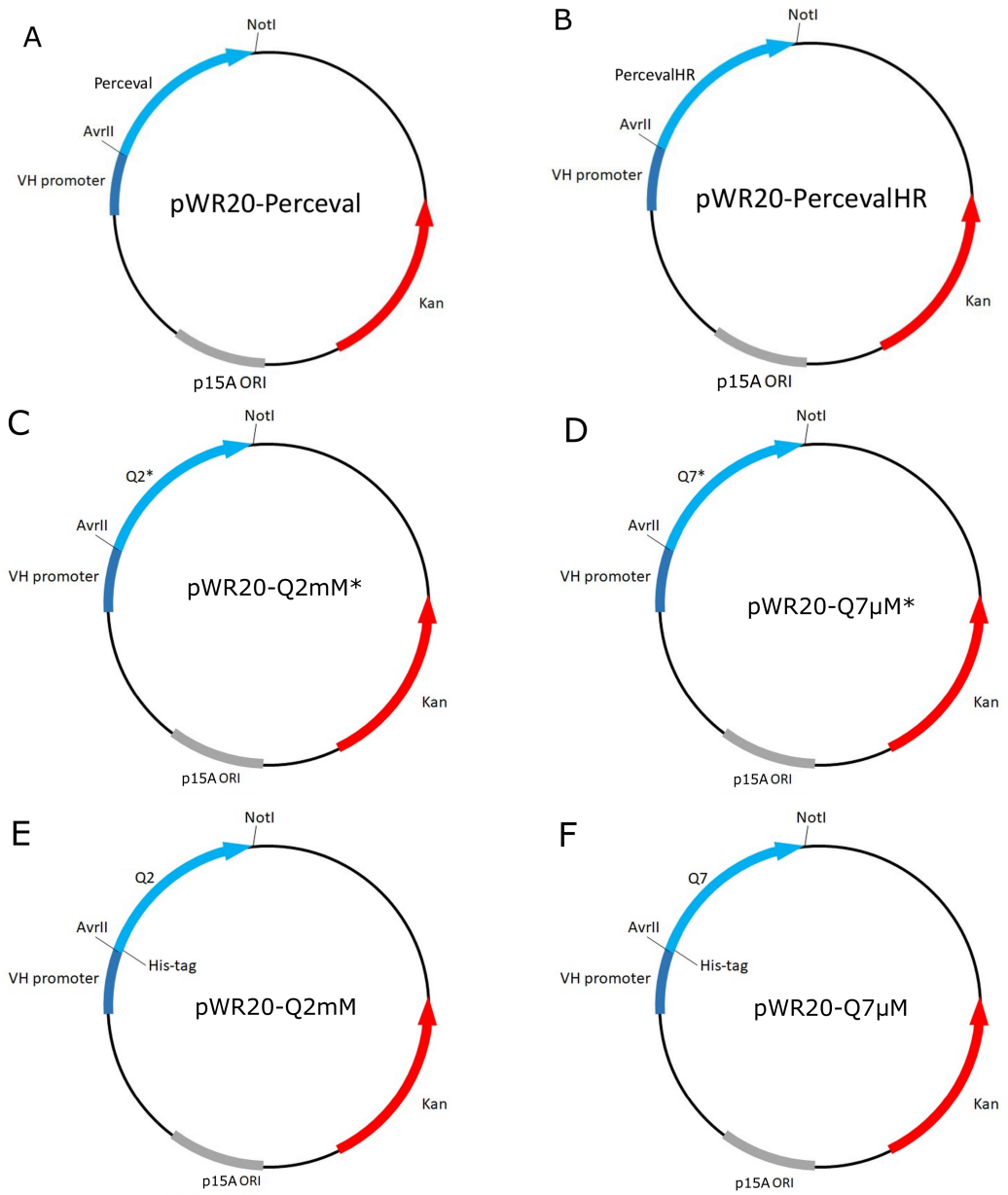

FIGURE 3.3: Maps of the plasmids produced for the constitutive expression of ATP sensors. a) Perceval, b) PercevalHR, c) QUEEN 2mM*, d) QUEEN 7μM*, e) QUEEN 2mM and f) QUEEN 7μM.

3.2.4 Fluorescence spectra

Fluorescence spectra were obtained with a SPEX Fluoromax 3 spectrometer. Excitation was scanned from 370 to 500nm at 513nm emission with a slit size of 3nm. The temperature of the sample holder was controlled via a circulating water bath, readings were taken after letting the temperature of the sample reach equilibrium with that of the sample holder for at least 5 minutes.

3.2.5 Fluorescence microscopy and microscope customization

The Pilizota lab uses a custom made microscope capable of brightfield and epifluorescence imaging and optical trapping. A detailed description of its setup was given elsewhere (Rosko, 2017; Krasnopeeva, 2018) and it is reported in Fig. 3.5. The light source for brightfield is a white LED (Luxeon Star, USA), while for epifluorescence, illumination is provided by a 395nm LED and a neutral white LED that together cover the spectrum summarised in Fig. 3.4. Wild-type MG1655 *E. coli*'s autofluorescence excitation spectrum has two peaks in the 370-500nm range with 513nm emission: 370nm and 470nm (Fig. 3.14). The QUEEN sensor has two peaks at 400 and 490nm (Fig. 3.14A, 3.9A). While at 400nm excitation the microscope setup is well fit for imaging, at 490nm only a portion of the peak can be excited by the ET470/40x filter (Chroma technology, USA) and the neutral white LED is relatively less intense (Fig. 3.4). As a result, the setup was prone to picking up significant amounts of signal from *E. coli*'s autofluorescence. To improve the signal-to-noise ratio of the imaged QUEEN, I implemented a 488nm laser as a light source for excitation, as this is at the center of the second excitation peak of QUEEN, and does not need an excitation filter (Fig. 3.14A, 3.9A). To set it up, the beam of the laser was first enlarged with a telescope made up of a lens of 2cm focal length and another of 50cm. The collimated beam was then focused on the back focal plane of the objective by a 17.5cm focal length lens, as showed in Fig. 3.5. To enable simultaneous illumination at 488nm and in the UV range, a shortpass dichroic mirror (Chroma, UK) (D1 in Fig. 3.5 and 3.6B and C) that only reflects light in a narrow region of the spectrum around 488nm was mounted at the intersection of the optical paths for illumination. The mirror was mounted on a flipper mount, such that users who needed the neutral white LED for illumination around 488nm could still have the choice to use it. Imaging where the 488nm laser was involved (Fig. 3.12, 3.17, 3.15,3.18,3.16) was carried out

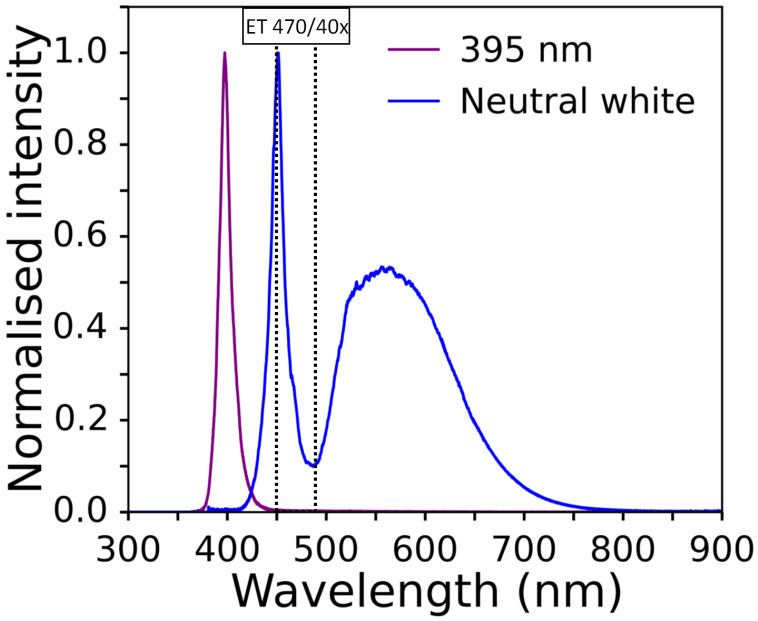

FIGURE 3.4: Spectra of the LEDs used in our custom made setup for epi-fluorescent excitation. The portion of the plot between the two broken lines indicates the region in which the ET470/40x filter is transmissive. At around 500nm the intensity of the neutral white LED is scarce making it sub-optimal for imaging of the QUEEN sensor. The image was adapted from (Krasnopeeva, 2018)

with 50ms exposure time and 50 Andor camera gain, only using the emission filter ET525/40m (Chroma technology, USA). For the experiments with cell lysates where the white LED was used as a source of illumination (Fig. 3.13), exposure time and camera gain were 0.1s and 300, respectively, with the filters ET470/40x (Chroma technology, USA) and ET525/40m for excitation and emission.

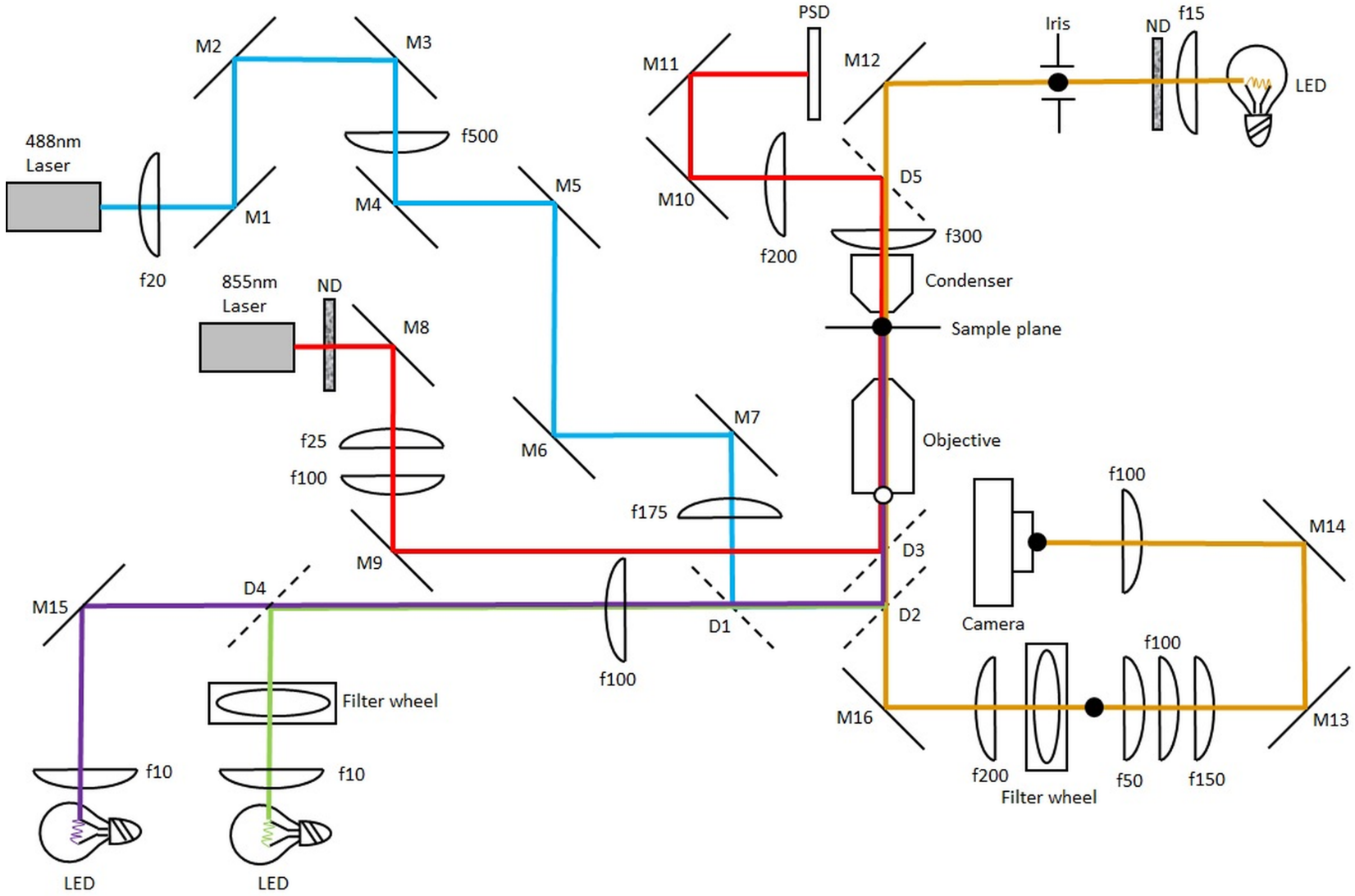

FIGURE 3.5: Scheme of the lab's custom microscope. Yellow and red lines show the optical paths of brightfield and optical trap described in (Rosko, 2017). Purple and green lines show the optical paths for LED-based epifluorescence (Krasnopeeva, 2018). In blue is presented the optical path of the 488nm laser used for epifluorescent illumination of the QUEEN sensor. M and f stand for mirror and lens.

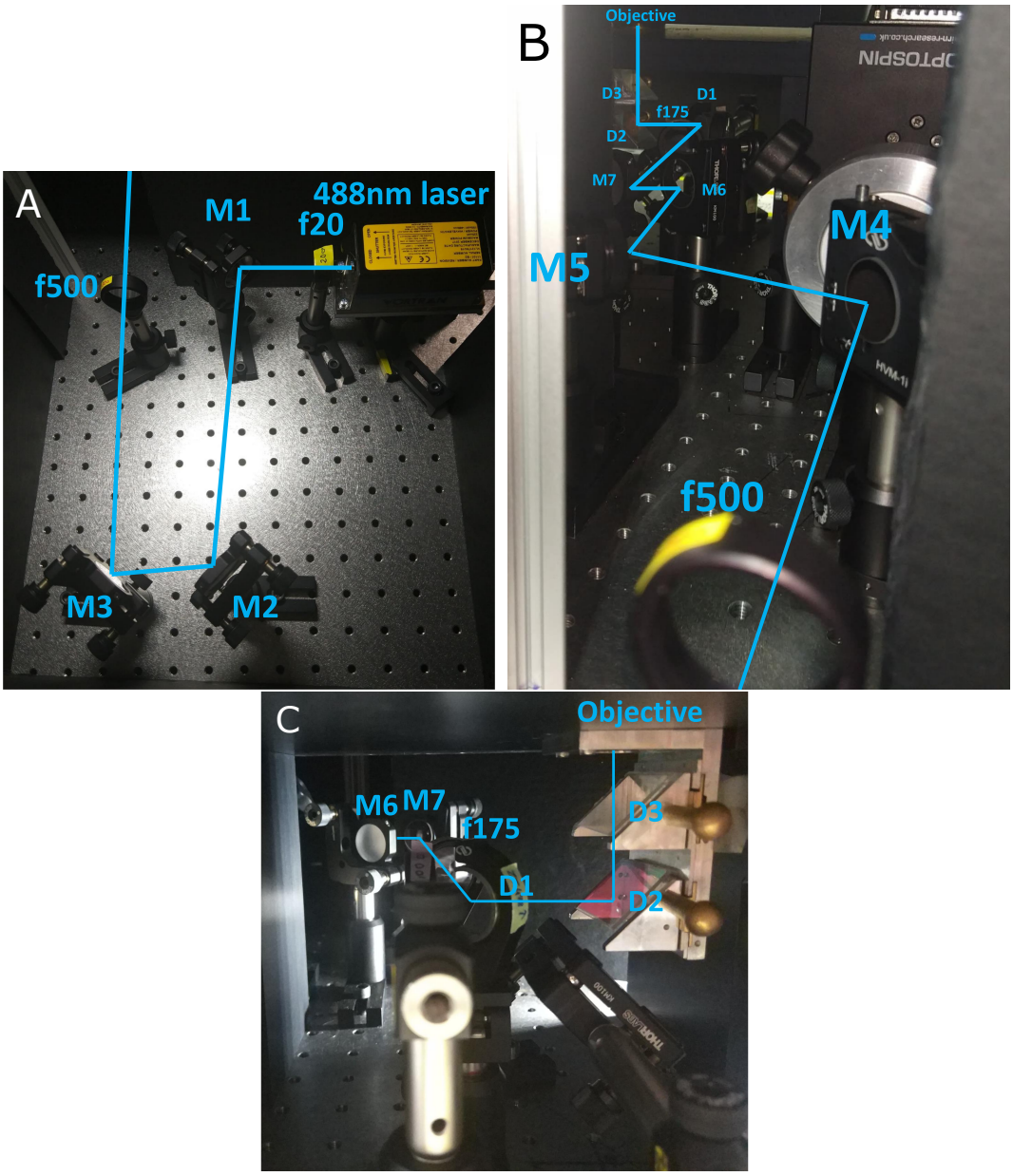

FIGURE 3.6: Images of the additional parts installed in the lab's microscope for the implementation of a 488nm laser as an illumination source for epifluorescence. M and D indicate mirrors and dichroic mirrors, respectively, numbered sequentially starting from the closest to the light source. f20, f500 and f175 indicate lenses and focal lengths in mm.

3.2.6 Sensor calibration

Cells were harvested via centrifugation at 9000 rpm (11000G) at 4°C for 30 minutes. The supernatant was discarded and cells resuspended in ice cold QUEEN buffer (50mM HEPES, 200mM KCl, 1mM MgCl2, 0.05% Triton X-100, protease inhibitor cocktail (Sigma, GB), pH adjusted to 7.7)(Yaginuma et al., 2014). 100ug/ml of lysozyme was added to the cell suspension and incubated for 15 minutes at room temperature (21°C). Cells were disrupted with a Sopniprep 150 sonicator (MSE (UK)) with 4 cycles of 30' on and 30' off, making sure that no foam was produced. During sonication the tube containing the sample was kept in ice cold water to limit protein damage. The lysates were then filtered with a 0.22 μm filter size to remove intact cells and large debris. Solutions of Mg-ATP (Sigma, UK) and QUEEN lysate were prepared maintaining a constant ratio between the two. Samples for imaging were prepared in tunnel slides (Fig. 3.7) by flushing 10 μl 1% Poly-L-Lysine (Sigma,UK), 100 μl QUEEN buffer wash, 10 μl of a 1:1 1μm polystyrene bead solution (Polysciences, USA), 100 μl QUEEN buffer wash, 10 μl of QUEEN lysate and ATP solution, the slides were then sealed (Biotium, US). Three distant fields of view were imaged with epifluorescence microscopy from each slide, the imaging plane was chosen focusing on the polystyrene beads.

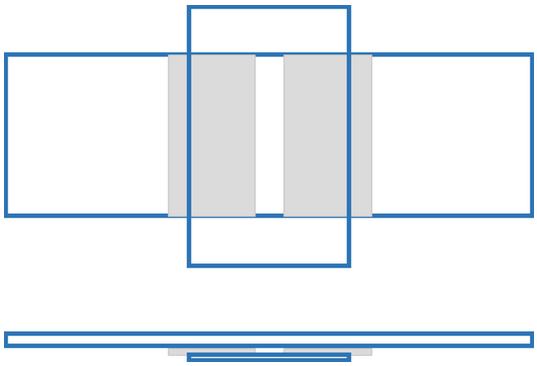

FIGURE 3.7: Top and side view of the tunnel slide used for cell lysates calibration. A vertical coverslip is attached to a horizontal microscope slide using two pieces of double-sided sticky tape indicated in grey. The distance between the two pieces of tape is approximatively 0.7mm.

3.2.7 Light damage estimation

To enable direct comparison with previous results, the estimation of light damage was carried out as in (Krasnopeeva et al., 2019). Briefly, cells for BFM speed measurements were prepared by growing them in LB at 37°C with shaking at 220rpm an *E. coli* EK01 culture carrying the QUEEN 7μ plasmid to OD 2. Aliquots of the culture were taken and the flagella were sheared by passing the cells through two syringes with narrow-gauge needles (26 gauge) connected by plastic tubing. Sheared cells were then spun down at 8000G for 2 minutes and the pellet resuspended in MM9. Flow cells (Fig. 2.SI2) were flushed with Poly-L-Lysine and immediately washed with roughly 10 flow chamber volumes (2.5ml) of water and 1 ml of MM9. Cells were then loaded in the slide and incubated for 10 minutes. Cells that did not stick to the surfaces of the chamber were washed out with 1 ml of MM9 and a suspension of beads with diameter 0.5μm (Polysciences, US) was flown in the chamber and incubated for further 10 minutes. Beads in excess were washed away with 1 ml of MM9. The experiments were carried out at room temperature (21°C) with a constant flow of 100μl/min of MM9 medium. Cultures were subjected to different light dosages by changing illumination frequency.

3.2.8 Data analysis

Spectroscopy

Signal intensity was automatically normalised by the intensity of the light source across the spectrum examined during data acquisition. The results obtained from the experiments, which were carried out in triplicate, were averaged and the standard deviation calculated. The spectra obtained were normalised by their value at 435nm excitation, which is the isosbestic point of the QUEEN spectrum, insensitive to ATP concentration.

Image analysis

The image analysis was carried out with a custom-written python script. For the analysis of the cytoplasmic lysates, every set of experiments was initially assayed for uniformity of the intensity values in the field of view in ImageJ. This was done to make sure that artifacts originating from large cellular debris that made it through the filtration step were not included in the analysis. An

area, normally above 50% of the field of view, in which the profile of the values was constant, was individuated and the values of all the pixels within such region averaged. All images, both from lysates and from live cells were initially inspected for unevenness of the field of view, which can sometimes arise if the sample or the microscope stage are slightly tilted. If a tilt was observed, portions of the images that were out of focus were cut off. To individuate the cells, objects with high grey values were automatically identified by applying a global threshold via the Otsu's method (Otsu, 1979). The resulting regions were then filtered for size and aspect ratio, using parameters that had been optimised for the individuation of cells grown in the particular conditions of the experiment, lying flat on the flow chamber surface. Total cells' intensity values were obtained by averaging pixels within the region thus selected.

Bacterial flagellar motor assay

Raw traces of the position of the bead attached to the filament stub were analyzed by a moving-window discrete Fourier transform as in (Rosko et al., 2017). From the obtained motor speed traces DC frequency (50 Hz) was removed, speeds lower then 5 Hz ignored, and subsequently a median filter (window size 31) was applied (Krasnopeeva et al., 2019). It should also be noted that I used a wild type strain for which the BFM can change rotational direction, which appears as a negative speed after application of the moving-window Fourier transform. However, for the purpose of PMF measurements these short intervals can be disregarded, and I only show the speed values above 0 Hz.

3.3 Results

3.3.1 Expression of Perceval and PercevalHR is not uniform in *E. coli*

The ratio between ATP and ADP is an interesting parameter for cell physiology, because it dictates the energetic yield of ATP hydrolysis. Quick changes in ATP to ADP ratios are also potentially representative of shifts in cellular energetic contents, given that ADP is the product of ATP hydrolysis and therefore of energy expenditure. Thus I tested whether Perceval and PercevalHR sensors (Berg et al., 2009; Tantama et al., 2013) could be expressed constitutively in *E. coli* with a sufficient amount of signal. The sensors were transferred downstream the strong constitutive promoter of a cytochrome oxidase from *Vibrio Harveyi* on pWR20 (Pilizota et al., 2012) and cells were imaged. While the signal from fluorescent cells was significantly higher than the background, the majority of cells were not bright (Fig. 3.8), which suggests that, at least at this level of expression and in these conditions, the sensor potentially causes a certain level of toxicity (Rosano et al., 2014).

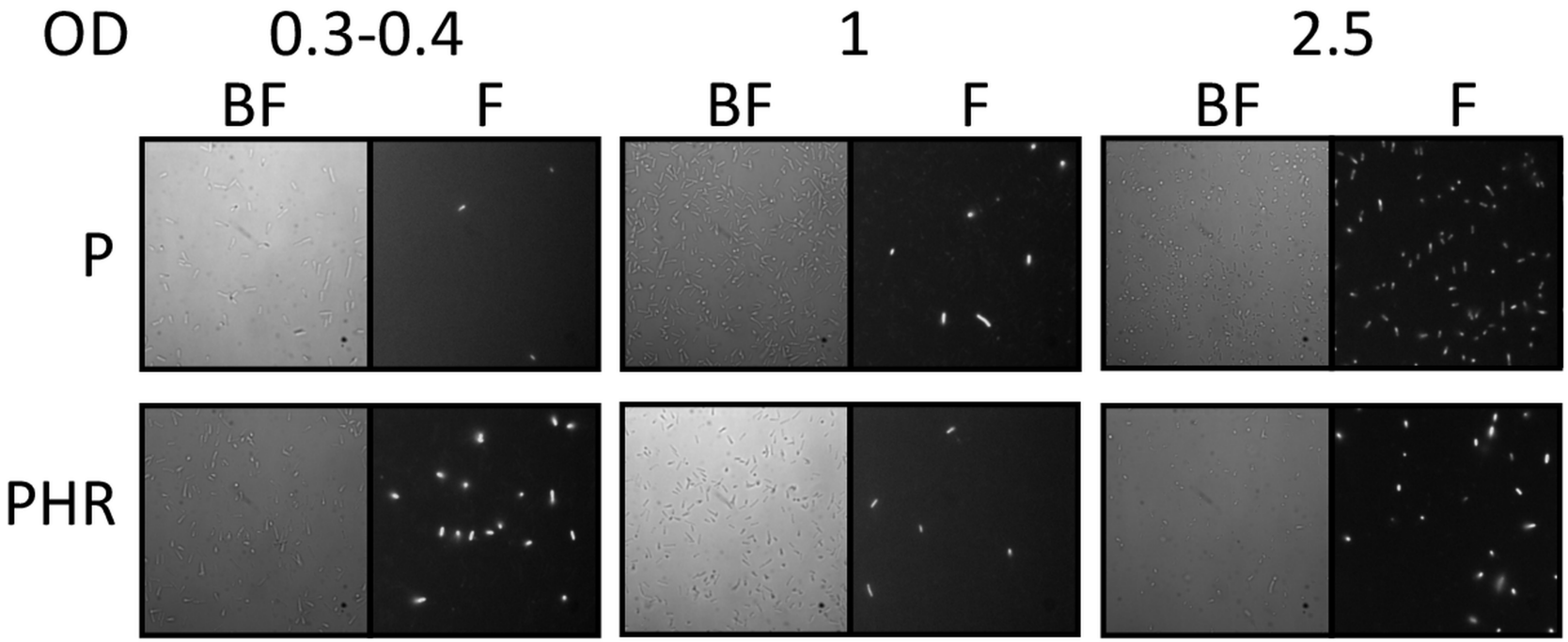

FIGURE 3.8: Expression of the Perceval (P) and PercevalHR (PHR) sensors from the pWR20 plasmid is not uniform across the cell population and across different growth stages. Cells were imaged in mid exponential phase (OD 0.3-0.4), late exponential phase (OD 1) and stationary phase (OD 2.5). Bright field (BF) and fluorescence (F) images are given.

3.3.2 The effects of a rational sequence modification on the QUEEN sensors: higher fluorescence signal.

The QUEEN sensor is another promising option for assaying ATP levels. Two ATP-sensing versions exist, named QUEEN 7μ and 2m because their sensitivity ranges are centered at 7μM and 2mM, respectively. The sensitivity range of the first roughly spans two orders of magnitude (range: 0.001 to 0.1 mM), while the second just one (range: 1 to 10mM). Because in physiological conditions, growing *E. coli* is thought to have an ATP concentration in the millimolar range (Yaginuma et al., 2014; Schneider et al., 2004), only the second can show ATP variations while the first is thought to be always saturated (Fig. 3.9B). However, like Perceval and PercevalHR, the sensor had not been expressed

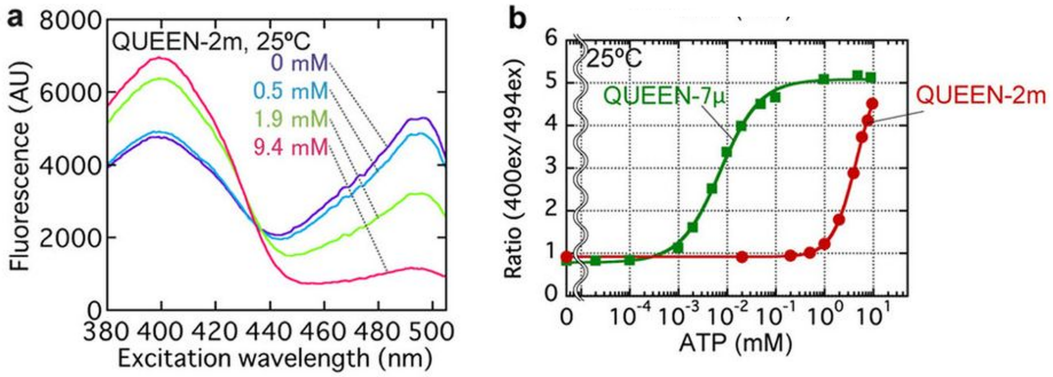

FIGURE 3.9: The QUEEN ATP sensor developed by (Yaginuma et al., 2014). a) Excitation spectra of QUEEN 2mM at different ATP concentrations. b) *In vitro* ATP calibration of the QUEEN7μ (green) and QUEEN2m (red) sensors. Adapted from (Yaginuma et al., 2014).

constitutively in *E. coli* before. To verify whether the sensor could be easily used for physiological measurements in E. coli, I transferred the QUEEN sensors downstream the strong constitutive promoter of pWR20 like I did for the Percevals. This time, signal was uniform among all the cells (Fig. 3.10). Particularly for the sensor that was named QUEEN2mM by its inventors, the signal intensity was however very low, in accordance with the previously published 2 seconds exposure time necessary for its imaging. In (Yaginuma et al., 2014), the calibration of QUEEN sensors for different ATP concentrations is performed on purified sensors that have a polyhistidine sequence (His-tag) at the N-terminal. The purification technique is based on the tendency that

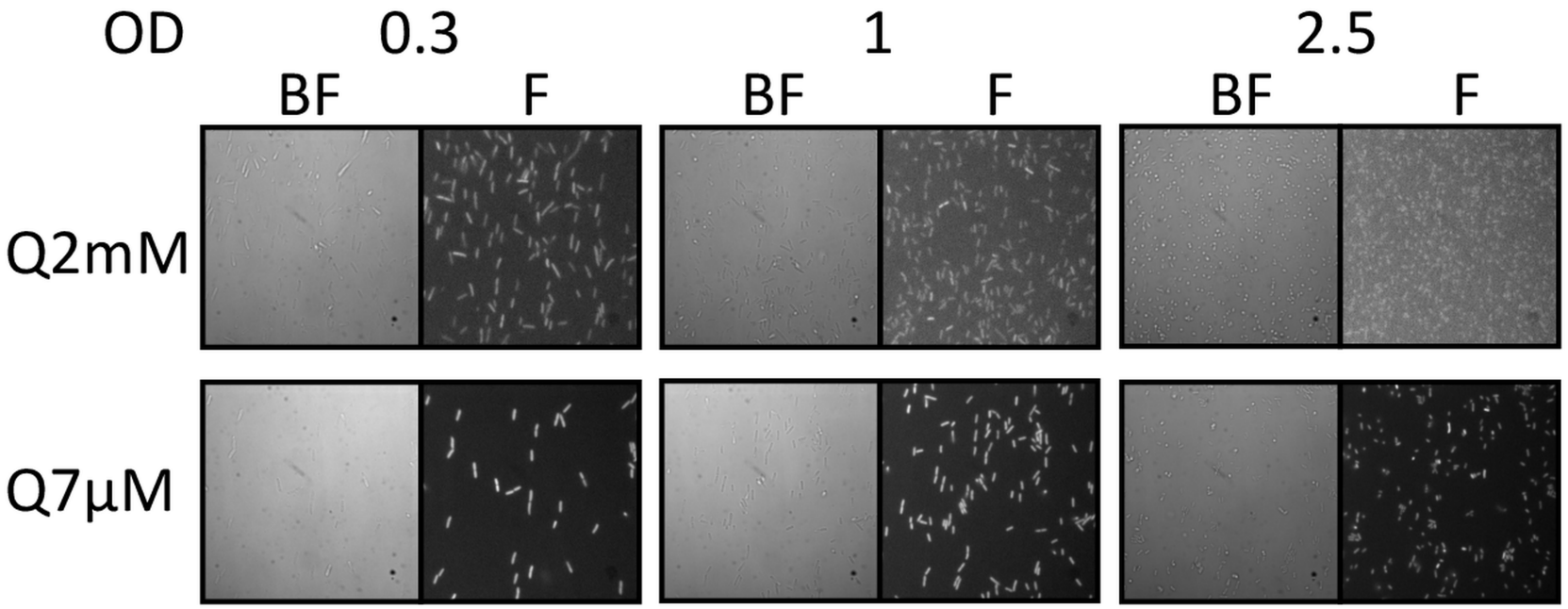

FIGURE 3.10: Expression of the QUEEN7μ and QUEEN2m sensors from the pWR20 plasmid is uniform across the cell population. Cells were grown from a frozen stock and imaged in mid exponential phase (OD 0.3), late exponential phase (OD 1) and stationary phase (OD 2.5). Bright field (BF) and fluorescence (F) images are given.

histidine has to bind metal ions. Taking advantage of this property, recombinant proteins carrying a repeated sequence of the amino acid can be retained onto columns in which metal ions have been immobilized (Immobilized metal ion affinity chromatography) (Yip et al., 1992). The His-tag at the N-terminal, however, is in close proximity with the ATP-sensing region. In the cytoplasm, ATP is active when complexed to Magnesium (Berg et al., 2002b). Therefore the His-tag could potentially affect the behavior of QUEEN either directly, by influencing the conformation of the ATP binding region, or indirectly by interacting with the Magnesium associated with ATP. The authors however give no clear mention on whether the tag is maintained for *in vivo* measurements. Considered the potential effects that the tag might have on the behavior of the sensor, purification and ATP calibration should be performed with the same protein. To verify whether the presence of the His-tag was affecting the behavior of the sensor, I produced a second set of plasmids expressing an His-tag-free version of the QUEEN protein 3.11. I will now on refer to this variant as QUEEN* or QUEEN star.

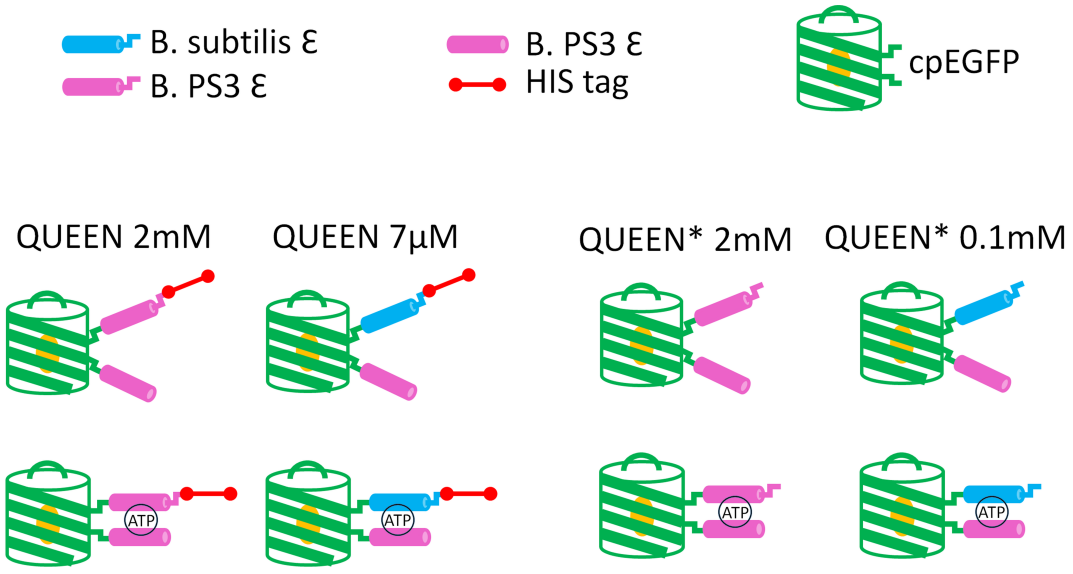

FIGURE 3.11: Cartoon schematic of the QUEEN sensors produced by (Yaginuma et al., 2014) and of the sensors I produced by removing the histidine tag. The structures are shown with and without ATP to highlight the ATP binding site and the conformational change induced by the binding of the molecule.

The first property I compared between the QUEEN and the QUEEN* sensors was signal intensity. As seen in Fig. 3.10, structural changes that do not concern the GFP can still have an effect on signal intensity. Interestingly, I

found that the elimination of the His-tag bears significant improvements to the signal intensity of the QUEEN 7μM (Fig. 3.12).

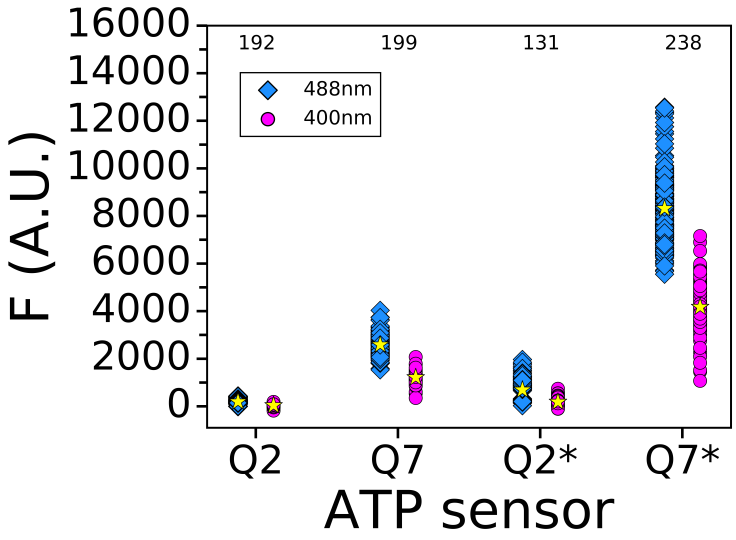

FIGURE 3.12: The removal of the histidine tag induces a significant change in the fluorescence of the QUEEN7μ sensor. Sensors without the tag are labelled by an *. All the cells are grown and imaged in the same conditions. Each data point is a single cell and values are given in blue for the 488nm excitation wavelength and in purple for the 400nm excitation wavelength. Yellow stars indicate the mean values. Cell numbers are given below the top x axis. Statistical significance of the difference in signal between the QUEENs and QUEENs* was assayed with a Welch's t-test with p-values $< 10^{-20}$.

3.3.3 The effects of a rational sequence modification on the QUEEN sensors: the sensitivity range.

I then tested whether the tag was altering the sensitivity range of the protein. To calibrate the fluorescence of QUEEN* against Mg-ATP concentration maintaining the protein unmodified and in its native conformation I developed an assay that relies on cell lysates and fluorescence microscopy. The methodology is detailed in *Materials and Methods* and involves cell resuspension in a buffer that mimics cytoplasmic conditions (Yaginuma et al., 2014) and lysis first via lysozyme treatment and then via sonication. From growth to microscope slide preparation, cells and lysates are kept on ice, with a brief transition into room temperature during lysozyme treatment, to minimize protein damage. QUEEN2mM* did not show any significant change from the published sensitivity range (Fig. 3.13). In the case of QUEEN 7μ* instead, the removal of the his-tag seemed to cause a slight shift of the sensitivity range towards the higher ATP concentrations (range: 0.01 to 1mM). However, as shown by the size of the error bars in Fig. 3.13A, B and C, the ratios produced by experiments carried out on different days suffered of poor reproducibility, mostly because of the low difference in fluorescence signal between lysates obtained from wild-type strains and lysates obtained from strains expressing the sensors (Fig. 3.12). Because autofluorescence contributed a large portion of the final fluorescence, changes in lysis efficiency or in cell number during sample handling caused significant variations. To improve the signal-to-noise ratio, I customized our lab's microscope by implementing a 488nm laser as a light source for epifluorescence. This had the advantage of illuminating the QUEEN sensors at one of their excitation peaks, thereby reducing autofluorescence. As explained in further detail in the *Materials and methods* section, the laser at 488nm also replaces our neutral white LED in a portion of its spectrum in which it is not particularly powerful (Fig. 3.4). When this new setup was used to image cells expressing the QUEEN7μM* sensor, it was possible to reduce the exposure time from 2 seconds to 50 ms, which had the potential to enable the use of the sensor for time series measurements.

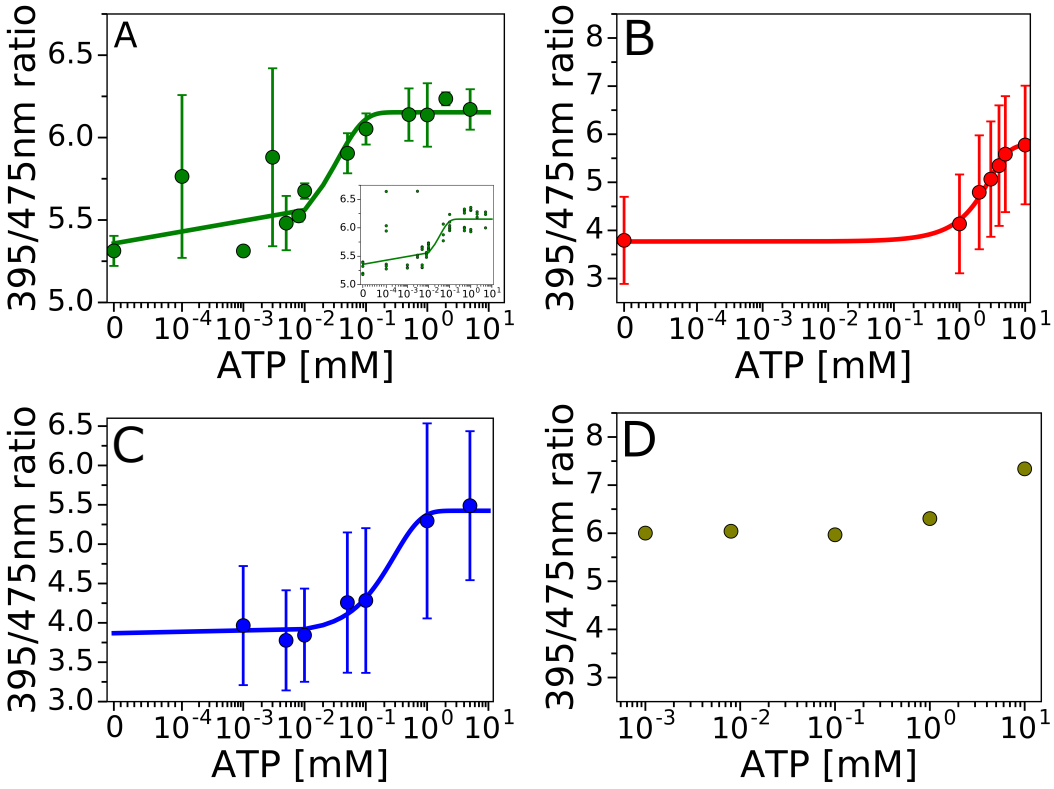

FIGURE 3.13: Calibration of lysates from cells expressing the QUEEN7μ, QUEEN7μ* and QUEEN2m* sensors with LED illumination. a) Calibration of the QUEEN7μ lysates at different ATP concentrations. The error bars show the standard deviation. For each experiment, fluorescence was read from three distant fields of view. In the inset, the single fields of view are shown, highlighting that the two large error bars for the ATP concentrations of 0.0001 and 0.003mM are the result of a few outliers. No obvious source of artifactual contribution to the signal was however noticed during image collection or image analysis and the data points were thus included. b) Calibration of the QUEEN2mM* lysates at different ATP concentrations. c) Calibration of the QUEEN7μ* lysates at different ATP concentrations. d) Autofluorescence of the solutions containing cytoplasmic lysate from cells that do not express QUEEN and ATP increases for ATP concentrations around 10mM. For a,b and c, goodness of fit was estimated via chi^2 test returning in all cases p-values > 0.99.

3.3.4 The effects of a rational sequence modification on the QUEEN sensors: unchanged excitation spectrum.

Because of its distal position, the His-tag is unlikely to produce changes so dramatic to affect the fluorescence spectrum of the chromophore. To completely rule out this possibility, I assayed the fluorescence excitation spectrum of the sensors with and without the tag in cell lysates, while performing an ATP titration. Fig. 3.14A shows that the shape of the spectrum of QUEEN7μ* is not affected by the presence of the tag. As expected, the fluorescence signal from the sensors deteriorates for the lysates obtained from the cultures expressing dimmer sensors, such as QUEEN 2m and QUEEN 2m* (Fig. 3.14D), and the spectrum of the autofluorescence from the cytoplasm starts to emerge (Fig. 3.14C). Interestingly, in these conditions the ATP titration did not confirm the sensitivity shift towards higher ATP concentrations in QUEEN7μ* compared to QUEEN 7μ that I had observed in Fig. 3.4. Instead, both sensors showed changes in the ratio between their excitation peaks at 400 and 488nm for concentrations ranging from 0.001 to 10mM (Fig. 3.14B).

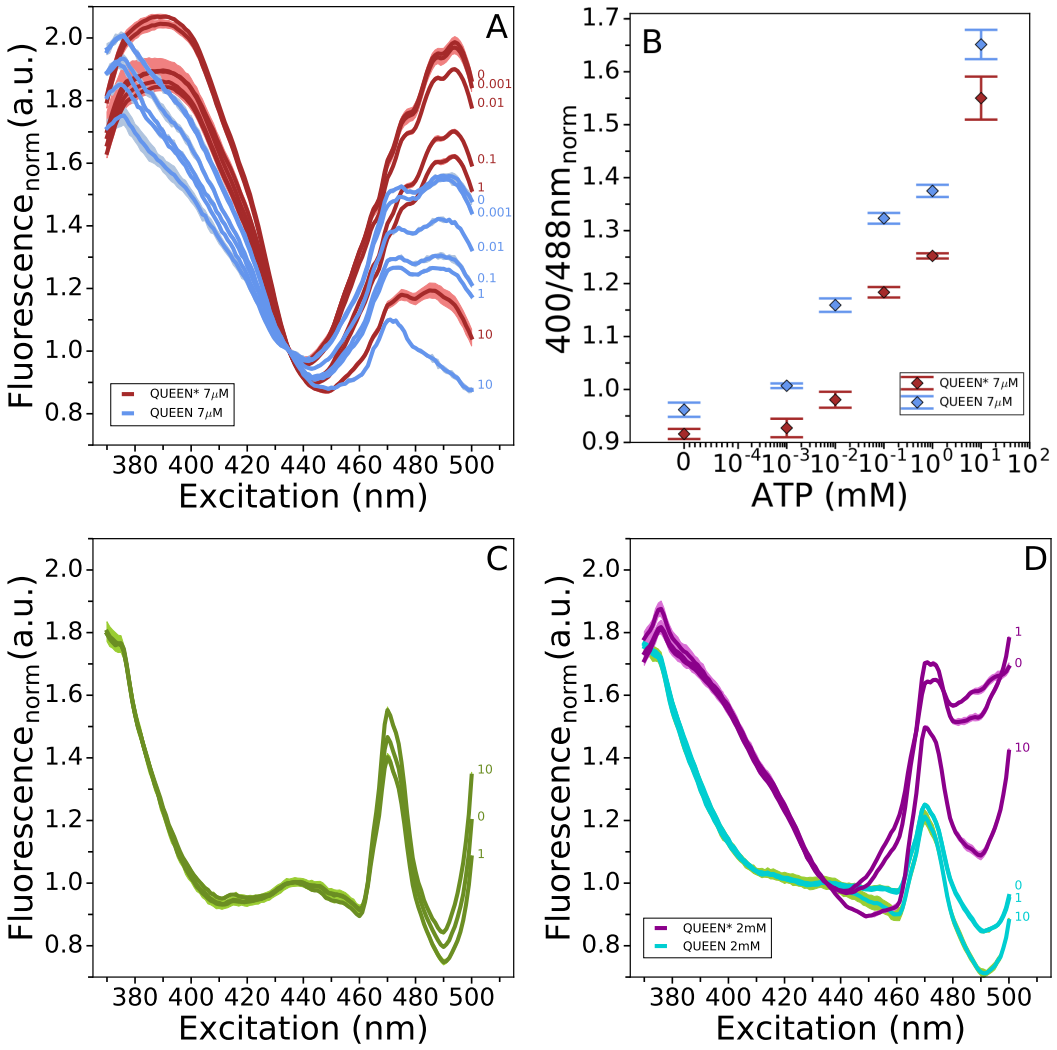

FIGURE 3.14: Spectroscopic analysis of QUEEN 7 μM and QUEEN* 7 μM cell lysates. A) Excitation spectra of QUEEN 7 μM and QUEEN* 7 μM cell lysates at 513nm emission during ATP titration normalised to their value at the QUEEN sensor's isosbestic point: 435nm. The numbers next to the traces indicate the final ATP concentration in the sample in mM. The shaded areas show the standard deviation. The experiment was carried out at 24°C. B) Ratio of the fluorescence at the two peaks of the sensor: 400 and 488nm, plotted against the ATP concentration in solution. The values were normalised to the range 0 to 1. Error bars show the standard deviation. C) Normalized excitation spectra of MG1655 wild type cell lysates. D) Normalized excitation spectra of QUEEN 2 mM and QUEEN* 2 mM cell lysates at 513nm emission

3.3.5 The sensitivity range of QUEEN 7μ and QUEEN 7μ* depends on the imaging conditions

Having optimised the sensor and the imaging conditions and verified that the removal of the his-tag was not affecting the excitation spectrum, I proceeded to characterize the sensor's calibration curve with the new imaging setup. To further improve signal-to-noise ratio, I also switched culture growth medium to rich defined medium (RDM) that has lower autofluorescence than LB. I then obtained cell lysates like before and imaged them at different ATP concentrations. The results showed that in these conditions QUEEN7μ and QUEEN7μ* share a very similar sensitivity spectrum ranging from 0.1 to 10mM of ATP (Fig. 3.15, Table 3.3). The separate analysis of the two wavelengths revealed that while the signal from the 488nm excitation peak showed a monotonically decrescent trend, coherent with the work performed by Yaginuma and colleagues, the 400nm peak showed a certain degree of quenching, which had not been reported before with the purified protein.

Sensor	Excitation	Range (mM)	Figure
Q7*	395nm/Neutral white	0.01-1	3.13C
Q7	395nm/Neutral white	0.001-0.1	3.13A
Q7*	395nm/488nm laser	0.1-10	3.15A
Q7	395nm/488nm laser	0.1-10	3.15A
Q7*	Xenon lamp	0.001-10	3.14B
Q7	Xenon lamp	0.001-10	3.14B

TABLE 3.3: Summary of the sensitivity ranges observed for the QUEEN sensors in different illumination conditions.

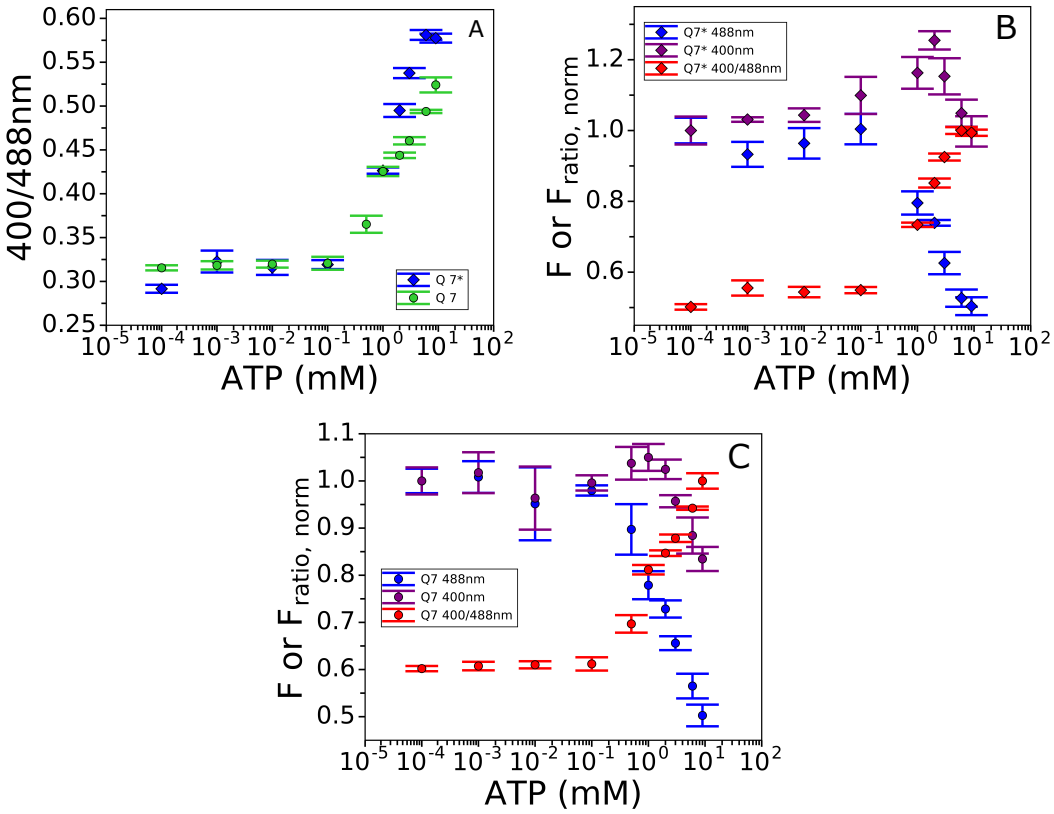

FIGURE 3.15: ATP calibration of QUEEN7μ and QUEEN7μ* cell lysates with a laser at 488nm for epifluorescent illumination. a) Comparison between lysates obtained from cells expressing the QUEEN7μ sensor that has the histidine tag at the N-terminus and QUEEN7μ that does not have the tag. b) and c) Comparison between the signal from the 400 and 488nm excitation wavelengths for QUEEN7μ* and QUEEN7μ, respectively. Fluorescence values are normalised by those at 0.0001mM ATP. The ratio is also plotted as a reference and it is normalised by the maximum value.

3.3.6 QUEEN 7μ* shows photobleaching and photoactivation *in vivo*.

Because of its sensitivity range when illuminated with the laser at 488nm and considering also its high quantum yield, QUEEN7μ* seemed suitable for assaying the ATP concentration of single *E. coli* cells over time. However, fluorescent reporters are typically affected by phenomena such as photodamage due to illumination. Characterising these effects is particularly important in ratiometric sensors, as different wavelengths might bleach differently and therefore be a source of artifacts. Thus I set out to characterize the photobleaching of the QUEEN7μ* sensor when this is exposed to different amounts of light. In the previous chapter, I have shown that illumination can directly affect cell physiology. This was also previously characterized in a sistematic manner in the lab (Krasnopeeva et al., 2019) for a mix of illumination at wavelengths of 400 nm and 475 nm, which are similar to the ones I use for QUEEN. To characterize photoeffects in a fluorescent sensor like QUEEN *in vivo*, it is necessary to make sure that signal changes are only due to illumination and not to changes in the cellular physiology. Measuring PMF is one of the most direct ways to assay cell damage caused by illumination, because light tends to permeabilize the plasma membrane probably perturbing the lipid bilayer via the formation of reactive oxygen species (Cabiscol et al., 2000; Zhao et al., 2014; Krasnopeeva et al., 2019). Therefore, to find the illumination power at which cell physiology is unperturbed, I assayed the physiological damage that the illumination of the QUEEN sensor imposes on the cells measuring PMF as a proxy. Because light damage is additive (Krasnopeeva et al., 2019), the effective power delivered to the sample can be tuned by regulating either the power of each single flash or the number of flashes. I chose the latter as this would have allowed me to maintain high signal intensity at the price of some time resolution.

In my conditions, physiological damage disappears for effective powers below 10mW/cm^2. (Fig. 3.16C). Interestingly, the functional relationship between the fitting parameter α of the PMF decay and the P_{eff} for illumination at 400 nm and 488 nm differs from that at 400nm and 475nm, in that the damage is less severe. This indicates that even a small shift towards longer wavelengths can significantly reduce light damage to *E. coli*. While constant motor speed indicates that cells maintain physiological levels of PMF, there might be changes in other aspects of cell physiology that are not directly reflected on PMF in

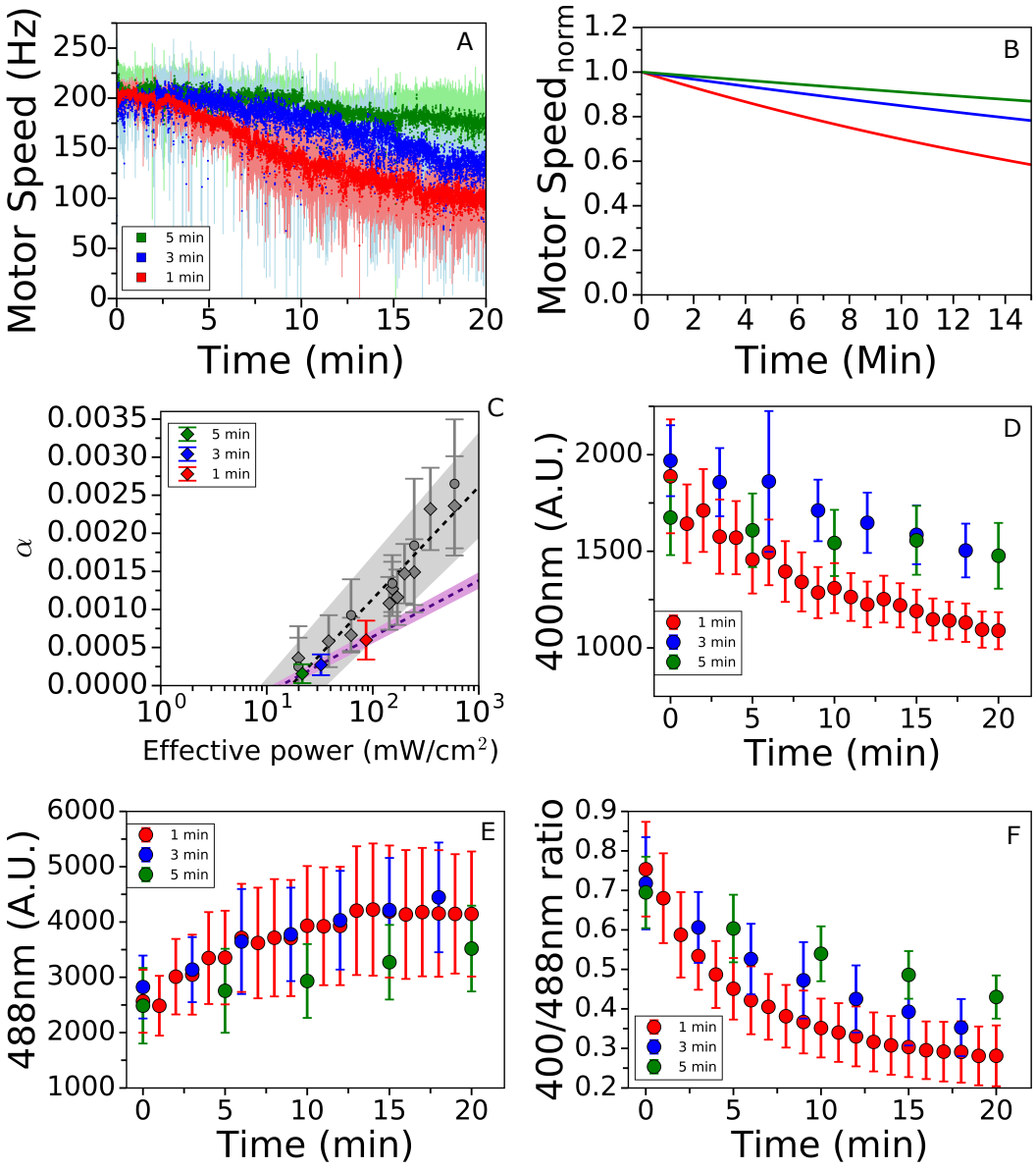

FIGURE 3.16: Optimization of the imaging conditions for ATP measurements with the QUEEN7μ* sensor. a) Estimation of light damage to cells using BFM speed as a proxy. Cells are exposed to illumination at 400 and 488nm for 20 minutes at different frequencies. b) Fits of the BFM speed decays obtained from (a). The function used is a single parameter exponential: $y = e^{-\alpha x}$ with α equal to 0.0006, 0.00027 and 0.00016 for 1,3 and 5 minute intervals between illumination events, respectively. c) α parameters from the fits in (b) plotted against the effective power, calculated as and compared to the results in (Krasnopeeva et al., 2019), which are plotted in grey. The fits are obtained with a logarithmic function: $\alpha log P_{eff} + \beta$, with α=0.00064 and β=-0.00181 for the grey trace and α=0.00032064 and β= -0.000835 for the purple trace. The shaded area shows the standard deviation.

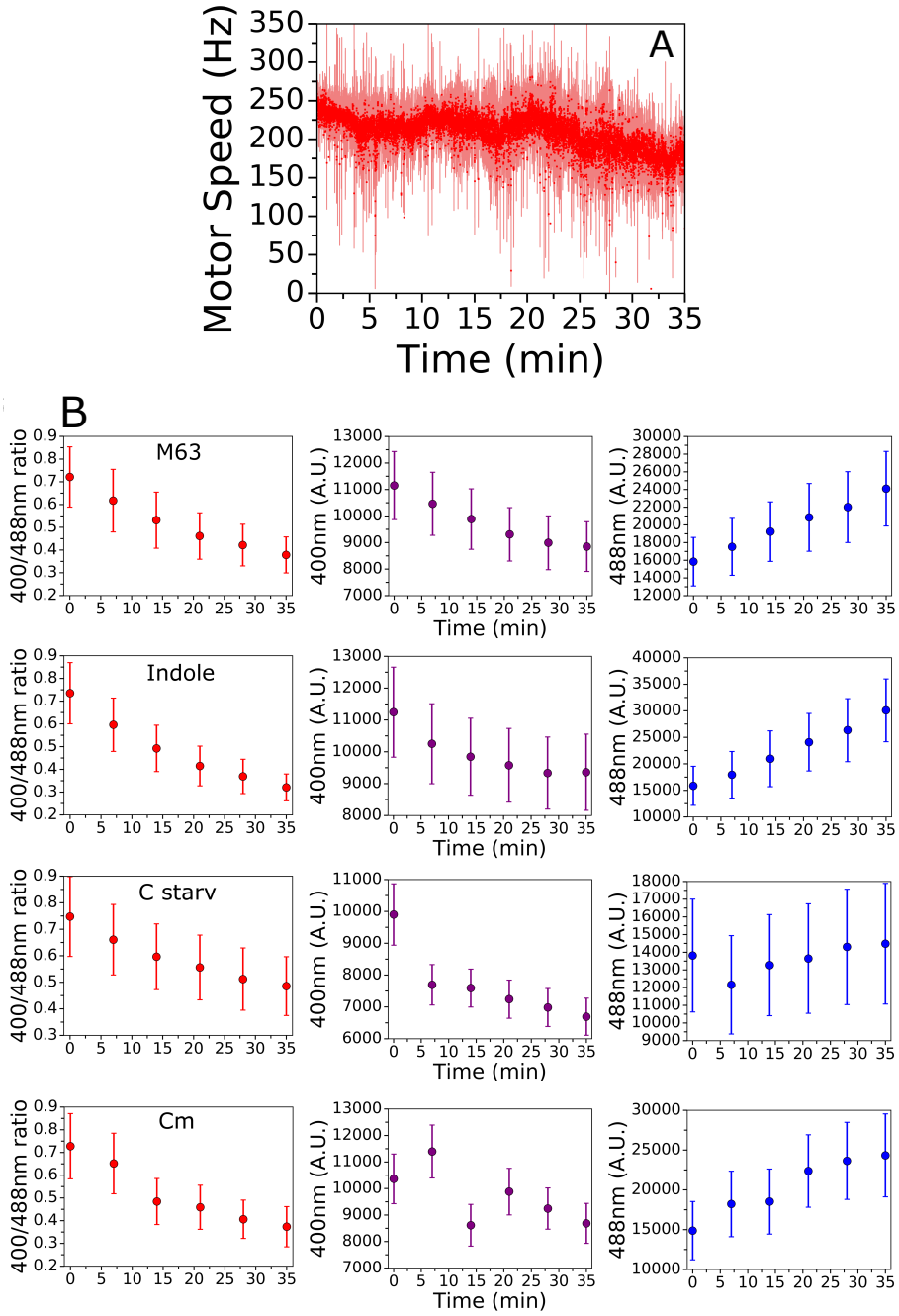

FIGURE 3.17: Photoeffects limit the use of QUEEN for time series measurements. a) Effect of the illumination of QUEEN at 7 minute intervals on the BFM speed of *E. coli* in untreated cells. In red the average trace of 5 single cells from 5 different experiments, the shaded area shows the standard deviation. b) QUEEN 7μ ratio when cells are untreated (M63), exposed to 10mM indole, to M63 deprived of the carbon source (C starv) and to 200μM chloramphenicol (Cm). The error bars show the standard deviation. In red are given the ratios between the two excitation wavelengths: 400nm (purple) and 488nm (blue).

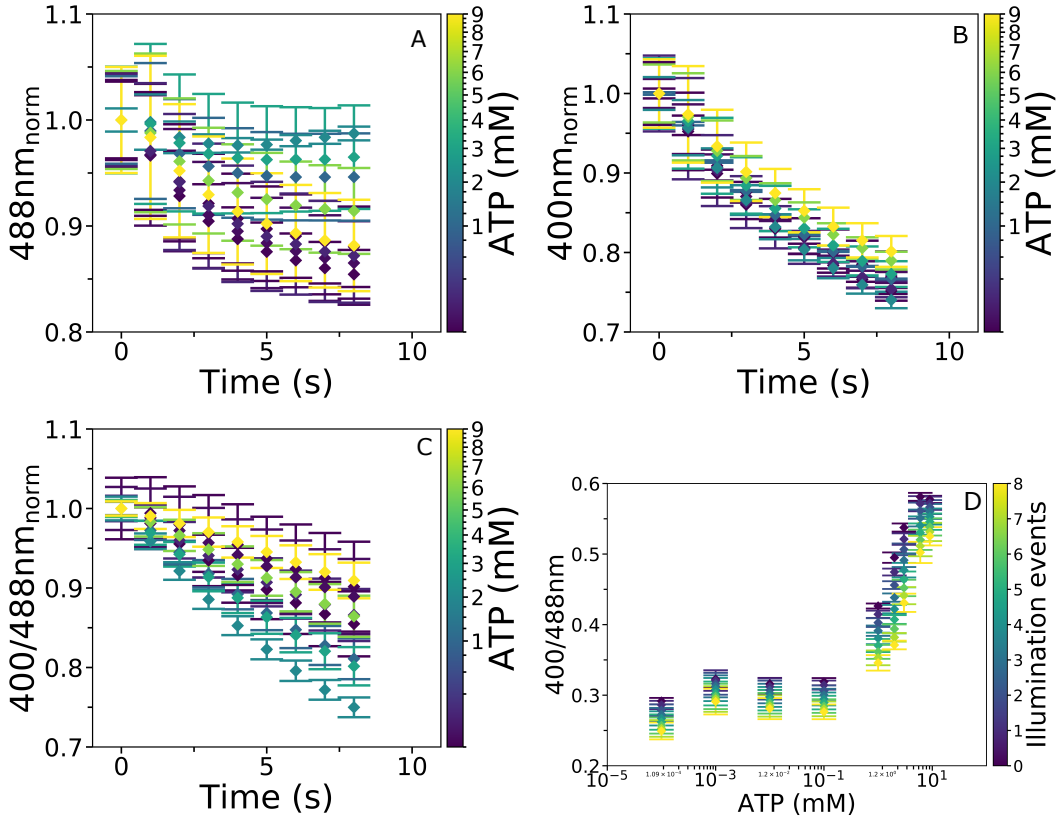

FIGURE 3.18: Photoeffects on QUEEN7μ* *in vitro*. a) Effect of illumination at 400 and 488nm on the signal of QUEEN7μ* from the 488nm excitation wavelength at different ATP concentrations, as indicated by the colourmap. b) Effect of illumination at 400 and 488nm on the signal of QUEEN7μ* from the 400nm excitation wavelength at different ATP concentrations, as indicated by the colourmap. c) Effect of illumination at 400 and 488nm on the 400/488nm ratio of QUEEN7μ* at different ATP concentrations, as indicated by the colourmap. d) Effect of illumination at 400 and 488nm on the calibration curve of QUEEN7μ*.

the time scale of the experiments. Thus, to make sure that changes in signal were only due to photoeffects, I decoupled physiology and photodamage by exposing the cells to 5% ethanol, which shuts down PMF and therefore ATP production (Krasnopeeva et al., 2019). I then assayed the photodamage for different total light powers over the same time span, finding that photobleaching too tends to disappear in these conditions when illumination is carried out at frequencies below 0.003 Hz (Fig. 3.16A,B and D). Interestingly, while the signal at 400nm excitation decreases as a consequence of photodamage, the signal at 488nm excitation increases (Fig. 3.16E), suggesting that the sensor may be affected by both photobleaching and photoactivation. Photoactivation is a known but poorly characterized phenomenon in GFP and its derivatives (Patterson et al., 2002). Because QUEEN is ratiometric, both effects have to be taken into account in time series experiments. When frequent imaging or high light intensity are required, the two photoeffects have to be characterised for the imaging conditions and subtracted from the measurements. When the total power delivered is sufficiently low the effects can be neglected. Of course, another possible explanation for a reduction in the ratio between the 400 and 488nm wavelengths could have been ATP loss, which is expected upon PMF shut down. However, cells that have been treated with ethanol have already lost PMF and to justify a light-dependent loss of ATP when PMF is zero one would need to invoke other unknown mechanisms. Further than ethanol, I tried uncoupling cell physiology from reporter behaviour by several other treatments. No matter whether cells were starved for carbon, treated with the quorum sensing molecule/ionophore indole or kept in fresh medium, the QUEEN fluorescence signal traces recapitulated the patterns I had previously observed in cells treated with ethanol (Fig. 3.16D, E and F). Taken together, these results suggested that the trends were due to photoeffects and not to an ATP decrease.

The observation that with the treatments used the trends of QUEEN7μ* ratios remained unchanged raised the question of whether QUEEN could still sense ATP in its photodamaged state. To assay that, I performed ATP calibrations *in vitro* like before (Fig. 3.15), but exposing the samples to multiple cycles of illumination. The outcome revealed several interesting points. First, that *in vitro* both wavelengths bleach as opposed to one bleaching and one photoactivating, which suggests that in the cytoplasm QUEEN7μ* experiences different conditions than in the lysates. Second, that the photobleached QUEEN can

still report ATP. Third, that the photobleaching is independent from the ATP concentration (Fig. 3.18).

3.4 Discussion

In this chapter I reviewed the state of the art in terms of ATP measurements in *E. coli* individuating two fluorescent protein sensors, Perceval and QUEEN, that could be used in *E. coli*. I first examined Perceval and its variant Perceval HR which are sensitive to the ATP to ADP concentration ratios. Because I aimed at using the sensor for time series assays, in physiological conditions and at the single cell level, I needed the protein to be expressed constitutively and with high signal. Thus, I expressed the probe from a plasmid downstream the strong constitutive promoter of the cytochrome C oxidase from *Vibrio Harveij* (Pilizota et al., 2012). In these conditions, a significant portion of the cell population would not produce any signal which was potentially indicative of toxicity (Rosano et al., 2014). Because imaging did not highlight inclusion bodies in the cells expressing Perceval, it is possible that the mechanism of toxicity might be metabolic burden and therefore that optimizing the expression level by testing different combinations of promoter strength and gene copy number the sensor could be expressed proficiently in *E. coli*. As mentioned earlier in this work, the ratio between ATP and ADP is an interesting parameter in cellular physiology and a sensor like Perceval has the potential to provide a snapshot of the ATP balance within a single observation. The optimization of its expression is therefore of significant interest for future work.

The role of the total ATP pool is less clear in cellular physiology. Rapid changes of the total ATP concentration in response to determinate stimuli are however equally telling in terms cellular energetics and ATP dynamics, as they likely indicate a shift in the ATP:ADP balance. In this chapter I demonstrated that it is possible to estimate such pool in *E. coli* with the QUEEN probe. Using an appropriate expression vector, I first showed that the sensor can be expressed in a constitutive and stable manner in *E. coli*. I then showed how a simple structural modification, the removal of the His-tag at the N-terminus, greatly increases the protein's quantum yield. Dimness was indeed a major problem for QUEEN and it had limited its use before (Yaginuma et al., 2014). I then went on showing how the removal of the his-tag does not alter the sensor's excitation spectrum, with the excitation peaks remaining placed around 400 and 488nm. The tag instead potentially alters the sensitivity range shifting it towards higher concentrations. It was not possible however to confirm this

in the illumination setup that encompasses a laser at 488nm or in the spectroscopic experiments where the light source is a xenon lamp (Table 3.3). Such dependence on the imaging setup is unexplained but not novel. In a recent paper in which QUEEN 7μM is used to estimate ATP concentration, the sensor was excited at 405 and 490nm and showed a sensitivity range that is comparable to the one I observed when using the laser (Svenningsen et al., 2019). The increased signal of QUEEN7μ* also allowed me to further characterise the optical properties of the sensor *in vivo*. Indeed, although further experiments *in vivo* are needed to confirm it, I found that the probe likely undergoes photoactivation. The phenomenon could not be reproduced *in vitro* in my conditions, which may be due to the poorly understood chemistry of photoactivation. Some reports indeed show that this phenomenon occurs when oxygen is depleted (Elowitz et al., 1997). In my experiments, cells are continuously perfused with fresh medium. Since it is known that oxygen depletion produces a characteristic drop in PMF (Schwarz et al., 2001) and this does not occur in the PMF traces of cells in which QUEEN is photoactivated, I can conclude that oxygen is metabolically available. However, it is possible that oxygen might be excluded in the proximity of the sensor's EGFP chromophore in the cytoplasm. One experimental strategy that could potentially clarify the role of oxygen in the photoeffects of QUEEN7μ* is to supplement reagents for an oxygen scavenging reaction to QUEEN lysates while these are being exposed to light. The reaction between glucose oxidase, catalase and -D-glucose was indeed used previously to characterize the photoactivation of GFP (Elowitz et al., 1997). To assay photoeffects it is necessary to uncouple the sensor from cellular physiology, for example by limiting ATP variations. Halting ATP production by poisoning the respiratory chain via substances the likes of cyanide or sodium azide is an often used strategy (Yaginuma et al., 2014). The ethanol treatment I performed inspired by (Krasnopeeva et al., 2019) produces essentially the same effect without the need for handling highly toxic compounds. However it should be highlighted that these strategies cause a stop in ATP production but not in its consumption and therefore ATP levels can in principle still vary. In the chapter I demonstrated that the protein is still capable of sensing ATP concentration when photodamage is administered *in vitro*, while the opposite seem to be true *in vivo* probably because of photoactivation. The sensor should thus be used minimising illumination to limit the contribution of photoeffects on the ATP concentration readouts.

Chapter 4

Measurement of energy parameters in dormant *E. coli*

4.1 Introduction

Little is known about cellular physiology during dormancy. In this chapter dormancy is examined from the perspective of cells that, after having grown for a long time in a constant environment and having reached balanced growth, suddenly encounter growth-prohibiting conditions such as high concentrations of indole, a quorum sensing molecule, chloramphenicol, a bacteriostatic drug, and carbon starvation. Observations from this point of view have several advantages. As a first instance, balanced growth eliminates artifacts in cell-to-cell variability that could be due to carry over cells from previous experimental stages such as overnight culturing. Balanced growth also elicits a physiological state in which all of the rates of cellular processes are constant. Once cells have entered in such a state, the condition can be maintained indefinitely upon appropriate culture dilution, which enhances measurements reproducibility. Lastly, cells in balanced growth express a number of bacterial flagellar motors that is compatible with high spinners yields during the bead assay. In certain infections, cells experience periods of feast in which conditions are comparable to those encountered during exponential growth. When the infection causes symptoms, the environmental conditions quickly change, in example because the patient alters its normal habits or initiates treatments. Therefore, the energetics measurements I present in this chapter, which I carry out during conditions shift and upon dormancy establishment, are likely to be informative under a clinical perspective.

4.2 Materials and methods

4.2.1 Strains

Strain	Genotype	Plasmid
EK01-QUEEN7μM*	ΔFliC	pWR20-QUEEN7μM*
EK07	ΔFliC,pHluorin	/
HE608	ΔFliC	/

4.2.2 Culture conditions

Cultures were grown to steady state from single colonies, isolated on LB agar plates that were kept at 4°C for a maximum of one month. Single colonies were inoculated in 10ml LB (0.5% Yeast Extract, 1% Bacto tryptone, 0.5% NaCl) and grown at 37°C for 3-4 hours. Cells were then transferred to M63 medium (13.6g/L KH2PO4, 0.5mg/L FeSO4.7H20, 0.5g/L MgSO4.7H20, 1.27mg/L Thiamine, 2.6428g/L (NH4)2SO4, 0.5% glucose), MM9 (50mM Na_2HPO_4, 25mM NaH_2PO_4, 8.5mM NaCl, 18.7mM NH4Cl, 0.1mM $CaCl_2$, 1mM KCl, 2mM $MgSO_4$, and 0.3% glucose) or MOPS medium (40 mM MOPS, 4 mM tricine (adjusted to pH 7.4 with NaOH), 1.32 mM KH2PO4, 0.523 mM MgCl2, 0.276 M Na2SO4, 0.1 mM FeSO4, 0.1 M NaCl, 20 mM NH4 and either 20mM glucose or 20mM fructose or 5mM mannose) with a 10^{-7} dilution and maintained below OD 0.5.

4.2.3 Plate reader

For estimating growth upon dormancy induction, optical density of cells was continuously estimated in a Spectrostar Omega microplate reader (BMG, Germany) using a flat-bottom 96-well plate that was covered with a lid during the experiments (Costar, UK). Cells were harvested from steady state cultures by centrifugation at 8000G for 2 minutes at 37°C and washed twice in the medium of destination to minimize medium carry over. In the case of indole and chloramphenicol, cells were simply transferred into M63 medium supplemented with 10mM Indole (Sigma, USA) or 200μM chloramphenicol. Final sample concentration was in the region of OD 0.3, such that the first readings would have been already in the range of sensitivity of the plate reader. Plates were loaded in the pre-warmed plate reader with the idea of keeping the temperature as constant as possible. Cells adjacent to those containing the samples

were loaded with water and optical density was assayed every 12 minutes for 5 hours, minimizing OD increases due to evaporation. Between every reading, the plates were shaken at 700 rpm with a double orbital mode.

4.2.4 Fluorescence microscopy and BFM speed estimation

For fluorescence imaging and BFM speed estimation cells were harvested from steady state cultures and flagella were sheared by passing the cells through two syringes with narrow-gauge needles (26 gauge) connected by plastic tubing. Sheared cells were then spun down at 8000G for 2 minutes and the pellet resuspended in half the initial volume. Flow cells were flushed with Poly-L-Lysine and immediately washed with roughly 10 flow chamber volumes (2.5ml) of water and 1 ml of M63. Cells were then loaded in the slide and incubated for 10 minutes. Cells that did not stick to the surfaces of the chamber were washed out with 1 ml of M63 and a suspension of beads with diameter 0.5μm (Polysciences, US) was flown in the chamber and incubated for further 10 minutes. Beads in excess were washed away with 1 ml of M63 and the slides brought to a pre-warmed fluorescence microscope. The whole procedure was carried out at 37°C and all the liquids had been pre-warmed. For the estimation of cytoplasmic pH with pHluorin, cells were imaged with an iXon Ultra 897 EMCCD camera (Andor, UK) (Rosko, 2017; Krasnopeeva, 2018) at 90 second intervals with a 50ms exposure time and 100 camera gain. Illumination was provided by a 395nm LED and the neutral white LED (Cairn Research Ltd, UK), with no excitation filter for the first and ET470/40x filter (Chroma Technology, USA) for the second while emission was collected at the same wavelength in both cases with a ET525/40m filter (Chroma Technology, USA). For the estimation of ATP concentration the same illumination hardware was used excepted that illumination at 488nm was provided by a laser (VLT, USA). For the control experiment (M63 in Fig. 4.4), images were taken from five well spaced (i.e. more than three fields of view of distance) fields of view at the beginning of each experiment and BFM speed estimated from five different cells for five seconds each. The samples were then treated with 10mM indole, M63 deprived of the carbon source or chloramphenicol for 15, 10 and 30 minutes, respectively. It should be noted that because of the length of the tubing used in the flow chamber, the transition between media only happened after three-four minutes from the start of the recordings. BFM speed of one single cell was

monitored to ensure that the treatment was being carried out as expected. This was done with the focus of the microscope moved several fields of view away from the region in which the previous images had been taken. After the treatment, images were taken from ten well spaced fields of view and BFM speed estimated from 10 different cells for five seconds each. The BFM speed was estimated via back-focal plane interferometry as explained previously (Rosko et al., 2017). In all conditions, media was flown with a syringe pump at a rate of 100μl per minute.

The motor speeds in Fig. 4.4 were obtained similarly, by measuring single spinners for five seconds each, from cells grown to steady state in the various media indicated in the legend. Here, growth media was flowed in the slide throughout the experiment.

4.2.5 Calibration of the pH and ATP sensors

To calibrate pHluorin *in vivo*, cells were loaded in a flow slide and exposed to M63 at various pre-defined pHs and 40mM PBMH for at least ten minutes. Values were averaged and plotted together with their standard deviation. Data points were fitted with a logarithmic function with four parameters as in (Krasnopeeva, 2018): $y = \alpha e^{\beta(x-\gamma)} + \delta / e^{\beta(x-\gamma)} + 1$, where α, β, γ and δ are equal to: 1.32910933, 1.30675219, 6.37473758 and 0.07666277 respectively. The calibration of QUEEN7μ* *in vitro* has been explained previously in Chapter 3. Data points were fitted with the same sigmoid function with α, β, γ and δ equal to: 0.58180951, 0.70747778, -1.28012047 and -0.36657943, respectively.

4.2.6 Data analysis

Plate reader data

The initial optical density reading of each individual growth curve was subtracted from the rest of the trace. Curves from different repeats were averaged and the standard deviation estimated.

BFM speed data

Raw traces of the position of the bead attached to the filament stub were analyzed by a moving-window discrete Fourier transform as in (Rosko et al.,

2017). From the obtained motor speed traces DC frequency (50 Hz) was removed, speeds lower then 5 Hz ignored, and subsequently a median filter (window size 31) was applied (Krasnopeeva et al., 2019). It should also be noted that I used a wild type strain for which the BFM can change rotational direction, which appears as a negative speed after application of the moving-window Fourier transform. However, for the purpose of PMF measurements these short intervals can be disregarded, and I only show the speed values above 0 Hz.

Fluorescence microscopy data

The image analysis was carried out with a custom written python script. Fluorescence images were initially inspected for unevenness of the field of view, which can sometimes arise if the sample or the microscope stage are slightly tilted. If a tilt was observed, portions of the images that were out of focus were cut off. To individuate the cells, objects with high grey values were automatically identified by applying a global threshold via the Otsu's method (Otsu, 1979). The resulting regions were then filtered for size and aspect ratio, using parameters that had been optimised for the individuation of cells grown at steady state with a growth rate of 0.7 hours^{-1}, lying flat on the flow chamber surface. Total cells' intensity values were obtained by summing up and averaging pixels within the region thus selected.

4.3 Results

Carbon starvation, bacteriostatic drugs and quorum sensing molecules can induce dormancy.

Dormancy is associated to stress survival. To investigate whether this is simply due to growth stop or to other physiological changes that cannot be observed by analysing the growth rate alone, I simultaneously measured PMF, ATP concentration and cytoplasmic pH of *E. coli* while inducing growth arrest in several different ways. I individuated dormancy inducing conditions by growing cells to steady state, quickly washing them into growth limiting media, and immediately transferring them in a plate reader to observe whether growth would have stopped. Amongst the media tested I found that indole, a quorum sensing molecule thought to undertake ionophore capabilities when highly concentrated, induced complete growth suppression when present at concentrations equal to 10mM (Fig. 4.1A). Chloramphenicol, a bacteriostatic drug, seemed to induce a sudden growth halt at a concentration as low as 31μM. After 3 hours of incubation with the antibiotic, some of the curves showed a slight increase in optical density (Fig. 4.1B). Visual examination of the wells of the 96-wells plate however, revealed that this was not due to growth but rather to cell sedimentation. To be sure that cell growth was halted and to maintain coherence with other attempts in the literature to suddenly stop cell growth by using chloramphenicol (Pilizota et al., 2012), a final concentration of 200μM was chosen. Transfer of the cells via centrifugation into M63 medium deprived of the carbon source also induced an immediate growth stop. Interestingly, it was not possible to obtain the same effect by removal of the nitrogen source, perhaps indicating, as pinpointed by others before (Kim et al., 2012), that nitrogen traces available to *E. coli* are present in common labware.

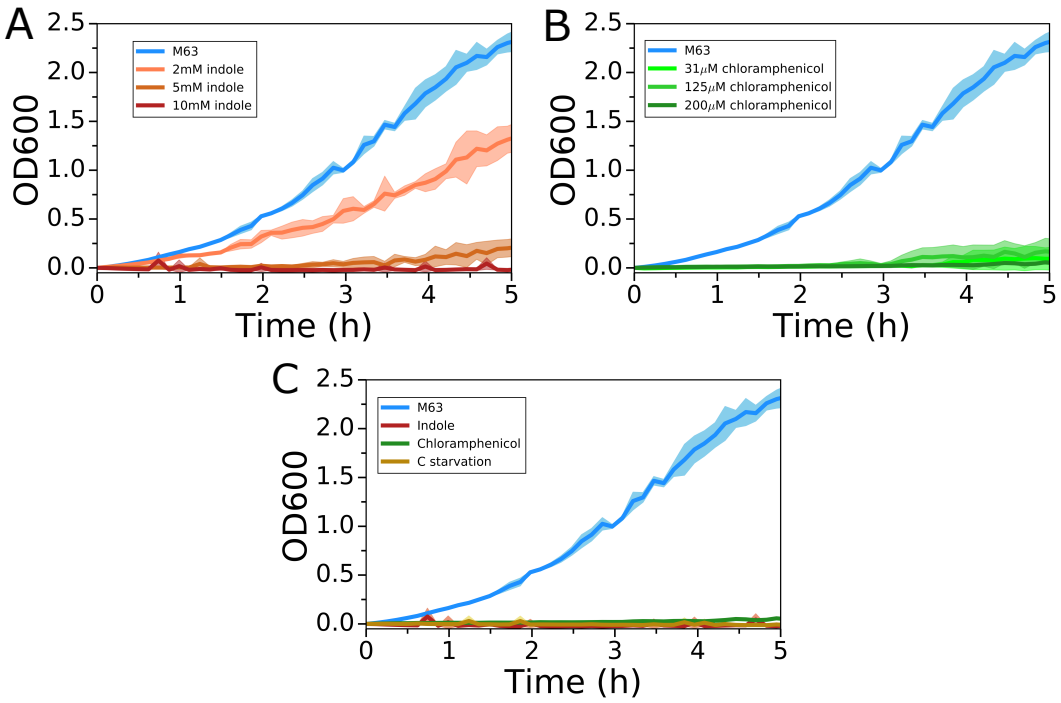

FIGURE 4.1: Individuation of dormancy inducing conditions by monitoring cell growth in plate readers. a) Assay of optical density of an *E. coli* culture immediately after addition of 0, 2, 5 and 10mM indole to the growth medium. b) Assay of optical density of an *E. coli* culture immediately after addition of 0, 31, 125 and 200μM of chloramphenicol to the growth medium. The control where no addition to the growth medium was made is re-plotted from (a). c) Dormancy inducing conditions: growth medium without carbon source, 10mM indole and 200μM chloramphenicol, are compared to normal growth medium (M63).

4.3.1 Simultaneous measurement of PMF, ΔpH and ATP concentration reveals energetic nonequivalence of dormancy.

Using the QUEEN7μ* and pHluorin I had characterised and calibrated before (Fig. 4.2) and the bacterial flagellar motor assay, I measured PMF, ATP concentration and cytoplasmic pH of cells while they were entering into dormancy, as this was induced via indole and chloramphenicol treatment and carbon removal. While the dynamics of ΔpH and PMF could be followed dynamically over time, the photoeffects evidenced by QUEEN recommended a more cautious approach for ATP estimation, which was therefore carried out only once per field of view. Because of this and because the wavelengths of pHluorin and QUEEN overlap, ΔpH and PMF were first measured over time simultaneously in one set of experiments. In a second set of experiments, PMF was first measured over 5 seconds from multiple cells, while fresh M63 was flowed. Immediately after, ATP concentration was estimated from multiple fields of view. Cells were then subjected to dormancy-inducing conditions. To make sure that the treatment had the same effects seen in Fig. 4.3, PMF was continuously measured during cell exposure to the conditions (Fig. 4.4A, B and C). After the treatment, multiple cells and fields of view were again assayed for PMF and ATP concentration. The results showed that all of the dormancy-inducing treatments yielded a reduction of the energy parameters from their initial state, but were significantly different from each other (Fig. 4.4D). In the case of chloramphenicol in example, differently to what previously estimated by others (Allison et al., 2011), ATP, ΔpH and PMF levels hardly changed. In the case of carbon starvation, PMF was halved and so roughly was the ΔpH. Also the ratio between the two excitation peaks of QUEEN decreased. ATP and PMF decrease was even more obvious in the indole-treated cells, nearing zero for the latter and thus confirming that the chemical might be a ionophore. Interestingly, although indole is thought to be a protonophore, according to my measurements performed with pHluorin and its calibration with PBMH, ΔpH did not become zero. Taken together, these results showed that the energy parameters dominating the physiology of dormant *E. coli* are highly dependent on environmental conditions and on the reasons for which dormancy was acquired.

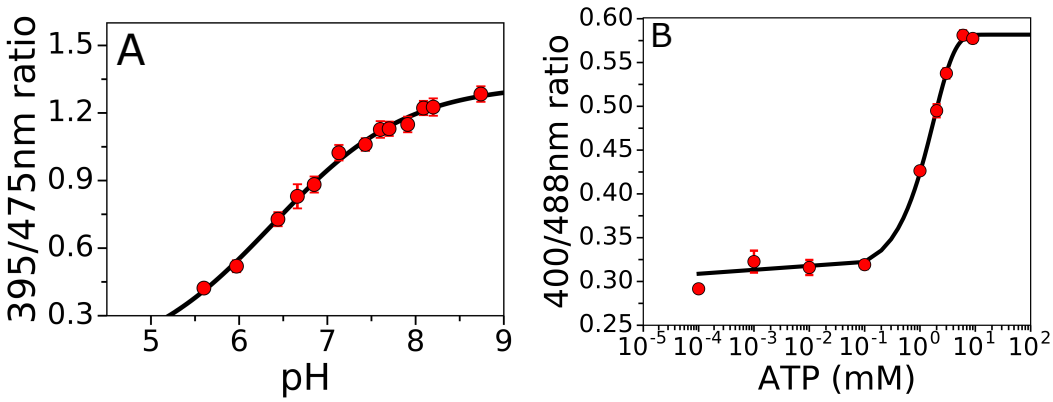

FIGURE 4.2: Calibration of protein sensors for intracellular pH and ATP concentration measurement at 37◦C. a) *In vivo* pHluorin calibration performed by collapsing the intracellular pH with 40mM PBMH for 10 minutes at different external pHs. The sigmoid fit is $y = \alpha e^{\beta(x-\gamma)} + \delta / e^{\beta(x-\gamma)} + 1$, where α, β, γ and δ are fitting parameters as in (Krasnopeeva, 2018) and the values are: 1.32910933, 1.30675219, 6.37473758 and 0.07666277 respectively. b) *In vitro* QUEEN7μ* calibration performed in lysates. Data points are replotted from Fig. 3.15A. The fit is performed with the same sigmoid of (a), but with α, β, γ and δ equal to: 0.58180951, 0.70747778, -1.28012047 and -0.36657943, respectively.

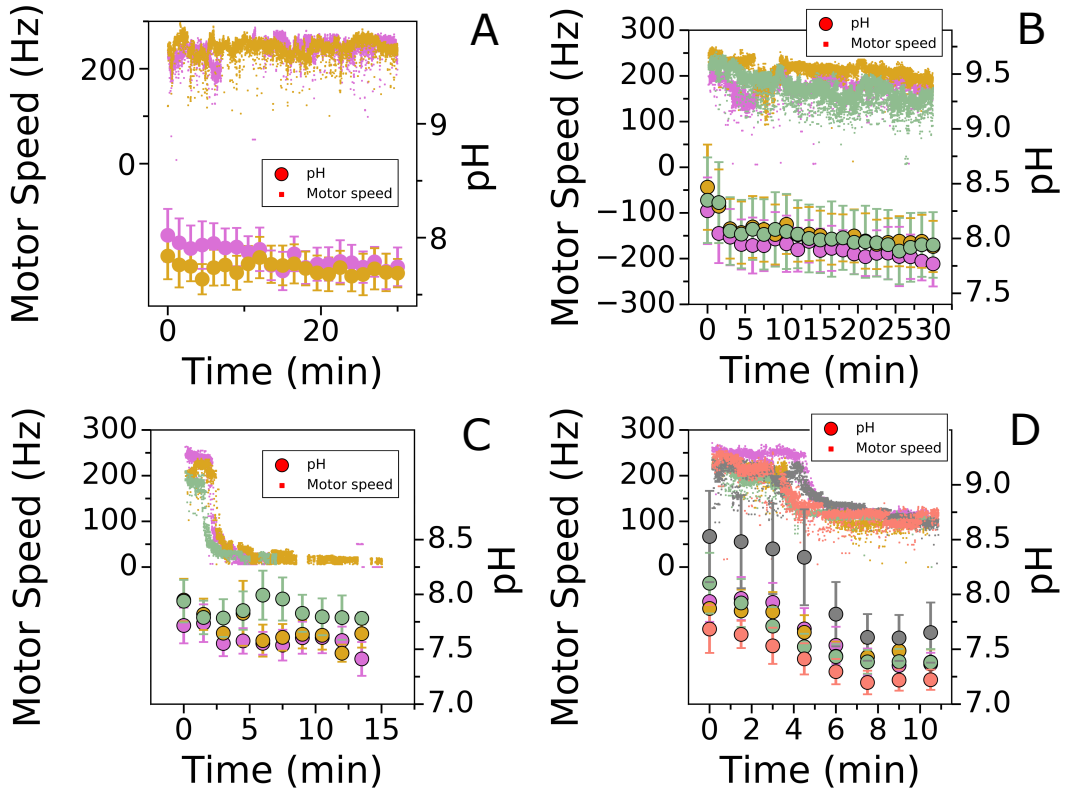

FIGURE 4.3: Simultaneous single cell time series measurements of BFM speed and intracellular pH upon dormancy induction. BFM speed and cytoplasmic pH are indicated by small rectangles and big circles, respectively. a) Continuous perfusion of fresh growth medium for 30 minutes. b) Continuous perfusion of growth medium + 200μM chloramphenicol for 30 minutes. c) Continuous perfusion of growth medium + 10mM indole. d) Continuous perfusion of growth medium lacking a carbon source. In the 4 experiments, the switch between media happens after 2-5 minutes from the start of the recording. External pH was maintained constant at 7.2 in all the experiments.

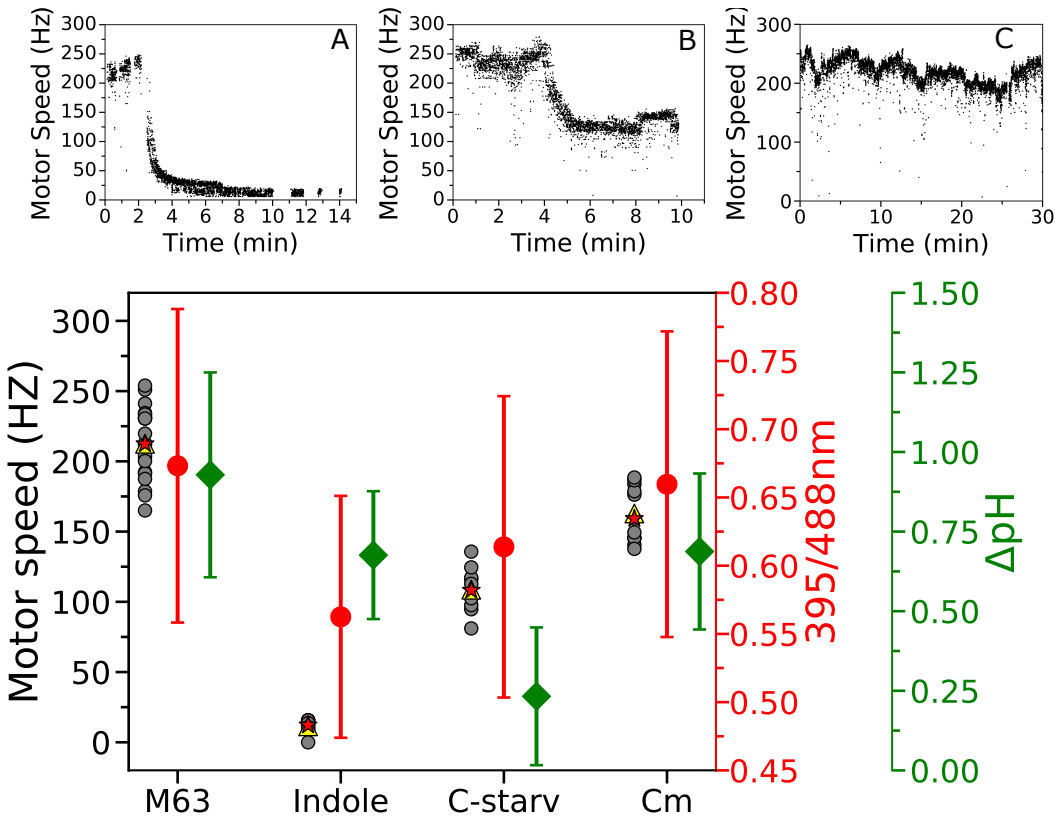

FIGURE 4.4: Energy parameters of dormant cells compared to growing ones. ΔpH values were estimated from the measurements taken at minute 10.5 in Fig. 4.3. ATP and BFM speed values were estimated from multiple cells and fields of view at the beginning of the recording for the growing cells, after 15 minutes for the indole treatment, after 10 minutes for the carbon starvation condition and after 30 minutes for the chloramphenicol treatment. The BFM speed traces measured during the treatments are coherent with those observed in Fig. 4.3 and are given in a) for indole, in b) for carbon starvation and in c) for chloramphenicol.

4.3.2 Upon carbon removal, cells use different, environment-dependent strategies to reach a certain PMF level.

In the previous paragraph I showed that removing the carbon source prompted a sudden drop of PMF and pH to a non-zero level. I wondered whether this PMF baseline depended on the remaining ΔpH. If this was the case, there could potentially have been pH conditions in which cells were more or less affected by carbon starvation. To find out whether the level of the PMF baseline depended on the residual ΔpH, I altered the pH of the carbon-free M63. I tested 4 pHs, which are within the range in which *E. coli* can grow: 6.7, 7.2, that is also the pH of the M63 in which cells are grown, 7.7 and 8.2. Interestingly, after the shift in the starvation medium, BFM speed tended to settle on very similar values independently from the pH of the carbon starvation medium. ΔpH instead showed some variability, with values ranging from -0.25 to 0.6 for external pHs going from 8.2 to 6.7, potentially portraying a linear dependency (Fig. 4.6). To confirm that in these conditions I was actually measuring ΔpH and PMF, I supplemented the cells with the PBMH mixture, which, as expected, further collapsed the remaining cytoplasmic pH to the value of the external medium and further decreased PMF (Fig. 4.5). The remaining PMF had thus to be provided by membrane voltage. To confirm it, I collapsed V_m supplementing the medium with additional potassium and valinomycin, which is an antibiotic that acts as a potassium ionophore (Ahmed et al., 1983; Varma et al., 2008). By subjecting the cells first to a medium with 300mM potassium, which did not significantly affect PMF, and then to a medium with 300mM potassium and 50μM of valinomycin, I was able to confirm that membrane voltage was responsible for the remaining PMF (Fig. 4.7).

Medium	Strain	Growth rate
MOPS mannose	HE608	0.33
MOPS fructose	HE608	0.73
MOPS glucose	HE608	0.87
M63	EK07	0.74
M63	EK01-QUEEN7μ*	0.73
MM9	EK07	0.7

TABLE 4.1: Growth medium, strains and growth rates for the experiments in Fig. 4.8

4.3.3 The proton motive force saturates after a threshold growth rate

In the cases examined, the energetics of dormancy depend on the conditions that induced it. However, it is reasonable to think that the life history of the cells might play a role too. In the experiments presented in this chapter, cells were grown to balanced growth, mimicking infections in which bacteria experience a continuous state of feast. In other cases, cells are thought to experience periods of starvation undergoing cycles of feast and famine, such that the accumulation of storage carbohydrates plays an important role in their colonization capabilities (Jones et al., 2008). Such stocks might in example define the rate at which energy is lost during the acquisition of starvation. Another possibility is that, even in a continuous state of feast, the quality of the nutrients used during this period might condition the energy levels during dormancy. To test this hypothesis, I initially characterised the PMF levels of bacteria grown to balanced growth in media with different nutrient qualities. Nutrient quality positively correlates with the growth rate, thus I expected that cells growing at faster rates would have had higher energy levels. Interestingly, I found that while this is true in a certain growth rate range, the correlation is not linear across the whole growth rate spectrum, but, reached a certain threshold, the PMF stops increasing. Future work will show whether cells that have been grown in different nutrient qualities acquire the same energy levels upon entrance in a dormant state.

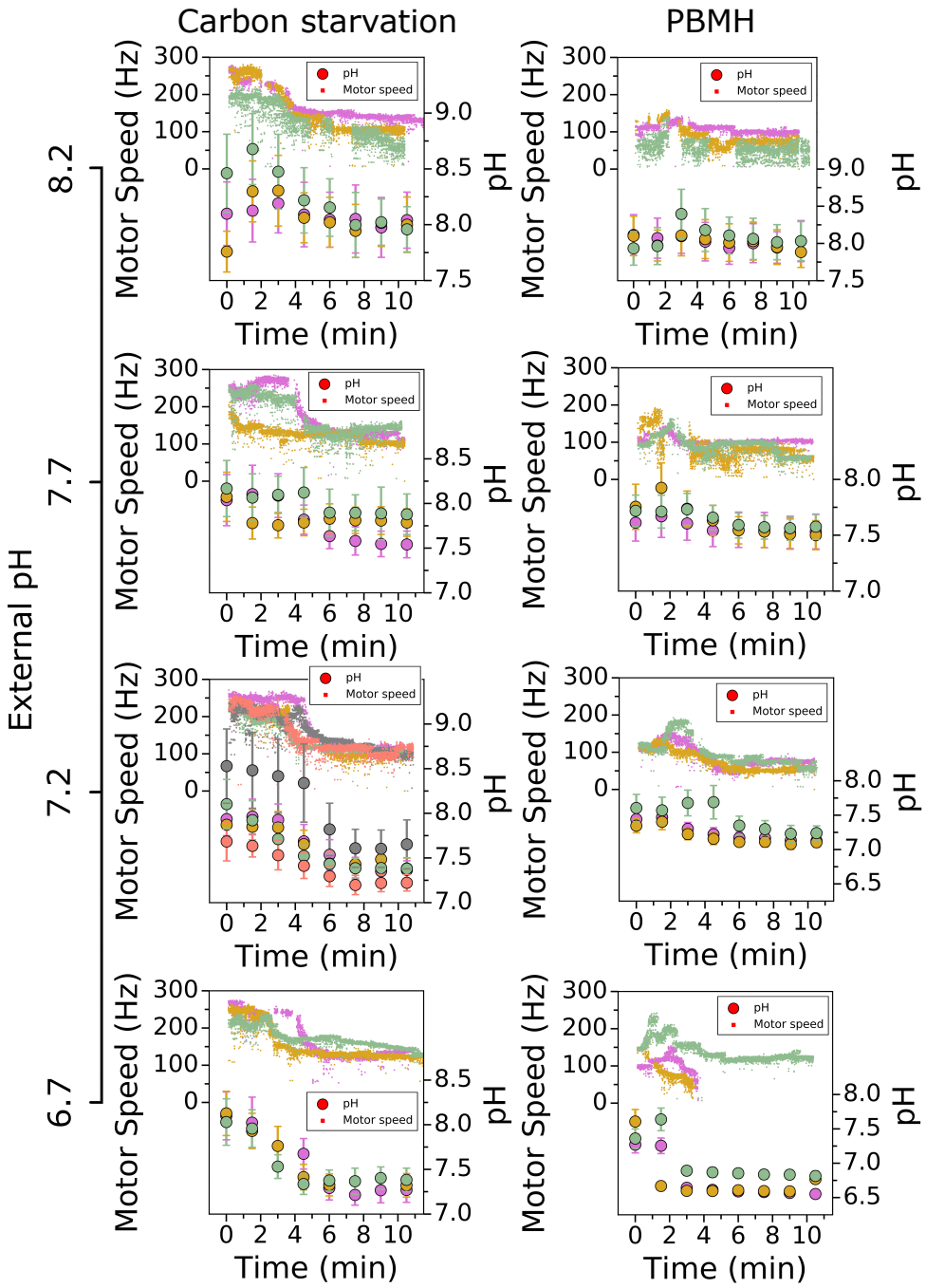

FIGURE 4.5: Induction of dormancy via carbon starvation at different external pHs and ΔpH collapse with 40mM PBMH. pH of the carbon starvation shift decreases from top to bottom, the left column shows shifts into carbon starvation medium, while the right column shows shifts to the carbon starvation medium with addition of 40mM PBMH. Motor speed is indicated by small squares, while cytoplasmic pH is shown by circles. The error bars represent the standard deviation across the cell population analysed. In each experiment, PMF and cytoplasmic pH are measured from a single cell and from all the cells in a field of view, respectively. Same marker colors denote data obtained from the same experiment.

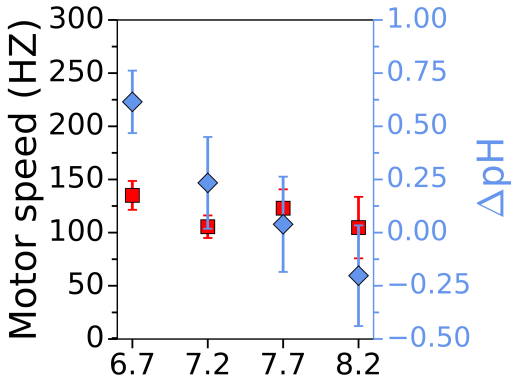

FIGURE 4.6: ΔpH and PMF dependence on external pH upon carbon starvation. PMF and cytoplasmic pH were estimated from the traces shown in Fig. 4.5 after 10 minutes from the start of the experiment.

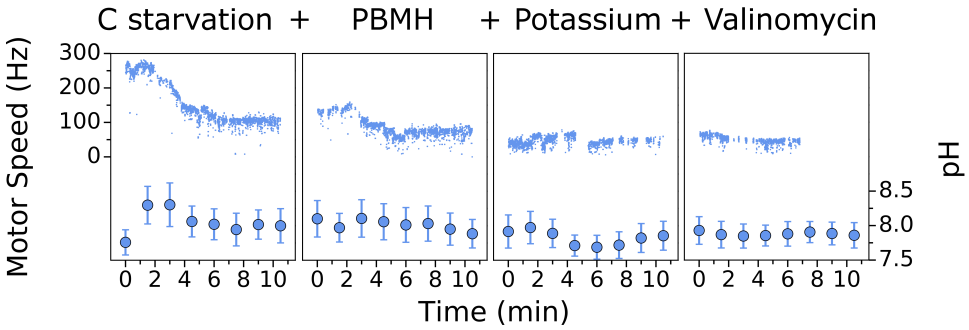

FIGURE 4.7: Sequential collapse of DeltapH and membrane voltage using PBMH and valinomycin. Panels from left to right, sequential transitions from: M63+Glucose growth medium to M63 without carbon source, to M63 without carbon source and 40mM PBMH, to M63 high in potassium (300mM) without carbon source and 40mM PBMH, to M63 high in potassium (300mM) without carbon source, with 40mM PBMH and 50μM valinomycin. In each panel, the transition between media occurs after 3-4 minutes from the start of the recording.

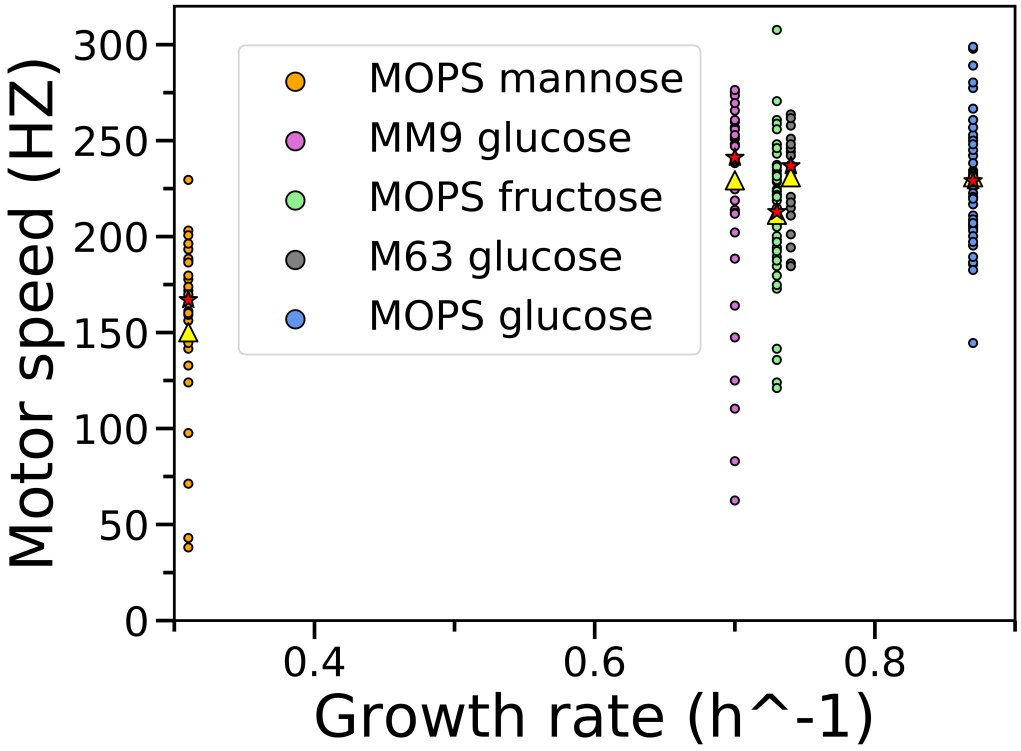

FIGURE 4.8: BFM speed measured from single cells grown to balanced growth in media with different nutrient quality. The star and triangle indicate mean and median, respectively. The M63 condition has 21 single cells, the MOPS mannose has 30 and all the others have 50 or more. The growth rates and strains used are reported in Table 4.1. The motor values reported in this plot for M63 glucose are for the strain EK07.

4.4 Discussion

In this chapter, I examined the energy parameters of *E. coli* single cells during their entrance and settlement into dormancy, which I defined as a state in which cells are viable but are not growing. I chose to focus on this state for several reasons. Dormancy is a hallmark of persistence and tolerance and is therefore of significant clinical interest. By being an extreme form of growth reduction, it is on one hand relatively easy to study, as one simply needs to ensure that the chosen experimental conditions prompt cell number to remain stable over time, but on the other hand it can potentially provide insights on the mechanisms that allow antibiotic survival in the slow growing regimes too.

With these concepts in mind, I first individuated three experimental conditions that sharply induced growth arrest, using optical density measurements over time in a plate reader, as a proxy for cell number: M63 without carbon source, M63 with 10mM indole and M63 with 200μM chloramphenicol (Fig. 4.1C). It should be noted that in Fig. 4.1, traces are normalised to OD readings at time = 0. However, to make sure that growth stops immediately or that cell number does not decrease, which are necessary conditions for assuming that cells are dormant, cell suspensions were added in the wells at an initial OD around 0.2, which is within the sensitivity range of the instrument. Because of this, flat traces were considered a good indication of cell dormancy. Of course a flat trace might be also the result of equal growth and death rates, a hypothesis that was then excluded via single cell level microscopy experiments. Having found conditions that could induce dormancy, I proceeded to measure their energy parameters finding significant differences. I indeed demonstrated that upon a shift into the same medium but deprived of the carbon source, BFM speed was halved, ΔpH fell to values close to a quarter of point of pH and also ATP concentration decreased. These changes in BFM speed and ATP concentration were even more pronounced in cells treated with indole, with the first in particular very close to zero. The ΔpH in these cells however, remained relatively high, a peculiar result considered that the PMF amounts to zero. While the relatively high ΔpH and the zero PMF might be explained by a positive membrane voltage, previous results (Krasnopeeva, 2018) suggest another explanation. Indeed, for reasons that are still under investigation, there can be significant differences in the *in vivo* calibration of pHluorin when this is performed using indole or PBMH (Fig. 4.9), and this might explain the non

zero ΔpH value of cells treated with indole. In this work I chose PBMH as a pH collapsing agent, because it produces the same calibration curve for *in vivo* and *in vitro* experiments. One way of clearing the doubt would be to perform the calibration of pHluorin with indole in my conditions and then use it to convert fluorescence ratio to pH for the cells that have been treated with the substance. While this will be carried out in the future, the ΔpH is here plotted as zero, based on the assumption that indole is a protonophore and therefore collapses internal pH to the external one (Fig. 4.10). In the case of the bacteriostatic drug chloramphenicol, the first 30 minutes of treatment revealed only small reductions in BFM speed and ΔpH which are coherent with other works showing that bacteriostatic drugs cause a reduction of the respiratory rate (Lobritz et al., 2015). ATP levels, however, showed a slight decrease, contrary to the previous notion that the rate of accumulation of ATP due to protein synthesis can not only make up but surpass the reduced production rate due to the reduced respiratory rate (Lobritz et al., 2015). This difference could be explained by the fact the cells in my experiments and in the experiments performed by Lobritz and colleagues are in different physiological states. In my case, cells have been grown to steady state and have therefore reached the maximum growth and metabolic rate allowed by the medium, minimizing the carry over of cells from stationary phase. Lobritz and colleagues instead only diluted cells 1:200, which is unlikely to produce steady state. Although hypothetical, the idea that cells in the relatively early stages of outgrowth from the stationary phase and in steady state might have significantly different respiratory and protein synthesis rates is intriguing. Experiments carried out by others in the lab, with cells that have not reached balanced growth, show a significantly less sharp BFM speed drop upon shift into poor medium than that I observed in Fig. 4.3D and 4.5 (personal communication).

Another point that should be noted is that when QUEEN ratios are converted to ATP, these yield values that are towards the highest extreme of the sensitivity range of the protein. In the previous chapter, I only assayed the calibration of QUEEN up to a concentration of 10mM, as the curve sharply leveled. It would be interesting to verify such sharp plateau with higher concentrations, particularly because the highest ratios measured *in vivo* are slightly higher than the maximum ratios obtained in the current *in vitro* calibration. In addition, the authors that first proposed QUEEN, observed a certain difference between *in vitro* calibration and *in vivo* measurements, which they corrected

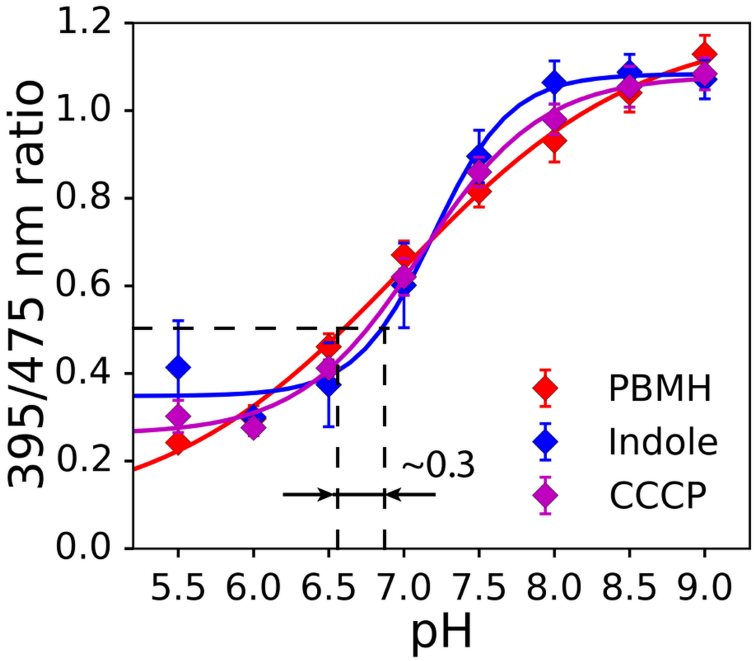

FIGURE 4.9: Calibration of pHluorin using different pH collapsing agents. The calibration performed in vitro with the purified protein is given in black. Figure from (Krasnopeeva, 2018)

for by the introduction of a parameter (Yaginuma et al., 2014). A comparison between the values read using QUEEN and another ATP estimation method, such as a population assay based on colorimetry, could potentially make my ATP estimations, which are given below (Fig. 4.10), more robust.

I also examined the role that the environmental pH has on the PMF of carbon starved cells, as this is a factor of ΔpH. I showed that for the range of external pH examined, with 6.7 and 8.2 at the extremes, the contribution of ΔpH varies linearly between -35 and 15mV respectively. As expected, acidic conditions are correlated with higher contributions to the PMF by the pH gradient. Despite such 50mV variation, the PMF is maintained within seemingly stable values. This perhaps suggests that in the absence of a carbon source, cells can only manage to reach a certain PMF level and that, depending on the environment, they can use different strategies to achieve it. It is however worth making some considerations. The exact conversion factor between BFM speed and PMF in mV is unknown for the load imposed by the size of the polystyrene bead I used. However, my measurements on EK07 cells grown to steady state with a growth rate of 0.74 hours^{-1} show that BFM speed averages 225 Hz. The PMF of fully energised *E. coli* is by some considered to be around

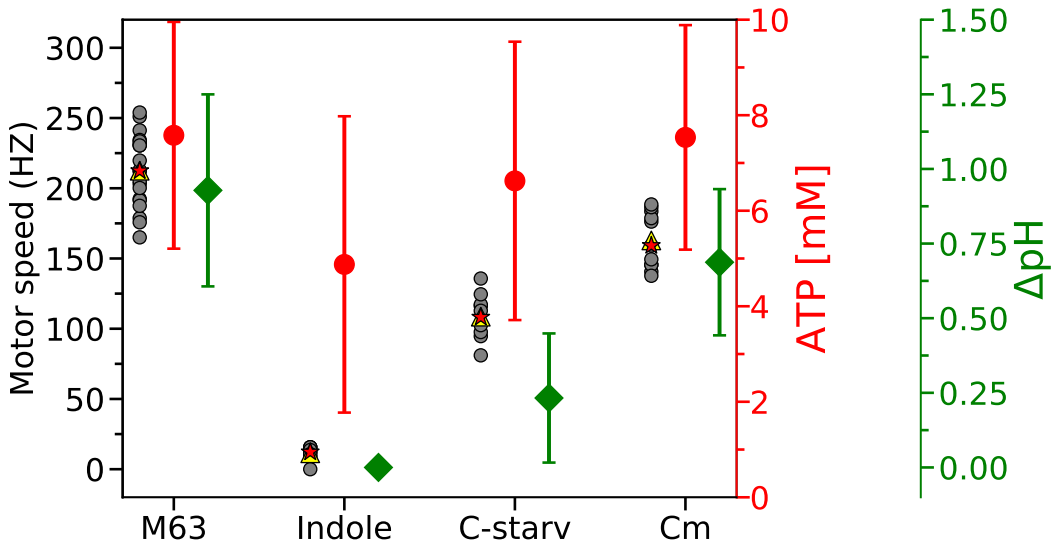

FIGURE 4.10: Energy parameters of dormant cells compared to growing ones. The figure is the same of Fig. 4.4D but the ratios from QUEEN7μ* have been converted to ATP concentrations according to the calibration curve in Fig. 3.15. The ΔpH value obtained after indole treatment is also converted to 0 as per assumption. Statistical significance of the differences in the energy parameters observed between dormant and growing cells were assayed via Student's t-test. All of the parameters of the various dormant conditions measured resulted significantly different from the ones of the growing cells with p-values at least below 10^{-6}. The only exception was the ATP concentration of cells treated with chloramphenicol which resulted not significantly different from that of growing cells.

-150mV (Gabel et al., 2003a), and although this may be a crude estimate, it is sufficient to postulate that the conversion factor may be not too far from 1. The ΔpH values measured are therefore likely to represent small contributions to the BFM speed, which are potentially masked by cell-to-cell variability. While the ΔpH is estimated from a larger sample of cells, PMF values are only measured from three to five cells per condition. Further experiments are needed to ascertain whether under carbon starvation conditions, cells achieve the same V_m but different ΔpHs or whether V_m and ΔpHs vary with opposite trends to make up the same PMF values. Another potential way of answering this question would be by measuring membrane voltage, but as discussed in chapter 2, reliable tools are lacking.

At the end of the chapter I discussed other factors that could in principle affect the energetics of the dormant state such as the life history of the cell. In particular, fluctuating environments are likely to induce accumulation of storage molecules which might fuel the cell during dormancy. Cells grown in different stable environments may also enter into dormancy with different energy levels because of their different metabolic adaptations. While assaying this second hypothesis, I discovered that although the growth rate increases when nutrient quality does, the PMF shows a threshold-like behavior once growth rate values of 0.7 hours^{-1} are reached, although the threshold point may in principle be anywhere between 0.33 and 0.7 hours^{-1}. This piece of evidence opens up to a series of suggestive hypotheses that will be discussed in detail in the *Future work* section of the last chapter.

As a final remark, the controls performed to ascertain that cells maintain a smaller ΔpH upon carbon starvation open an interesting avenue for estimating the conversion value between PMF in mV and BFM speed in Hz. Indeed, in Fig. 4.7 I showed that it is possible to selectively collapse membrane voltage and ΔpH by using PBMH and valinomycin together with a high concentration of potassium. Because: a) it is possible to measure ΔpH and b) its relationship with PMF in mV is known, it is in principle possible to estimate the conversion factor by first collapsing membrane voltage and then simultaneously measuring ΔpH and the remaining BFM speed.

Chapter 5

Dynamics of antibiotic accumulation and susceptibility

5.1 Introduction

The effectiveness of an antibiotic depends on the number of essential molecular targets it manages to reach and neutralise. Resistant, tolerant or persistent bacteria can adopt several different strategies to limit the damage caused by antimicrobials (Blair et al., 2014).

For example, increasing the number of copies of a protein that performs a task provides a buffer against molecules that interfere with it. The abundance of a certain molecular target depends on gene expression (the target production rate), dilution rate due to growth and turnover rate (Klumpp et al., 2009). Gene expression in bacteria is regulated by a plethora of signalling and control molecules that are produced or suppressed in response to environmental stimuli (Bervoets et al., 2019). The environment however does not only influence gene expression via the controlled means of regulation, but also through more indirect mechanisms. Many of the parameters that concur in gene expression, such as the transcription rate and gene dosage, are physiology dependent (Hintsche et al., 2013) and have a correlation with the growth rate (Klumpp et al., 2009). Thus, any unspecific environmental or internal cue that influences growth rate can in principle condition gene expression and antibiotic target abundance.

In some cases instead, it is easier to simply learn to do without the targeted protein. The importance of a certain cellular product depends on the conditions of both inner and outer environment. For example, the lactose permease, a sugar importer, becomes essential when lactose is the only carbon source in

the medium but mutants that lost the protein can grow normally on glucose substrates. Likewise, the cell division machinery is essential to growing cells, but its functions are limited in dormant, non-growing ones. Therefore, environmental conditions and physiological state do not only influence antibiotic survival because of target abundance but also because they can shift target essentiality (Tuomanen et al., 1986). Cell products that are only essential in a certain set of conditions are known as conditionally essential.

Another possibility is trying to limit the concentration of antibiotics that reach the targets. Bacteria can achieve this in various ways. Motile ones for example, can swim away from an array of noxious substances they are capable to sense, which are known as chemorepellents (Adler, 1975). Others can secrete enzymes that break down antibiotics, as in the case of the enzyme β-lactamase in ampicillin resistance (Bush, 2018). Sometimes it is not possible to alter antibiotic concentration in the environment. In such cases, one first line of defence is offered by the bacterial envelope, which varies in complexity and composition depending on species and strain. Gram-negative bacteria for example, perhaps only second to mycobateria, have particularly complex cell envelopes that act like permeability barriers and that make them, at least to a certain extent, intrinsically resistant to antibiotics. Even organisms with complex cell envelopes are not closed systems and need to exchange energy and matter with the environment to stay alive. This is achieved through channels such as porins, that constitute small gaps in their defensive system, or through pumps that selectively import molecules from the cellular milieu. Antibiotics that can treat these bacteria are capable of hijacking such structures and accumulate in the cytoplasm. Cells can however respond by expressing less channels or by altering their architectures to make them more selective against antimicrobials. These structural changes are commonly inheritable and are not limited to the cell's permeability barrier, but can concern the antibiotic target as well, making it unrecognisable, a form of adaptation often found in resistant strains (Blair et al., 2014). Another way of reducing drug concentration in the cytoplasm and perhaps the most obvious, is to actively pump it out. As discussed in chapter 2, bacteria have a plethora of pumps with these capabilities, which represent a major concern for their propensity to recognise and export a vast array of antimicrobials (Anes et al., 2015). Interestingly some evidence shows that even dormant cells, which, as discussed previously, many people assume low in energy, use these energy costly pumps to stay alive (Pu et al., 2016).

The accumulation of an antibiotic in the cell determines its efficacy, understanding the countermeasures that bacteria can adopt and their mechanisms is thus important to design appropriate treatments. If a cell is actively exporting a drug from its cytoplasm for example, reducing the energy available to the pumps to function or challenging the pumps with additional substrate species may be sufficient to increase antimicrobial efficacy. Likewise, knowing an antibiotic mechanism of permeation of the cell envelope has potential in improving drug design. This information is however difficult to obtain experimentally. I thus wondered whether, known the molecular target of an antibiotic, it could be possible to infer the accumulation mechanism of a drug in a cell by the survival rate of the population. Because survival depends on the physiological conditions of the cell, this could help devising more efficient treatment strategies. In this chapter I evaluate this preliminary hypothesis via mathematical modelling.

5.2 Contribution by other authors

Chua Chong Kean contributed to the work presented in this chapter by reviewing the literature on antibiotic influx and efflux mechanisms and on the dependency of volume on growth during his undergraduate dissertation project (honours project) that he carried out under my supervision.

5.3 Materials and methods

Computational work was carried out in Python using the odeint method of the Integrate subpackage of Scipy (Jones et al., 2001). Values for growth rate dependent parameters are obtained from the empirical measurements collected from previous literature by (Klumpp et al., 2009). They are reported in Table 5.1.

Parameter	Value at μ				
μ	0.6	1	1.5	2	2.5
a_m	0.65	1	1.31	1.49	1.5
a_p	0.97	1	0.94	0.94	0.90
g	1.55	1.82	2.28	2.86	3.56
β_m	0.53	0.50	0.48	0.45	0.43
β_p	6.9	11.5	17.3	23.1	28.9

TABLE 5.1: Empirical values reported by (Klumpp et al., 2009).

5.4 Results

The flux of antibiotic across the membrane has been recognised in previous theoretical work as an important factor to estimate its concentration in the cytoplasm. (**Greulich2015**) for example, define the rate of change of antibiotic concentration in the cytoplasm as:

$$\frac{da}{dt} = -\mu a + f(r_u, r_b, a) + J(a_{ex}, a) \tag{5.1}$$

where a_{ex} and a are the concentrations of antibiotic in the medium and in the cytoplasm, μa is the dilution rate due to cell growth, $f(r_u, r_b, a)$ is the binding of antibiotic to its target and $J(a_{ex}, a)$ describes antibiotic flux across the membrane. This latter is central in defining antibiotic efficacy and can vary significantly among different species and conditions. In this work, as done by others before (Nichols, 2017), the bacterial envelope is considered as a single barrier separating cellular cytoplasm from the medium. Differently than what proposed by (Nichols, 2017), the barrier is here modeled as completely impermeable to the drugs and decorated by 3 types of proteins that allow movement of chemicals: channels which, like porins, permit the non-selective bidirectional movement of antibiotics (inward and outward) with a certain diffusion coefficient D, import pumps, that transport the antibiotics from the cellular milieu to the cytoplasm, and export pumps that do the opposite. Cells are assumed to be in low enough density such that any accumulation of antibiotic in the cytoplasm is negligible for the concentration in the medium.

The dynamics of pumping mechanisms are poorly understood in bacteria, while active influx is scarcely documented. Beside the complex and still not completely clarified membrane voltage dependent uptake of aminoglycosides (Taber et al., 1987), the antibiotics albomycin and rifamycin CGP 4832 (a chemical relative to the more popular rifampicin) are actively imported through FhuA, an active transporter of siderophores (iron-chelating compounds) in *E. coli* (Braun et al., 2001). Despite their large number, the transport dynamics of efflux pumps (Anes et al., 2015), which have been often mentioned throughout this work, are also poorly understood. At this stage therefore, both the inward and outward active pumping mechanisms have been modeled in a Michaelis-Menten form as one possible example. Other kinds of transport mechanisms, including those specifically dependent on V_m or PMF, could be implemented

at a later stage. Cells are here assumed to always express the three protein species. Permeation through porins is always assumed and the drugs can be substrate of import pumps, export pumps, both or neither. Protein expression has a dependency on growth rate. In the model I take into account three types of gene expression: constitutive expression, that does not involve any regulation, activation, that implies the presence of a growth dependent activator protein, and repression, that encompasses a growth dependent inhibitor of expression (Klumpp et al., 2009). They are here represented according to the work done by (Klumpp et al., 2009), such that the number of channels and pumps depends on its expression regulation and on the physiological state of the cell represented by the growth rate. In accordance to (Klumpp et al., 2009) the dependence of a membrane protein P on the growth rate upon constitutive expression is as follow:

$$\frac{dP}{dt} = a_m a_p g/(\beta_m V) - \beta_p P \tag{5.2}$$

Where a_m, a_p, g, $_m$, V and $_p$ are growth rate dependent parameters which are based on empirical results and describe respectively: transcription rate per gene, translation rate, gene copy number, inverse of the mRNA lifetime, cell volume and protein dilution rate.

E. coli's volume is approximated to that of a spherocylinder (Buda et al., 2016) where length (l) and width (w) are dependent on the growth rate μ and are given by:

$$l = \alpha \cdot 2^{\beta\mu} \tag{5.3}$$

$$w = \beta \cdot 2^{\gamma\mu} \tag{5.4}$$

where α, β and γ are fitting parameters with values: 2.08, 0.41 and 0.36 respectively, as in (Taheri-Araghi et al., 2015). Volume is thus:

$$V = \frac{4}{3}\pi(\frac{w}{2})^3 + \pi(\frac{w}{2})^2 l \tag{5.5}$$

The growth dependent parameters can then be grouped together in $F(\mu)$ which is normalised to the value at μ = 1 and P_1 is the protein concentration at μ = 1:

$$\frac{dP}{dt} = P_1 F(\mu) - P \tag{5.6}$$

In the case of repression:

$$\frac{dP}{dt} = \frac{e_1}{(r_1/K)^n} F(\mu)^{-n+1} \tag{5.7}$$

where e_1 and r_1 represent the concentrations of the regulated protein and of the repressor, respectively, when $\mu = 1$. n describes the cooperativity of repression and K the repression scale, or the concentration of the repressor at which the expression is half-maximal (Klumpp et al., 2009).

In the case of positively regulated protein expression, $F(\mu)$ includes the growth rate dependent terms but takes two different indexes for the regulated protein and the activator because the two genes can be at different positions on the chromosome or on a plasmid (which would affect gene copy number). Similar to the case of repression, e_1 and a_1 are the concentrations of positively regulated protein and activator, respectively, when $\mu = 1$.

$$\frac{dP}{dt} = e_1 F_e(\mu) A(a_1 F_a(\mu)/K) \tag{5.8}$$

where A and K are part of the activation function:

$$A(a/K) = \frac{\frac{1}{f} + (a/K)^n}{1 + (a/K)^n} \tag{5.9}$$

and f is the fold-change of activation (Klumpp et al., 2009).

Where no active transport is involved, influx and efflux only depend on diffusion through the porin-like channels such that:

$$J(a_{ex}, a) = sP_p(\mu)D\frac{a_{ex} - a}{x} \tag{5.10}$$

where $P_p(\mu)$ is the number of channels (i.e. porins) through which the antibiotic can cross the membrane, s is the surface area of one channel, D is the diffusion coefficient through the channels and x is the membrane thickness (Buda

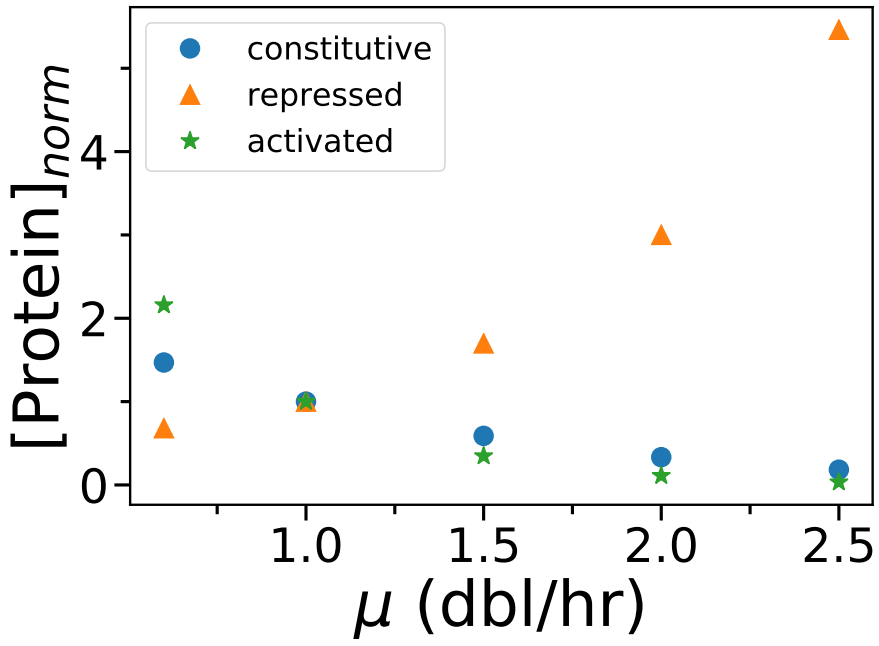

FIGURE 5.1: Protein expression as a function of growth rate in the 3 expression systems analysed: constitutive expression, repression, activation. The values are normalised for $f(\mu)$ where $\mu = 1$. Reproduced from (Klumpp et al., 2009).

et al., 2016).

The active transport of the antibiotic is described with a Michaelis-Menten form:

$$J(a_{ex}, a) = P(\mu)\frac{\gamma a}{k\gamma + a} \tag{5.11}$$

$P_i(\mu)$ and $P_e(\mu)$ are the pumps concentrations for influx and efflux. According to (1) and (2), in the case of active export, (2) becomes:

$$J(a_{ex}, a) = sP_p(\mu)D\frac{a_{ex} - a}{x} - P_e(\mu)\frac{\gamma_e a}{k_e\gamma_e + a} \tag{5.12}$$

while the case in which drugs are only substrate of active export pumps is given by:

$$J(a_{ex}, a) = sP_p(\mu)D\frac{a_{ex} - a}{x} + P_i(\mu)\frac{\gamma_i a_{ex}}{k_i\gamma_i + a_{ex}} \tag{5.13}$$

Lastly, the case in which drugs can cross the cellular envelope through the three protein species is given by:

$$J(a_{ex}, a) = sP_p(\mu)D\frac{a_{ex} - a}{x} + P_i(\mu)\frac{\gamma_i a_{ex}}{k_i\gamma_i + a_{ex}} - P_e(\mu)\frac{\gamma_e a}{k_e\gamma_e + a} \tag{5.14}$$

The computational experiment is carried out by adding a certain concentration of antibiotic in the medium and letting the cytoplasmic concentration a reach steady state. Cells at t_0 are in balanced growth at different growth rates. The model encompasses three protein species regulating drug concentration and three possible expression regulation strategies. In the main text I examine three limit cases in which all the proteins are simultaneously expressed either constitutively, with repression or with activation. The cytoplasmic concentrations of antibiotic at steady state for different growth rates in the other permutations are given in the *Appendix*. As shown in Fig. 5.2, in the three regulation cases examined, the model predicts significantly different antibiotic accumulation. As discussed in the introduction, together with antibiotic target abundance, antibiotic accruement defines bacterial survival rate. Thus, these results suggest that even with little prior knowledge, it may be possible to infer the mechanisms underlying antibiotic accumulation from the cells' survival rate.

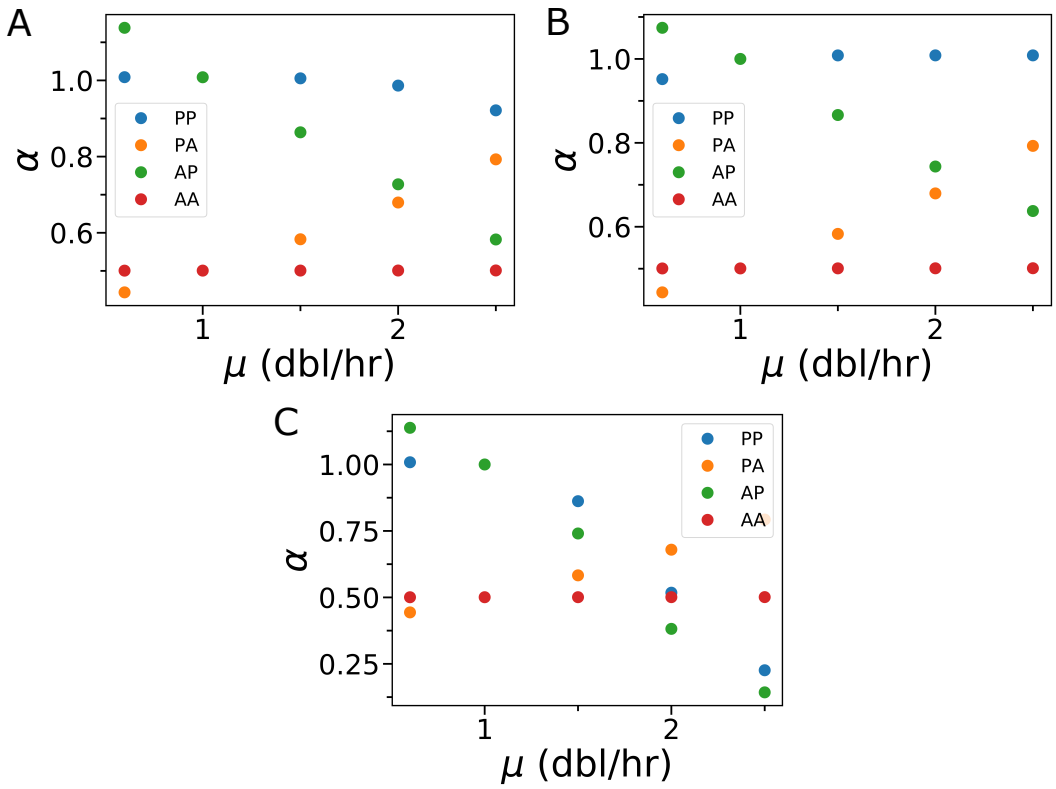

FIGURE 5.2: Cytoplasmic antibiotic concentration at equilibrium for the 3 limit cases examined with regards of protein expression and the 4 mechanisms: PP passive influx and passive efflux, AP = active influx and passive efflux, PA = passive influx and active efflux and AA = active influx and active efflux. a) All of the membrane proteins are expressed constitutively. b) The expression of all of the membrane proteins is repressed. c) The expression of all of the membrane proteins is activated.

Further than the value at equilibrium, I wondered whether the dynamics by which this equilibrium is reached could distinguish different mechanisms. Indeed the model shows that depending on the protein species the drug is a substrate of, cytoplasmic antibiotic concentration reaches steady state with different dynamics (Fig. 5.3, 5.4 and 5.5).

5.4.1 All of the protein species are expressed constitutively

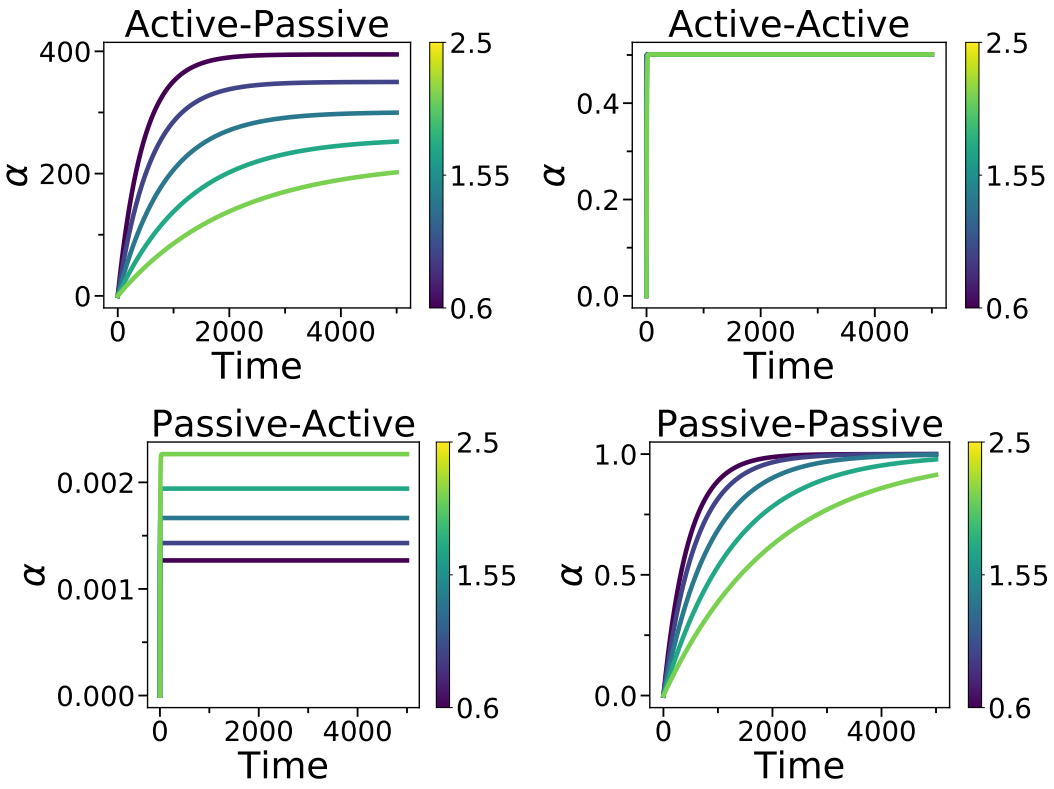

FIGURE 5.3: Cytoplasmic antibiotic accumulation according to the 4 mechanisms. The number of pumps is regulated constitutively. The colourmap indicates the growth rate.

5.4.2 The expression of all of the protein species is repressed

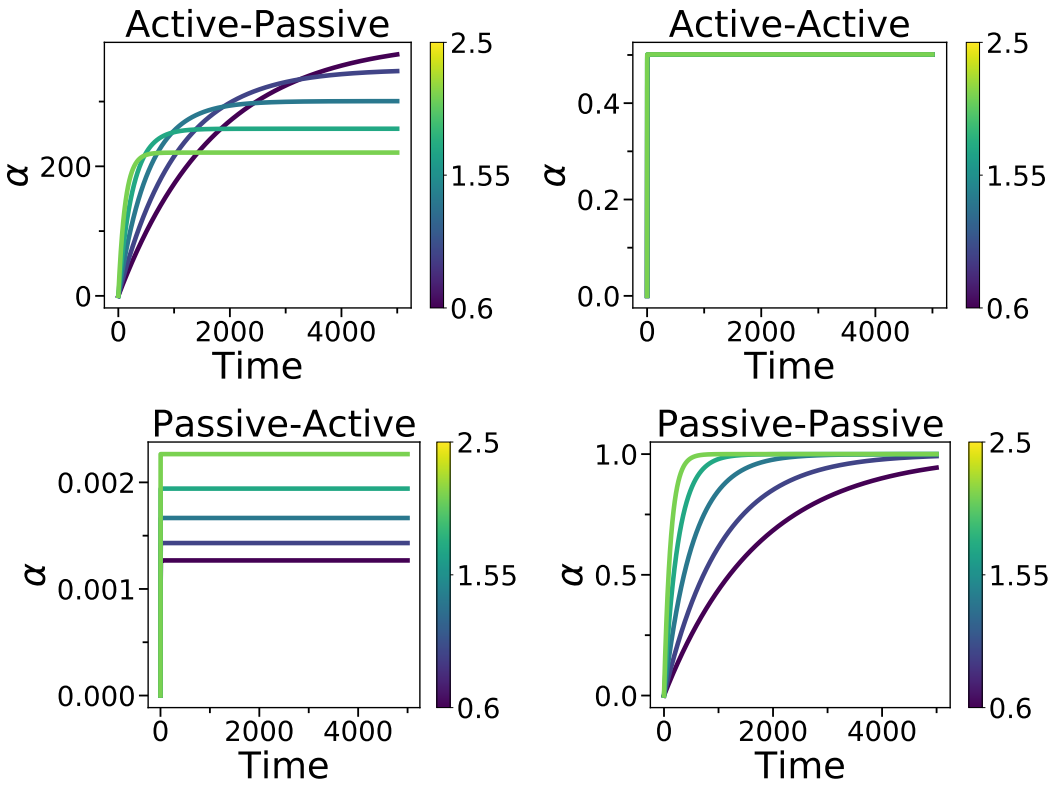

FIGURE 5.4: Cytoplasmic antibiotic accumulation according to the 4 mechanisms. The number of pumps is negatively regulated. The colourmap indicates the growth rate.

5.4.3 The expression of all of the protein species is activated

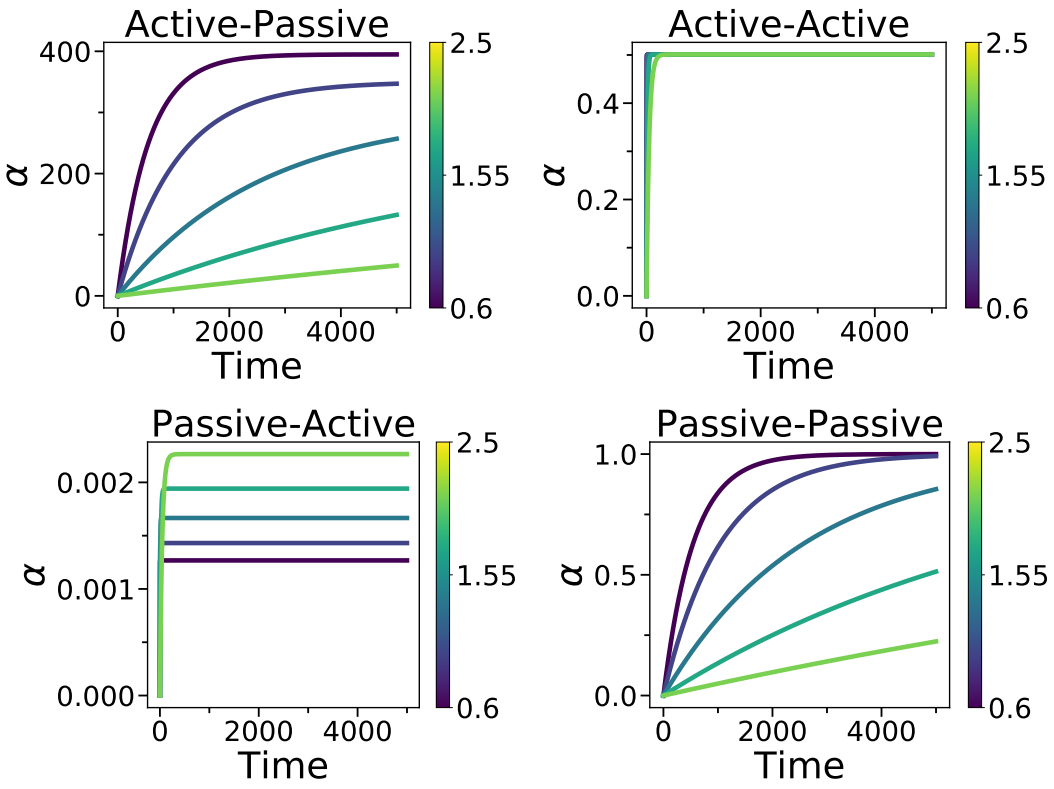

FIGURE 5.5: Cytoplasmic antibiotic accumulation according to the 4 mechanisms. The number of pumps is positively regulated. The colourmap indicates the growth rate.

5.5 Discussion

In this chapter I proposed the idea of a mathematical model that would describe antibiotic accumulation in the cytoplasm depending on its influx and efflux rates and on the physiological state of the cell. In the model, drug dynamics are governed by three protein species: a non-selective porin-like channel, a selective influx pump and a selective efflux pump.

I showed that depending on whether the drug is substrate of influx and efflux pumps, cytoplasmic accumulation reaches significantly different values and with characteristic dynamics. The existence of these signature traits suggests that it may be possible to map the cytoplasmic concentration to a specific accumulation mechanism even for uncharacterised drugs, a kind of information that would help drug discovery and infection treatment strategies. However, to distinguish between the different mechanisms, it is necessary to know drug intracellular concentration, whose experimental estimation is non-trivial.

Different cytoplasmic concentrations of antimicrobials likely have different effects on cell survival rate, an experimental parameter by far more accessible than antibiotic concentration. Cell survival rate depends on antibiotic abundance, targets abundance and on the minimum number of targets needed for life. All of these parameters have a certain dependence on the cell's physiological state. While I have shown that cellular physiology can easily be implemented in antibiotic fluxes when its role in protein expression is considered, in this work I did not model antibiotic target availability and its link with cell survival. However, relevant antibiotic targets such as the ribosome have been extensively studied and modeled mathematically with respect to the physiology of the cell (Scott et al., 2010; Scott et al., 2014) and their role in its survival (Greulich et al., 2017). In the future, merging my model of antibiotic fluxes with the work of others that focused on drug targets, such as those mentioned, will enable me to make predictions concerning survival rates. This will not only render the model experimentally testable, but will also help me characterise drug accumulation mechanisms. Non-resistant antimicrobial survivors enact strategies to keep the ratio between uptaken drugs and their targets low enough and thus the model has the potential to provide interesting insights on some of the mechanisms of drug tolerance.

Chapter 6

Conclusions and future work

6.1 Conclusions

Dormancy evolved several times in the history of life as an energy-saving, stress-avoiding mechanism. Bacteria enter in such a state in response to external and internal stimuli acquiring remarkable survival capabilities. Of particular relevance from a clinical point of view, dormancy confers these organisms the capability to withstand antibiotic challenges. Bacteria are known for being capable of evolving mechanisms allowing growth at relatively high concentrations of antibiotics, a phenomenon referred to as resistance. Dormant bacteria instead, die off to the same concentrations that regularly kill susceptible growing ones. What divides them from these latter is their capability to tolerate the drugs for long time. Many antibiotics used nowadays in clinical settings indeed, interfere with processes that are vital to growing cells, such as cell wall synthesis or DNA replication. Dormant cells are less susceptible to these drugs, because they make less use of the processes they target, a phenomenon known as conditional essentiality. There are several possible explanations to why most of our antibiotics are tuned for fast growing cells. One of the hypotheses might be connected to the evolution of microbial interactions. Most of the modern antibiotic classes indeed derive from substances that organisms evolved to gain the upper hand in a certain environmental niche. Examples are penicillin, produced by fungi of the genus *Penicillium* and streptomycin, produced by *Streptomyces griseus*. Thinking that, in these habitats, the complete eradication of a competitor through antibiotics might not be necessary, has its logical coherence. Indeed, the gain of a simple fitness advantage is often enough to outnumber a rival species. Or perhaps, it might have to do with the methods we use to screen for antimicrobials, that often, at least in their

initial stages, rely on the presence or absence of growth, as this is arguably the easiest proxy for susceptibility. A treatment that eradicates dormant cells but that is poorly effective against growing cells is very likely to pass under the radar of these screens. Focusing on proliferating cells is of course important, as it is cell proliferation that practically allows infections to progress. Indeed, keeping pathogen number in check is often enough to ensure their clearance by the immune system. However, recent findings demonstrate that tolerant cells are not only a health risk for a subset of the population that is not immunocompetent, but that they pave the way to antibiotic resistance (Levin-Reisman et al., 2017), which concerns both individuals with healthy and compromised immune systems. In the light of the incumbent antibiotic resistance crisis it is therefore necessary to develop strategies to eradicate dormant cells from infection sites. To this end better knowledge of the mechanisms that allow dormant cells to maintain viability is needed, as this will allow us to tune our drug discovery experiments against the most effective targets and design appropriate treatments.

Cells that exhausted their nutrient source stop growing and enter into a stationary phase, which is characterised by a constant cell number resulting from the fact that the birth rate matches the death rate. In this condition most of the cells stop growing entering a dormant state and acquiring antibiotic tolerant capabilities. Because these cells have exhausted their external energy sources and because of the natural link borrowed from superior animals between dormancy and energy-saving, the first idea of a difference between dormant cells and growing cells that comes to mind is their energetic state. Research carried out on the quantification of ATP concentration in dormant cells produced contrasting evidence, perhaps suggesting that dormancy, at least from an energy perspective, may not be univocal. In this work I proposed and examined this interpretation developing tools to test it at the single cell level.

To have a broader view of the energetics of dormant cells I focused on ATP and on PMF, the main players in the chemiosmotic theory, and on the two components of the second: the proton gradient across the plasma membrane and the membrane voltage.

In chapter 2, I reviewed the current methodologies for assaying V_m in bacteria, finding in cationic nernstian probes the ideal candidate for carrying out absolute estimations. Motivated by the complexity of the biological context in which these molecules are used, I first explored the parametrical landscape

that governs the tradeoffs behind the use of these charged substances, using mathematical modelling and in collaboration with other colleagues. I showed that the time needed for these molecules to reach nernstian equilibrium is independent from the concentration of the probes but not from the membrane voltage. I then showed how, by virtue of these predictions, it is possible to design a simple experimental algorithm to characterise the effects of cationic nernstian probes on cell physiology. I demonstrated the procedure on the recently proposed nernstian dye Thioflavin T, failing to find suitable conditions for its use in *E. coli*. I also demonstrated the array of effects the dyes can have on bacterial physiology and how these could easily lead to misinterpretation of the membrane voltage readings. Due to the different experimental conditions and bacterial species used, a direct comparison between my results and those previously obtained with the same membrane voltage dye in *B. subtilis* is not possible. Due to its generality and simplicity however, the workflow is in the position to offer a rapid mean to assay the reliability of previous works and the robustness of future findings.

In chapter 3, I examined the state of the art of single cell ATP measurements, individuating two potentially interesting sensors in the literature: Perceval, which reports ATP to ADP ratio, and QUEEN, which is susceptible to ATP concentration. I attempted their constitutive expression downstream the cytochrome C oxidase from *V. Harveij*. While Perceval showed a non-uniform pattern of expression across the cell population, perhaps indicating some level of toxicity, the QUEEN sensor, although very dimly, was expressed by all the cells. For logistical reasons I decided to not dedicate further time to the optimization of the expression of Perceval, but to focus on QUEEN. During these initial expression attempts I noticed that removing the histidine tag from the QUEEN sensor yielded a significant increase in fluorescence, particularly for the sensor variant called QUEEN7μ. Together with the implementation of a laser at 488nm in my lab's custom build microscope setup, this allowed me to reduce the exposure time necessary for imaging the probe by one and a half orders of magnitude. I showed that in my conditions the QUEEN7μ sensor, deprived of the his tag, which I renamed QUEEN7μ*, could sense in the mM range, which is the expected physiological range of *E. coli*. Having access to time series imaging of the sensor due to the enhanced signal intensity, I assayed its response to illumination, finding it prone to both photobleaching and photoactivation. While the first can be characterised and corrected for, I

demonstrated that the appearance of the second can be condition-dependent. My results suggest that the safest treatment of photoeffects is to bypass them altogether by restricting measurements to single events. To the best of my knowledge, the QUEEN* sensor developed in this work is the only available method that enables ATP quantification at the single cell level in physiological conditions in bacteria, which, considered the central role of ATP in biology, opens up to the possibility of addressing an array of research questions.

The methods developed in the previous chapters were used in association to others in the literature to measure energy parameters during bacterial dormancy in chapter 4. Having first established a definition of dormancy that lied on simple axioms such as viability and growth halt, I pinpointed three different conditions capable of inducing dormancy in *E. coli*: starvation, quorum sensing and treatment with bacteriostatic drugs. I elicited starvation by suddenly removing the carbon source from the medium. Differently from stationary phase, in my experimental setup, live cells cannot feed on the debris of the dead ones, because the media in the flow chamber is continuously replenished. As an example of quorum sensing molecule I chose indole while I used chloramphenicol as a bacteriostatic drug. Combining the sensors QUEEN and pHluorin and the bacterial flagellar motor speed, I examined ATP concentration, ΔpH and PMF of dormant cells. While calibrating pHluorin against different pHs I showed that the relationship between its fluorescence and pH has a slight temperature dependence. I showed that indole induces a very energy-poor dormancy, sharply collapsing PMF, in agreement with previous reports suggesting that indole at mM concentrations acts as a ionophore. The changes induced by chloramphenicol are instead much more gradual, with only a slight decrease in PMF over 30 minutes of treatment, coherent with previous reports. In contrast, ATP concentration remained stable, which is in contradiction with the same reports. I then showed that carbon starvation induces a dormancy also characterised by a sharp drop in PMF. Both the electrochemical potential of protons and ATP concentration settled on values that were roughly half than the initial ones. Finally, I showed that the pH of the carbon starvation medium was affecting the composition of the PMF. Taken together these results demonstrated that the dormant state is not univocally energy-poor, but that its energetics are strongly dependent on the environmental conditions. This on one hand offers an explanation for the contrasting results obtained in different labs regarding ATP concentration in subpopulations of antibiotic

tolerant dormant cells, on the other hand suggests that to fight infection recalcitrance due to growth halted cells it might be necessary to develop different treatments according to the conditions present at the infection site. Taken together, the results presented in this chapter offer a novel view of dormancy and of its physiology, knowledge that is in the position to help the design of more efficient treatments.

6.2 Future work

6.2.1 Effect of cellular life history on the energetics of dormancy

In this work I demonstrated with single cell tools that dormancy-inducing conditions can yield significantly different energetic states upon growth arrest. However, it is likely that also the physiological state of the cell at the moment of the entrance into dormancy may play a role. In particular, two factors may be worth of consideration: energy storage and metabolic adaptations. Bacteria, particularly in stressful conditions or in the presence of stress anticipating conditions such as those characteristic of fluctuating environments, can accumulate several kinds of storage molecules. Some of them, such as polymeric lipids (Wältermann et al., 2005) and glycogen (Wang et al., 2011), can be used for long term survival, while others such as inorganic poly-P chains (Kornberg et al., 1999) and polyhydroxybutyrate (PHB) can supply energy on the short term (Wang et al., 2011). In the future it would be interesting to investigate the role of these forms of metabolic stress memory on survival during dormancy.

Energetic differences might also exist between dormant cells that had grown in different constant environments. Cellular composition, which in balanced growth depends on nutrient quality (Scott et al., 2010; Scott et al., 2014) and starting energy values may influence the physiological state of dormancy. Indeed in this work, obtaining some preliminary data regarding PMF, I demonstrated that for certain growth rates, nutrient quality has a direct effect on cellular energetics. It is possible that these differences may be to some extents maintained upon growth halt and may participate in determining the survival of the organisms to antimicrobial treatments.

6.2.2 Do energetically different dormancies condition susceptibility to antibiotic treatment and survival in general?

Another work that would be complimentary to the one presented here, involves testing whether the observed energetic differences play a role in survival. From the point of view of antibiotics, the involvement of energetics in some mechanisms capable of altering antibiotic efficacy is already demonstrated or at least expected. The classical case is the one of aminoglycoside antibiotics, the entrance of which in the cell is by many thought to be dependent on PMF and particularly membrane voltage (Davis, 1987) and by some on ATP too (Fraimow et al., 1991). The mechanism is still not completely clear, although the leading hypothesis is the one of a self-promoted uptake (Hancock et al., 1991). A case in which the involvement of energy is instead expected is the one of antibiotics that are substrate of multi-drug efflux pumps. These enzymes are indeed PMF or ATP dependent (Anes et al., 2015). It can therefore speculated that dormancies which are low in energy will be poorly susceptible to aminoglycosides. Conversely, highly energetic dormancies will probably be better suited for surviving antibiotic challenges from drugs that are substrate of efflux pumps such as β-lactams.

Survival over long periods of unfavourable conditions, whether these are a result of antibiotics or not, is not well understood. Tools such as those developed in this work can potentially help shed light on bacterial strategies of energy maintenance in example by helping establishing a definition of life and death from an energetic point of view. Understanding the energy cost of certain processes would be important in many aspects of cell biology and may also be highly informative for synthetic biology.

6.2.3 Calibration of BFM speed and PMF at different motor loads

Another potential future development of this work concerns the demonstration that using a combination of potassium and valinomycin, and PBMH it is possible to selectively collapse membrane voltage or ΔpH. While, as showed in this work and others (Krasnopeeva, 2018), it is possible to estimate the latter, tools that allow the estimation of the membrane voltage are lacking. Because of this, the exact relation between motor speed at a given load and PMF is not

known. The only available technique allowing the estimation of this factor is practically cumbersome as it requires the physical insertion of a filamentous *E. coli* cell expressing the motor into a narrow micropipette. Its effectiveness for precise estimations at high motor speeds is not demonstrated (Fung et al., 1995). However, by first collapsing the membrane voltage and then estimating the ΔpH it might in principle be possible to calibrate BFM speed against PMF at different loads. A precise estimation of the PMF would be useful for understanding the energetics dynamics underlying cell physiology.

6.2.4 *E. coli* energetics at slow growth rate

Another intriguing research direction may arise from the understanding that PMF and growth rate are not linearly correlated throughout the possible growth rates that *E. coli* can attain during balanced growth. Indeed, based on population extracts, the currently accepted notion is that ATP concentration is independent from the growth rate (Schneider et al., 2004). However, as evident

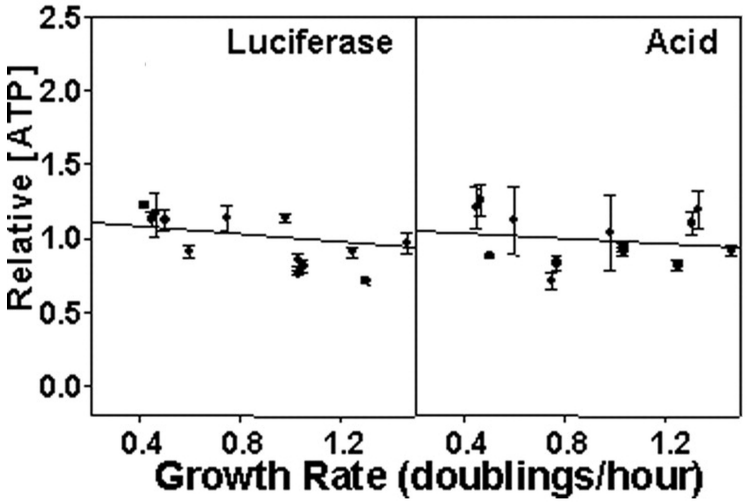

FIGURE 6.1: ATP concentration is independent from the growth rate as estimated by (Schneider et al., 2004) via luciferase and acid extraction assays. The figure has been adapted from (Schneider et al., 2004)

from Fig. (6.1), ATP concentration has only been estimated down to a doubling rate around 0.5 doublings/hour which corresponds to a growth rate of 0.35 hours^{-1}. According to my experiments this might still be in a region of the growth rate spectrum in which the PMF is relatively steady. Because in my dormant cells PMF and ATP quantities seem correlated, it may be possible

that like PMF, ATP concentration too may depend on growth rate when this is sufficiently low. This could potentially have repercussions on the current interpretation of the regulatory role that ATP concentration has in gene expression. Alternatively, it may suggest that cells maintain an energy-cap, which is an interesting concept per se. Instead, if ATP and PMF do not correlate at the slow growth rates, it may mean that a mechanism that couples PFM and ATP comes into play when one of the two is limited, as it happens during dormancy.

6.2.5 Can a simple mathematical model predict antibiotic accumulation mechanisms?

A further piece of future work concerns the continuation of Chapter 5, in which the idea of using a mathematical model encompassing antibiotic accumulation and target production rates to predict antibiotic accruement mechanism is put forward. The development of the idea may follow several possible paths. In example, the antibiotic fluxes modeled in Chapter 5 may be merged with other models encompassing the abundance of drug targets (Greulich et al., 2017; Scott et al., 2010; Scott et al., 2014). Knowledge of drug and targets abundance, together with that of the cellular need of these latter for survival, has the potential to yield predictions that are relatively easy to test experimentally in terms of drug mechanisms. One way to test whether the predictions of the model make sense, would be to use β-lactam antibiotics because they are known for entering in the cell via diffusion and for being substrate of drug efflux pumps (Lim et al., 2010). Another interesting path of development for the work discussed in Chapter 5, would be to use it to better understand antibiotic survival. Active drug import and export are indeed energy dependent. Using the model in association with the single cell tools developed and demonstrated in this work, it may be possible, in example, to postulate that cells with little energy are more susceptible to -lactams because they accumulate more drug as they do not have enough fuel for the efflux pumps.

Appendix A

Appendix

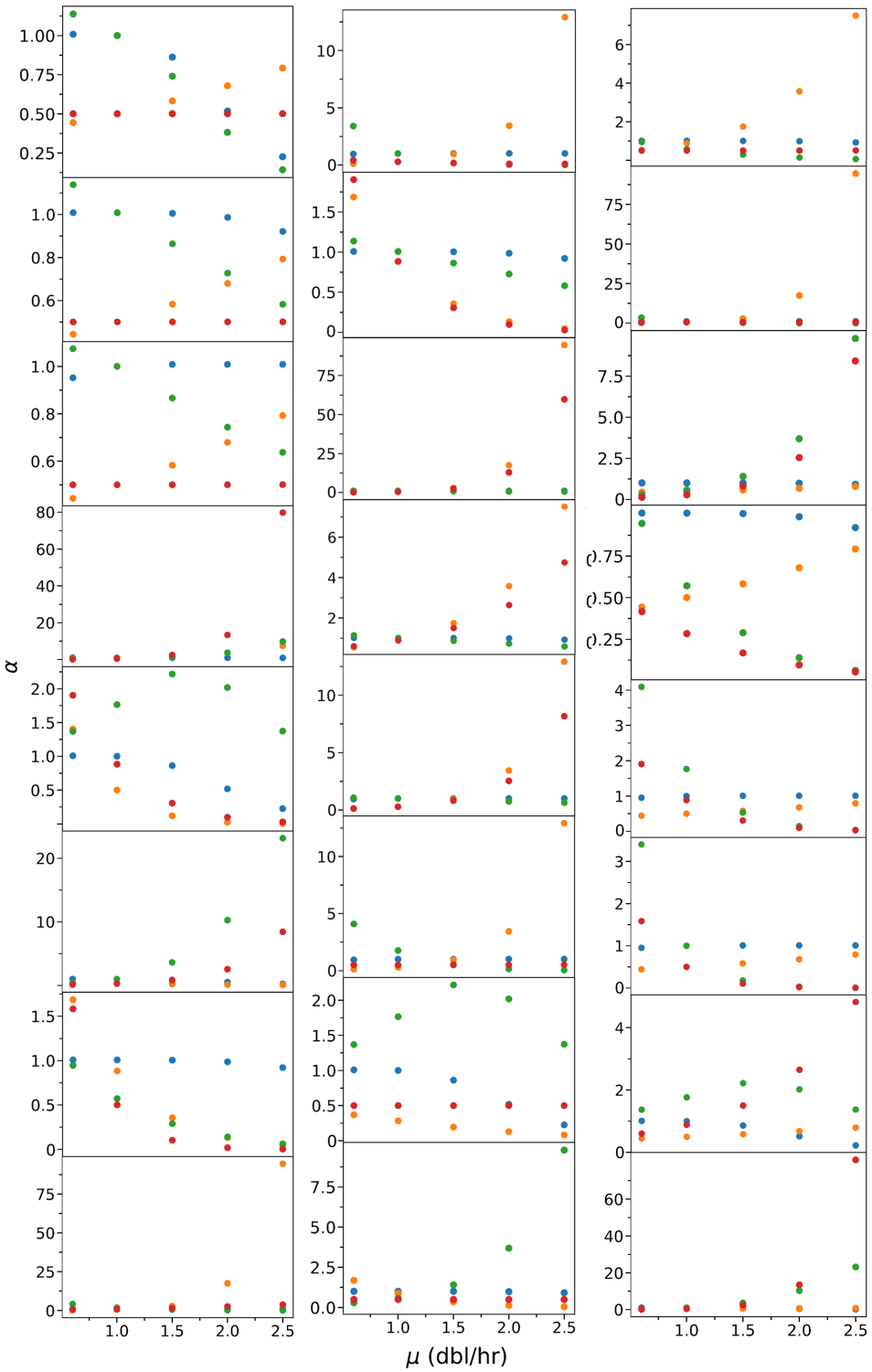

FIGURE A.1: Possible permutations of the constitutive, repressed or activated expression of the porins (P), influx pumps (I) and efflux pumps (E) as indicated in Table A.2

Study	Claim	Induction	Estimation
Shan et al., 2017	*E. coli* MG1655 low in ATP has higher persister frequency	10mM arsenate	a
Conlon et al., 2016	*S. aureus* persisters have low ATP	1,5,10mM Arsenate	a
Cameron et al., 2018	*P. aeruginosa* Δ*carB* accumulates ATP and is more susceptible than the WT treated with 5mM arsenate	Δ*carB* or 5mM arsenate	a
Leszczynska et al., 2013	No correlation between *E. coli* at 37°C in LB medium supplemented with MC4100 persisters and ATP levels	Various media, stationary phase	a
Braetz et al., 2017	*S. Typhimurium* persists if treated with arsenate, *S. Typhimurium* Δ*atp* does not	0.25mM arsenate or ΔATP	a
Svenningsen et al., 2019	Low ATP in *E. coli* MG1655 does not induce persisters	Temperature sensitive tRNA synthesis	b

TABLE A.1: The literature offers contrasting evidence concerning ATP abundance in persisters. a = Promega BacTiter Glo Kit, b = QUEEN 7μ

Const	Repr	Activ
/	/	P,I,E
P,I,E	/	/
/	P,I,E	/
P	I	E
I	E	P
E	I	P
P	E	I
I	P	E

Const	Repr	Activ
E	P	I
P,I	E	/
/	PI	E
PI	/	E
E	PI	/
EI	P	/
EI	/	P
P	EI	/

Const	Repr	Activ
P	/	EI
/	P	EI
EP	I	/
EP	/	I
I	EP	/
/	EP	I
I	/	EP
/	I	EP

TABLE A.2: Scheme of expression of the porins (P), influx pumps (I) and efflux pumps (E) showed in Fig. A.1.

Bibliography

Aakre, Christopher D. et al. (2013). "A Bacterial Toxin Inhibits DNA Replication Elongation through a Direct Interaction with the Sliding Clamp". In: *Molecular Cell* 52.5, pp. 617 –628. ISSN: 1097-2765. DOI: https://doi.org/10.1016/j.molcel.2013.10.014.

Ackermann, Martin (2015). "A functional perspective on phenotypic heterogeneity in microorganisms". In: *Nature Reviews Microbiology* 13, 497 EP –.

Adams, Dany S. and Michael Levin (2012). "Measuring resting membrane potential using the fluorescent voltage reporters DiBAC4(3) and CC2-DMPE". In: *Cold Spring Harbor protocols* 2012.4, pp. 459–464. ISSN: 1559-6095. DOI: 10.1101/pdb.prot067702.

Adler, J (1975). "Chemotaxis in Bacteria". In: *Annual Review of Biochemistry* 44.1, pp. 341–356. DOI: 10.1146/annurev.bi.44.070175.002013.

Ahmed, S. and I. R. Booth (1983). "The use of valinomycin, nigericin and trichlorocarbanilide in control of the protonmotive force in Escherichia coli cells". In: *The Biochemical journal* 212.1, pp. 105–112. ISSN: 0264-6021. DOI: 10.1042/bj2120105.

Alberty, Robert A. (1968). "Effect of pH and Metal Ion Concentration on the Equilibrium Hydrolysis of Adenosine Triphosphate to Adenosine Diphosphate". In: *Journal of Biological Chemistry* 243.7, pp. 1337–1343.

Allison, Kyle R., Mark P. Brynildsen, and James J. Collins (2011). "Metabolite-enabled eradication of bacterial persisters by aminoglycosides". In: *Nature* 473.7346, pp. 216–220. ISSN: 1476-4687. DOI: 10.1038/nature10069.

Alvarez-Ortega, Carolina, Jorge Olivares, and José L. Martínez (2013). "RND multidrug efflux pumps: what are they good for?" In: *Front Microbiol* 4, pp. 7–7. ISSN: 1664-302X. DOI: 10.3389/fmicb.2013.00007. URL: https://www.ncbi.nlm.nih.gov/pubmed/23386844.

Amini, Sasan et al. (2011). "Fitness Landscape of Antibiotic Tolerance in Pseudomonas aeruginosa Biofilms". In: *PLOS Pathogens* 7.10, pp. 1–13. DOI: 10.1371/journal.ppat.1002298.

Anes, João et al. (2015). "The ins and outs of RND efflux pumps in Escherichia coli". In: *Front Microbiol* 6, pp. 587–587. ISSN: 1664-302X. DOI: 10.3389/fmicb.2015.00587.

Arkin, Isaiah T. et al. (2007a). "Mechanism of Na+/H+ Antiporting". In: *Science* 317.5839, pp. 799–803. ISSN: 0036-8075. DOI: 10.1126/science.1142824.

— (2007b). "Mechanism of Na+/H+ Antiporting". In: *Science* 317.5839, pp. 799–803. ISSN: 0036-8075. DOI: 10.1126/science.1142824. eprint: https://science.sciencemag.org/content/317/5839/799.full.pdf. URL: https://science.sciencemag.org/content/317/5839/799.

Baba, Tomoya et al. (2006). "Construction of Escherichia coli K-12 in-frame, single-gene knockout mutants: the Keio collection". In: *Molecular Systems Biology* 2.1. ISSN: 1744-4292. DOI: 10.1038/msb4100050. eprint: http://msb.embopress.org/content/2/1/2006.0008.full.pdf. URL: http://msb.embopress.org/content/2/1/2006.0008.

Bai, Fan et al. (2010). "Conformational Spread as a Mechanism for Cooperativity in the Bacterial Flagellar Switch". In: *Science* 327.5966, pp. 685–689. ISSN: 0036-8075. DOI: 10.1126/science.1182105. eprint: http://science.sciencemag.org/content/327/5966/685.full.pdf. URL: http://science.sciencemag.org/content/327/5966/685.

Bai, Wei, K.S. Zhao, and K. Asami (2006). "Dielectric properties of E. coli cell as simulated by the three-shell spheroidal model". In: *Biophysical Chemistry* 122.2, pp. 136 –142. ISSN: 0301-4622. DOI: https://doi.org/10.1016/j.bpc.2006.03.004. URL: http://www.sciencedirect.com/science/article/pii/S0301462206000767.

Balaban, Nathalie Q. et al. (2004). "Bacterial Persistence as a Phenotypic Switch". In: *Science* 305.5690, pp. 1622–1625. ISSN: 0036-8075. DOI: 10.1126/science.1099390.

Balaban, Nathalie Q. et al. (2019). "Definitions and guidelines for research on antibiotic persistence". In: *Nature Reviews Microbiology* 17.7, pp. 441–448. ISSN: 1740-1534. DOI: 10.1038/s41579-019-0196-3.

Ballmoos, Christoph von, Alexander Wiedenmann, and Peter Dimroth (2009). "Essentials for ATP Synthesis by F1F0 ATP Synthases". In: *Annual Review of Biochemistry* 78.1, pp. 649–672. DOI: 10.1146/annurev.biochem.78.081307.104803.

Basan, Markus et al. (2015). "Overflow metabolism in Escherichia coli results from efficient proteome allocation". In: *Nature* 528.7580, pp. 99–104. ISSN: 1476-4687. DOI: 10.1038/nature15765.

Bay, Denice C., Kenton L. Rommens, and Raymond J. Turner (2008). "Small multidrug resistance proteins: A multidrug transporter family that continues to grow". In: *Biochimica et Biophysica Acta (BBA) - Biomembranes* 1778.9, pp. 1814 –1838. ISSN: 0005-2736. DOI: https://doi.org/10.1016/j.bbamem.2007.08.015. URL: http://www.sciencedirect.com/science/article/pii/S000527360700301X.

Berg, J. M., J. L. Tymoczko, and L. Stryer (2002a). *Biochemistry. 5th edition.* New York: W H Freeman.

Berg, Jim, Yin Pun Hung, and Gary Yellen (2009). "A genetically encoded fluorescent reporter of ATP:ADP ratio". In: *Nature methods* 6.2, pp. 161–166. ISSN: 1548-7105. DOI: 10.1038/nmeth.1288.

Berg, JM, JL Tymoczko, and L Stryer (2002b). *Biochemistry. 5th edition. Section 9.4.2: Magnesium (or Manganese) Complexes of Nucleoside Triphosphates Are the True Substrates for Essentially All NTP-Dependent Enzymes*. New York: W H Freeman.

Bergmiller, Tobias et al. (2017). "Biased partitioning of the multidrug efflux pump AcrAB-TolC underlies long-lived phenotypic heterogeneity". In: *Science* 356.6335, pp. 311–315. ISSN: 0036-8075. DOI: 10.1126/science.aaf4762.

Bernstein, J. (1868). "Ueber den zeitlichen Verlauf der negativen Schwankung des Nervenstroms". In: *Archiv für die gesamte Physiologie des Menschen und der Tiere* 1.1, pp. 173–207. ISSN: 1432-2013. DOI: 10.1007/BF01640316. URL: https://doi.org/10.1007/BF01640316.

Bervoets, Indra and Daniel Charlier (2019). "Diversity, versatility and complexity of bacterial gene regulation mechanisms: opportunities and drawbacks for applications in synthetic biology". In: *FEMS Microbiology Reviews* 43.3, pp. 304–339. ISSN: 0168-6445. DOI: 10.1093/femsre/fuz001.

Blair, Jessica M. A. et al. (2014). "Molecular mechanisms of antibiotic resistance". In: *Nature Reviews Microbiology* 13, 42 EP –.

Bloch, Konrad (1996). "Some biochemical thoughts on the RNA world". In: *Chemistry Biology* 3.5, pp. 405 –407. ISSN: 1074-5521. DOI: https://doi.org/10.1016/S1074-5521(96)90123-4.

Blondeau, Joseph M. (2004). "Fluoroquinolones: mechanism of action, classification, and development of resistance". In: *Survey of Ophthalmology* 49.2, Supplement 2, S73 –S78. ISSN: 0039-6257. DOI: https://doi.org/10.1016/j.survophthal.2004.01.005.

Bokranz, M., E. Mörschel, and A. Kröger (1985). "Phosphorylation and phosphate-ATP exchange catalyzed by the ATP synthase isolated from Wolinella succinogenes". In: *Biochimica et Biophysica Acta (BBA) - Bioenergetics* 810.3, pp. 332 –339. ISSN: 0005-2728. DOI: https://doi.org/10.1016/0005-2728(85)90218-X.

Bowers, Keith C, Ashley P Allshire, and Peter H Cobbold (1992). "Bioluminescent measurement in single cardiomyocytes of sudden cytosolic ATP depletion coincident with rigor". In: *Journal of Molecular and Cellular Cardiology* 24.3, pp. 213 –218. ISSN: 0022-2828. DOI: https://doi.org/10.1016/0022-2828(92)93159-H.

Bradbeer, C (1993). "The proton motive force drives the outer membrane transport of cobalamin in *Escherichia coli*." In: *Journal of bacteriology* 175.10, pp. 3146–50. ISSN: 0021-9193. URL: http://www.pubmedcentral.nih.gov/articlerender.fcgi?artid=204637{\&}tool=pmcentrez{\&}rendertype=abstract.

Braetz, Sebastian et al. (2017). "The role of ATP pools in persister cell formation in (fluoro)quinolone-susceptible and -resistant strains of Salmonella enterica ser. Typhimurium". In: *Veterinary Microbiology* 210, pp. 116 –123. ISSN: 0378-1135. DOI: https://doi.org/10.1016/j.vetmic.2017.09.007.

Braun, Volkmar et al. (2001). "Outer Membrane Channels and Active Transporters for the Uptake of Antibiotics". In: *The Journal of Infectious Diseases* 183.Supplement$_1$, S12–S16. ISSN: 0022-1899. DOI: 10.1086/318840.

Brauner, Asher et al. (2016). "Distinguishing between resistance, tolerance and persistence to antibiotic treatment". In: *Nature Reviews Microbiology* 14, 320 EP –.

Bremer H, Dennis P (2008). "Modulation of Chemical Composition and Other Parameters of the Cell at Different Exponential Growth Rates". In: *EcoSal Plus*.

Buda, Renata et al. (2016). "Dynamics of Escherichia coli's passive response to a sudden decrease in external osmolarity". In: *Proceedings of the National*

Academy of Sciences 113.40, E5838–E5846. ISSN: 0027-8424. DOI: 10.1073/pnas.1522185113.

Bush, Karen (2018). "Past and Present Perspectives on -Lactamases". In: *Antimicrobial Agents and Chemotherapy* 62.10. ISSN: 0066-4804. DOI: 10.1128/AAC.01076-18.

Butt, H.J. et al. (2003). *Physics and Chemistry of Interfaces*. Physics textbook. Wiley. ISBN: 9783527404131. URL: https://books.google.es/books?id=r-IpcdGJMJEC.

Cabiscol, Elisa, Jordi Tamarit, and Joaquim Ros (2000). "Oxidative stress in bacteria and protein damage by reactive oxygen species". In: *International microbiology : the official journal of the Spanish Society for Microbiology* 3, pp. 3–8.

Cameron, David R. et al. (2018). "A Genetic Determinant of Persister Cell Formation in Bacterial Pathogens". In: *Journal of bacteriology* 200.17, e00303–18. ISSN: 1098-5530. DOI: 10.1128/JB.00303-18.

Capaldi, Roderick A. and Robert Aggeler (2002). "Mechanism of the F₁F<sub>
type ATP synthase, a biological rotary motor". In: *Trends in Biochemical Sciences* 27.3, pp. 154–160. ISSN: 0968-0004. DOI: 10.1016/S0968-0004(01)02051-5.

Cars, Otto et al. (2008). "Meeting the challenge of antibiotic resistance". In: *BMJ* 337. ISSN: 0959-8138. DOI: 10.1136/bmj.a1438.

Chowdhury, Nityananda, Brian W. Kwan, and Thomas K. Wood (2016). "Persistence Increases in the Absence of the Alarmone Guanosine Tetraphosphate by Reducing Cell Growth". In: *Scientific Reports* 6, 20519 EP –.

Conlon, Brian P. et al. (2016). "Persister formation in Staphylococcus aureus is associated with ATP depletion". In: *Nature microbiology* 1, p. 16051. ISSN: 2058-5276. DOI: 10.1038/nmicrobiol.2016.51.

Costa, P F et al. (1989). "Determination of ionic permeability coefficients of the plasma membrane of Xenopus laevis oocytes under voltage clamp." In: *The Journal of Physiology* 413.1, pp. 199–211. DOI: 10.1113/jphysiol.1989.sp017649. eprint: https://physoc.onlinelibrary.wiley.com/doi/pdf/10.1113/jphysiol.1989.sp017649. URL: https://physoc.onlinelibrary.wiley.com/doi/abs/10.1113/jphysiol.1989.sp017649.

Datsenko, Kirill A. and Barry L. Wanner (2000). "One-step inactivation of chromosomal genes in Escherichia coli K-12 using PCR products". In: *Proceedings of the National Academy of Sciences* 97.12, pp. 6640–6645. ISSN: 0027-8424. DOI: 10.1073/pnas.120163297. eprint: http://www.pnas.org/content/97/12/6640.full.pdf. URL: http://www.pnas.org/content/97/12/6640.

Davis, B. D. (1987). "Mechanism of bactericidal action of aminoglycosides". In: *Microbiological reviews* 51.3, pp. 341–350. ISSN: 0146-0749.

Del Castillo, J. and B. Katz (1954). "Quantal components of the end-plate potential". In: *J Physiol* 124.3, pp. 560–573. ISSN: 0022-3751. URL: https://www.ncbi.nlm.nih.gov/pubmed/13175199.

Dhamdhere, Girija and Helen I. Zgurskaya (2010). "Metabolic shutdown in Escherichia coli cells lacking the outer membrane channel TolC". In: *Molecular microbiology* 77.3, pp. 743–754. ISSN: 1365-2958. DOI: 10.1111/j.1365-2958.2010.07245.x. URL: https://www.ncbi.nlm.nih.gov/pubmed/20545840.

Di Tomaso, Giovanna, Roberto Borghese, and Davide Zannoni (2001). "Assay of ATP in intact cells of the facultative phototroph Rhodobacter capsulatus expressing recombinant firefly luciferase". In: *Archives of Microbiology* 177.1, pp. 11–19. ISSN: 1432-072X. DOI: 10.1007/s00203-001-0352-8.

Dong, Jiantong and Meiping Zhao (2016). "In-vivo fluorescence imaging of adenosine 5-triphosphate". In: *TrAC Trends in Analytical Chemistry* 80, pp. 190–203. ISSN: 0165-9936. DOI: https://doi.org/10.1016/j.trac.2016.03.020.

Drawz, Sarah M. and Robert A. Bonomo (2010). "Three Decades of -Lactamase Inhibitors". In: *Clinical Microbiology Reviews* 23.1, pp. 160–201. ISSN: 0893-8512. DOI: 10.1128/CMR.00037-09.

Dudev, Todor, Cédric Grauffel, and Carmay Lim (2017). "How Native and Alien Metal Cations Bind ATP: Implications for Lithium as a Therapeutic Agent". In: *Scientific Reports* 7, 42377 EP –.

Ehrenberg, B. et al. (1988). "Membrane potential can be determined in individual cells from the nernstian distribution of cationic dyes". In: *Biophysical journal* 53.5, pp. 785–794. ISSN: 0006-3495. DOI: 10.1016/S0006-3495(88)83158-8. URL: https://www.ncbi.nlm.nih.gov/pubmed/3390520.

Elowitz, Michael B et al. (1997). "Photoactivation turns green fluorescent protein red". In: *Current Biology* 7.10, pp. 809 –812. ISSN: 0960-9822. DOI: https://doi.org/10.1016/S0960-9822(06)00342-3.

Elowitz, Michael B. et al. (2002). "Stochastic Gene Expression in a Single Cell". In: *Science* 297.5584, pp. 1183–1186. ISSN: 0036-8075. DOI: 10.1126/science.1070919.

Felle, H. et al. (1980). "Quantitative measurements of membrane potential in Escherichia coli". In: *Biochemistry* 19.15, pp. 3585–3590. DOI: 10.1021/bi00556a026.

Fleming, Alexander (1929). "On the Antibacterial Action of Cultures of a Penicillium, with Special Reference to their Use in the Isolation of B. influenzæ". In: *British journal of experimental pathology* 10.3, pp. 226–236. ISSN: 0007-1021.

Fluhler, Eric, Valerie G. Burnham, and Leslie M. Loew (1985). "Spectra, membrane binding, and potentiometric responses of new charge shift probes". In: *Biochemistry* 24.21, pp. 5749–5755. ISSN: 0006-2960. DOI: 10.1021/bi00342a010.

Fraimow, H. S. et al. (1991). "Tobramycin uptake in Escherichia coli is driven by either electrical potential or ATP". In: *Journal of bacteriology* 173.9, pp. 2800–2808. ISSN: 0021-9193. DOI: 10.1128/jb.173.9.2800-2808.1991.

Franzen, James S. and S. B. Binkley (1961). "Comparison of the Acid-soluble Nucleotides in Escherichia coli at Different Growth Rates". In: *Journal of Biological Chemistry* 236.2, pp. 515–519.

Frey, Perry A. and Abolfazl Arabshahi (1995). "Standard Free Energy Change for the Hydrolysis of the α,β-Phosphoanhydride Bridge in ATP". In: *Biochemistry* 34.36, pp. 11307–11310. DOI: 10.1021/bi00036a001.

Fridman, Ofer et al. (2014). "Optimization of lag time underlies antibiotic tolerance in evolved bacterial populations". In: *Nature* 513, 418 EP –.

Fung, David C. and Howard C. Berg (1995). "Powering the flagellar motor of Escherichia coli with an external voltage source". In: *Nature* 375.6534, pp. 809–812. ISSN: 1476-4687. DOI: 10.1038/375809a0.

Gaal, Tamas et al. (1997). "Transcription Regulation by Initiating NTP Concentration: rRNA Synthesis in Bacteria". In: *Science* 278.5346, pp. 2092–2097. ISSN: 0036-8075. DOI: 10.1126/science.278.5346.2092.

Gabel, Christopher V. and Howard C. Berg (2003a). "The speed of the flagellar rotary motor of Escherichia coli varies linearly with protonmotive force". In: *Proceedings of the National Academy of Sciences* 100.15, pp. 8748–8751. ISSN: 0027-8424. DOI: 10.1073/pnas.1533395100.

Gabel, Christopher V. and Howard C. Berg (2003b). "The speed of the flagellar rotary motor of Escherichia coli varies linearly with protonmotive force". In: *Proceedings of the National Academy of Sciences* 100.15, pp. 8748–8751. ISSN: 0027-8424. DOI: 10.1073/pnas.1533395100. eprint: http://www.pnas.org/content/100/15/8748.full.pdf. URL: http://www.pnas.org/content/100/15/8748.

Garlid, Keith D., Andrew D. Beavis, and Signe K. Ratkje (1989). "On the nature of ion leaks in energy-transducing membranes". In: *Biochimica et Biophysica Acta (BBA) - Bioenergetics* 976.2, pp. 109 –120. ISSN: 0005-2728. DOI: https://doi.org/10.1016/S0005-2728(89)80219-1. URL: http://www.sciencedirect.com/science/article/pii/S0005272889802191.

Garlid, Keith D and Petr Paucek (2003). "Mitochondrial potassium transport: the K+ cycle". In: *Biochimica et Biophysica Acta (BBA) - Bioenergetics* 1606.1, pp. 23 –41. ISSN: 0005-2728. DOI: https://doi.org/10.1016/S0005-2728(03)00108-7. URL: http://www.sciencedirect.com/science/article/pii/S0005272803001087.

Gefen, Orit et al. (2008). "Single-cell protein induction dynamics reveals a period of vulnerability to antibiotics in persister bacteria". In: *Proceedings of the National Academy of Sciences* 105.16, pp. 6145–6149. ISSN: 0027-8424. DOI: 10.1073/pnas.0711712105.

Geiser, Fritz (2011). "Hibernation: Endotherms". In: *eLS*. American Cancer Society. ISBN: 9780470015902. DOI: 10.1002/9780470015902.a0003215.pub2.

Gerdes, K., P. B. Rasmussen, and S. Molin (1986). "Unique type of plasmid maintenance function: postsegregational killing of plasmid-free cells". In: *Proceedings of the National Academy of Sciences of the United States of America* 83.10, pp. 3116–3120. ISSN: 0027-8424. DOI: 10.1073/pnas.83.10.3116.

Gerdes, Kenn (2000). "Toxin-Antitoxin Modules May Regulate Synthesis of Macromolecules during Nutritional Stress". In: *Journal of Bacteriology* 182.3, pp. 561–572. ISSN: 0021-9193. DOI: 10.1128/JB.182.3.561-572.2000.

Germain, Elsa et al. (2015). "Stochastic induction of persister cells by HipA through (p)ppGpp-mediated activation of mRNA endonucleases". In: *Proceedings of the National Academy of Sciences* 112.16, pp. 5171–5176. ISSN: 0027-8424. DOI: 10.1073/pnas.1423536112.

Goldman, David E. (1943). "POTENTIAL, IMPEDANCE, AND RECTIFICATION IN MEMBRANES". In: *The Journal of General Physiology* 27.1, pp. 37–

60. ISSN: 0022-1295. DOI: 10.1085/jgp.27.1.37. eprint: http://jgp.rupress.org/content/27/1/37.pdf. URL: http://jgp.rupress.org/content/27/1/37.

Goormaghtigh, Frédéric et al. (2018). "Reassessing the Role of Type II Toxin-Antitoxin Systems in Formation of Escherichia coli Type II Persister Cells". In: *mBio* 9.3. Ed. by Gisela Storz. DOI: 10.1128/mBio.00640-18.

Grabe, Michael and George Oster (2001). "Regulation of Organelle Acidity". In: *The Journal of General Physiology* 117.4, pp. 329–344. ISSN: 0022-1295. DOI: 10.1085/jgp.117.4.329. eprint: http://jgp.rupress.org/content/117/4/329.full.pdf. URL: http://jgp.rupress.org/content/117/4/329.

Graef, M. R. de et al. (1999). "The steady-state internal redox state (NADH/NAD) reflects the external redox state and is correlated with catabolic adaptation in Escherichia coli". In: *Journal of bacteriology* 181.8, pp. 2351–2357. ISSN: 0021-9193.

Graham, Jay P., John J. Boland, and Ellen Silbergeld (2007). "Growth promoting antibiotics in food animal production: an economic analysis". In: *Public health reports (Washington, D.C. : 1974)* 122.1, pp. 79–87. ISSN: 0033-3549. DOI: 10.1177/003335490712200111.

Greulich, Philip et al. (2017). "Predicting the dynamics of bacterial growth inhibition by ribosome-targeting antibiotics". English. In: *Physical Biology* 14.6. ISSN: 1478-3967. DOI: 10.1088/1478-3975/aa8001.

Hall, James E., C. A. Mead, and Gabor Szabo (1973). "A barrier model for current flow in lipid bilayer membranes". In: *The Journal of Membrane Biology* 11.1, pp. 75–97. ISSN: 1432-1424. DOI: 10.1007/BF01869814. URL: https://doi.org/10.1007/BF01869814.

Han, Junyan and Kevin Burgess (2010). "Fluorescent Indicators for Intracellular pH". In: *Chemical Reviews* 110.5, pp. 2709–2728. ISSN: 0009-2665. DOI: 10.1021/cr900249z.

Hancock, R. E. et al. (1991). "Interaction of aminoglycosides with the outer membranes and purified lipopolysaccharide and OmpF porin of Escherichia coli". In: *Antimicrobial agents and chemotherapy* 35.7, pp. 1309–1314. ISSN: 0066-4804. DOI: 10.1128/aac.35.7.1309.

Harms, Alexander et al. (2017). "Prophages and Growth Dynamics Confound Experimental Results with Antibiotic-Tolerant Persister Cells". In: *mBio* 8.6.

Ed. by Joerg Vogel, Sophie Helaine, and Richard Gourse. DOI: 10.1128/mBio.01964-17.

Helaine, Sophie et al. (2010). "Dynamics of intracellular bacterial replication at the single cell level". In: *Proceedings of the National Academy of Sciences* 107.8, pp. 3746–3751. ISSN: 0027-8424. DOI: 10.1073/pnas.1000041107.

Hintsche, Marius and Stefan Klumpp (2013). "Dilution and the theoretical description of growth-rate dependent gene expression". In: *Journal of Biological Engineering* 7.1, p. 22. ISSN: 1754-1611. DOI: 10.1186/1754-1611-7-22.

Hodgkin, A L and A F Huxley (1939). "Action Potentials Recorded from Inside a Nerve Fibre". In: *Nature* 144, p. 710.

Imamura, Hiromi et al. (2009). "Visualization of ATP levels inside single living cells with fluorescence resonance energy transfer-based genetically encoded indicators". In: *Proceedings of the National Academy of Sciences* 106.37, pp. 15651–15656. ISSN: 0027-8424. DOI: 10.1073/pnas.0904764106.

Jahreis, Knut et al. (2008). "Ins and outs of glucose transport systems in eubacteria". In: *FEMS Microbiology Reviews* 32.6, pp. 891–907. ISSN: 0168-6445. DOI: 10.1111/j.1574-6976.2008.00125.x. URL: http://dx.doi.org/10.1111/j.1574-6976.2008.00125.x.

Jensen, Kaj Frank, Ulf Houlberg, and Per Nygaard (1979). "Thin-layer chromatographic methods to isolate 32P-labeled 5-phosphoribosyl--1-pyrophosphate (PRPP): Determination of cellular PRPP pools and assay of PRPP synthetase activity". In: *Analytical Biochemistry* 98.2, pp. 254 –263. ISSN: 0003-2697. DOI: https://doi.org/10.1016/0003-2697(79)90138-6.

Jones, Eric, Travis Oliphant, Pearu Peterson, et al. (2001). *SciPy: Open source scientific tools for Python*. URL: http://www.scipy.org/.

Jones, Shari A. et al. (2008). "Glycogen and Maltose Utilization by Escherichia coli O157:H7 in the Mouse Intestine". In: *Infection and Immunity* 76.6, pp. 2531–2540. ISSN: 0019-9567. DOI: 10.1128/IAI.00096-08.

Jonge, R. de et al. (2003). "The adaptive response of Escherichia coli O157 in an environment with changing pH". In: *Journal of Applied Microbiology* 94.4, pp. 555–560. DOI: 10.1046/j.1365-2672.2003.01865.x.

Kashket, E R (1985). "The Proton Motive Force in Bacteria: A Critical Assessment of Methods". In: *Annual Review of Microbiology* 39.1, pp. 219–242. DOI: 10.1146/annurev.mi.39.100185.001251. eprint: https://doi.org/10.1146/annurev.mi.39.100185.001251. URL: https://doi.org/10.1146/annurev.mi.39.100185.001251.

Keener, J. and J. Sneyd (2009). "Mathematical Physiology". In: p. 93.

Kell, Douglas B. et al. (1998). "Viability and activity in readily culturable bacteria: a review and discussion of the practical issues". In: *Antonie van Leeuwenhoek* 73.2, pp. 169–187. ISSN: 1572-9699. DOI: 10.1023/A:1000664013047.

Kennedy, Helen J. et al. (1999). "Glucose Generates Sub-plasma Membrane ATP Microdomains in Single Islet -Cells: POTENTIAL ROLE FOR STRATEGICALLY LOCATED MITOCHONDRIA". In: *Journal of Biological Chemistry* 274.19, pp. 13281–13291. DOI: 10.1074/jbc.274.19.13281.

Kim, Jong-Ho et al. (2010). "A Luciferase/Single-Walled Carbon Nanotube Conjugate for Near-Infrared Fluorescent Detection of Cellular ATP". In: *Angewandte Chemie International Edition* 49.8, pp. 1456–1459. DOI: 10.1002/anie.200906251.

Kim, Jun-Seob and Thomas K. Wood (2016). "Persistent Persister Misperceptions". In: *Frontiers in Microbiology* 7, p. 2134. ISSN: 1664-302X. DOI: 10.3389/fmicb.2016.02134.

Kim, Minsu et al. (2012). "Need-based activation of ammonium uptake in Escherichia coli". In: *Molecular Systems Biology* 8.1, p. 616. DOI: 10.1038/msb.2012.46.

Klumpp, Stefan, Zhongge Zhang, and Terence Hwa (2009). "Growth rate-dependent global effects on gene expression in bacteria". In: *Cell* 139.7, pp. 1366–1375. ISSN: 1097-4172.

Koop, A and P H Cobbold (1993). "Continuous bioluminescent monitoring of cytoplasmic ATP in single isolated rat hepatocytes during metabolic poisoning". In: *Biochemical Journal* 295.1, pp. 165–170. ISSN: 0264-6021. DOI: 10.1042/bj2950165.

Kornberg, Arthur, Narayana N. Rao, and Dana Ault-Riché (1999). "Inorganic Polyphosphate: A Molecule of Many Functions". In: *Annual Review of Biochemistry* 68.1, pp. 89–125. DOI: 10.1146/annurev.biochem.68.1.89.

Kralj, Joel M. et al. (2011). "Electrical Spiking in Escherichia coli Probed with a Fluorescent Voltage-Indicating Protein". In: *Science* 333.6040, pp. 345–348. ISSN: 0036-8075. DOI: 10.1126/science.1204763.

Krämer, Christina E. M., Wolfgang Wiechert, and Dietrich Kohlheyer (2016). "Time-resolved, single-cell analysis of induced and programmed cell death via non-invasive propidium iodide and counterstain perfusion". In: *Scientific Reports* 6, p. 32104. URL: https://doi.org/10.1038/srep32104.

Krasnopeeva, Ekaterina (2018). "Single cell measurements of bacterial physiology traits during exposure to an external stress". PhD thesis. University of Edinburgh.

Krasnopeeva, Ekaterina, Chien-Jung Lo, and Teuta Pilizota (2019). "Single-Cell Bacterial Electrophysiology Reveals Mechanisms of Stress-Induced Damage". In: *Biophysical Journal* 116.12, pp. 2390 –2399. ISSN: 0006-3495. DOI: https://doi.org/10.1016/j.bpj.2019.04.039.

Krebs, H. A. and W. A. Johnson (1937). "The role of citric acid in intermediate metabolism in animal tissues." In: *Enzymologia* 4, pp. 148–156.

Kuroda, Teruo and Tomofusa Tsuchiya (2009). "Multidrug efflux transporters in the MATE family". In: *Biochimica et Biophysica Acta (BBA) - Proteins and Proteomics* 1794.5, pp. 763 –768. ISSN: 1570-9639. DOI: https://doi.org/10.1016/j.bbapap.2008.11.012. URL: http://www.sciencedirect.com/science/article/pii/S1570963908003749.

Lee, Heewook et al. (2012). "Rate and molecular spectrum of spontaneous mutations in the bacterium Escherichia coli as determined by whole-genome sequencing". In: *Proceedings of the National Academy of Sciences* 109.41, E2774–E2783. ISSN: 0027-8424. DOI: 10.1073/pnas.1210309109.

Lee, Henry H. et al. (2010). "Bacterial charity work leads to population-wide resistance". In: *Nature* 467, 82 EP –.

Leszczynska, Daria et al. (2013). "The Formation of Persister Cells in Stationary-Phase Cultures of Escherichia Coli Is Associated with the Aggregation of Endogenous Proteins". In: *PLOS ONE* 8.1, pp. 1–10. DOI: 10.1371/journal.pone.0054737.

Levin-Reisman, Irit et al. (2017). "Antibiotic tolerance facilitates the evolution of resistance". In: *Science* 355.6327, pp. 826–830. ISSN: 0036-8075. DOI: 10.1126/science.aaj2191.

Lewis, Kim (2006). "Persister cells, dormancy and infectious disease". In: *Nature Reviews Microbiology* 5, 48 EP –.

Lim, Siew Ping and Hiroshi Nikaido (2010). "Kinetic parameters of efflux of penicillins by the multidrug efflux transporter AcrAB-TolC of Escherichia coli". In: *Antimicrobial agents and chemotherapy* 54.5, pp. 1800–1806. ISSN: 1098-6596. DOI: 10.1128/AAC.01714-09.

Lindner, Ariel B. et al. (2008). "Asymmetric segregation of protein aggregates is associated with cellular aging and rejuvenation". In: *Proceedings of the*

National Academy of Sciences 105.8, pp. 3076–3081. ISSN: 0027-8424. DOI: 10.1073/pnas.0708931105.

Ling, G. and R. W. Gerard (1949). "The normal membrane potential of frog sartorius fibers". In: *Journal of Cellular and Comparative Physiology* 34.3, pp. 383–396. ISSN: 0095-9898. DOI: 10.1002/jcp.1030340304.

Lipmann, Fritz (2006). "Metabolic Generation and Utilization of Phosphate Bond Energy". In: *Advances in Enzymology and Related Areas of Molecular Biology*. John Wiley Sons, Ltd, pp. 99–162. ISBN: 9780470122464. DOI: 10.1002/9780470122464.ch4.

Little, R. and H. Bremer (1982). "Quantitation of guanosine 5,3-bisdiphosphate in extracts from bacterial cells by ion-pair reverse-phase high-performance liquid chromatography". In: *Analytical Biochemistry* 126.2, pp. 381 –388. ISSN: 0003-2697. DOI: https://doi.org/10.1016/0003-2697(82)90531-0.

Lo, Chien-Jung et al. (2007a). "Nonequivalence of Membrane Voltage and Ion-Gradient as Driving Forces for the Bacterial Flagellar Motor at Low Load". In: *Biophysical Journal* 93.1, pp. 294–302. ISSN: 0006-3495. DOI: 10.1529/biophysj.106.095265.

— (2007b). "Nonequivalence of Membrane Voltage and Ion-Gradient as Driving Forces for the Bacterial Flagellar Motor at Low Load". In: *Biophysical Journal* 93.1, pp. 294 –302. ISSN: 0006-3495. DOI: https://doi.org/10.1529/biophysj.106.095265. URL: http://www.sciencedirect.com/science/article/pii/S0006349507712821.

Lobas, Mark A. et al. (2019). "A genetically encoded single-wavelength sensor for imaging cytosolic and cell surface ATP". In: *Nature Communications* 10.1, p. 711. ISSN: 2041-1723. DOI: 10.1038/s41467-019-08441-5.

Lobritz, Michael A. et al. (2015). "Antibiotic efficacy is linked to bacterial cellular respiration". In: *Proceedings of the National Academy of Sciences* 112.27, pp. 8173–8180. ISSN: 0027-8424. DOI: 10.1073/pnas.1509743112.

Lopez-Amoros, R, J Comas, and J Vives-Rego (1995). "Flow cytometric assessment of Escherichia coli and Salmonella typhimurium starvation-survival in seawater using rhodamine 123, propidium iodide, and oxonol." In: *Applied and Environmental Microbiology* 61.7, pp. 2521–2526. ISSN: 0099-2240. eprint: https://aem.asm.org/content/61/7/2521.full.pdf. URL: https://aem.asm.org/content/61/7/2521.

Lord, Nathan (2014). "Fluctuation timescales in bacterial gene expression". PhD thesis. Harvard University.

Loukin, Stephen H. et al. (2005). "Microbial K+ Channels". In: *The Journal of General Physiology* 125.6, pp. 521–527. ISSN: 0022-1295. DOI: 10.1085/jgp.200509261.

Lubelski, Jacek, Wil N. Konings, and Arnold J. M. Driessen (2007). "Distribution and physiology of ABC-type transporters contributing to multidrug resistance in bacteria". In: *Microbiol Mol Biol Rev* 71.3, pp. 463–476. ISSN: 1092-2172. DOI: 10.1128/MMBR.00001-07. URL: https://www.ncbi.nlm.nih.gov/pubmed/17804667.

Macara, Ian G. and Stavroula Mili (2008). "Polarity and Differential Inheritance—Universal Attributes of Life?" In: *Cell* 135.5, pp. 801 –812. ISSN: 0092-8674. DOI: https://doi.org/10.1016/j.cell.2008.11.006.

Magariyama, Y. et al. (1995). "Simultaneous measurement of bacterial flagellar rotation rate and swimming speed". In: *Biophysical Journal* 69.5, pp. 2154 –2162. ISSN: 0006-3495. DOI: https://doi.org/10.1016/S0006-3495(95)80089-5.

Magariyama, Yukio, Shigeru Sugiyama, and Seishi Kudo (2001). "Bacterial swimming speed and rotation rate of bundled flagella". In: *FEMS Microbiology Letters* 199.1, pp. 125–129. ISSN: 0378-1097. DOI: 10.1111/j.1574-6968.2001.tb10662.x.

Maisonneuve, Etienne et al. (2011). "Bacterial persistence by RNA endonucleases". In: *Proceedings of the National Academy of Sciences* 108.32, pp. 13206–13211. ISSN: 0027-8424. DOI: 10.1073/pnas.1100186108.

Maisonneuve, Etienne, Manuela Castro-Camargo, and Kenn Gerdes (2018). "Retraction Notice to: (p)ppGpp Controls Bacterial Persistence by Stochastic Induction of Toxin-Antitoxin Activity". In: *Cell* 172.5, p. 1135. ISSN: 0092-8674. DOI: 10.1016/j.cell.2018.02.023.

Mancini, Leonardo et al. (2020). "A General Workflow for Characterization of Nernstian Dyes and Their Effects on Bacterial Physiology". In: *Biophysical Journal* 118.1, pp. 4 –14. ISSN: 0006-3495. DOI: https://doi.org/10.1016/j.bpj.2019.10.030. URL: http://www.sciencedirect.com/science/article/pii/S0006349519308793.

Mandadapu, Kranthi K. et al. (2015). "Mechanics of torque generation in the bacterial flagellar motor". In: *Proceedings of the National Academy of Sciences* 112.32, E4381–E4389. ISSN: 0027-8424. DOI: 10.1073/pnas.1501734112.

Manno, Carlo et al. (2013). "Confocal imaging of transmembrane voltage by SEER of di-8-ANEPPS". In: *The Journal of General Physiology* 141.3, pp. 371–387. ISSN: 0022-1295. DOI: 10.1085/jgp.201210936.

Martinac, B et al. (1987). "Pressure-sensitive ion channel in Escherichia coli". In: *Proceedings of the National Academy of Sciences* 84.8, pp. 2297–2301. ISSN: 0027-8424. DOI: 10.1073/pnas.84.8.2297. eprint: http://www.pnas.org/content/84/8/2297.full.pdf. URL: http://www.pnas.org/content/84/8/2297.

Martinac, Boris et al. (2013). "Patch Clamp Electrophysiology for the Study of Bacterial Ion Channels in Giant Spheroplasts of E. coli". In: *Bacterial Cell Surfaces: Methods and Protocols*. Ed. by Anne H. Delcour. Totowa, NJ: Humana Press, pp. 367–380. ISBN: 978-1-62703-245-2. DOI: 10.1007/978-1-62703-245-2_23. URL: https://doi.org/10.1007/978-1-62703-245-2_23.

Martinez, Keith A. et al. (2012). "Cytoplasmic pH Response to Acid Stress in Individual Cells of Escherichia coli and Bacillus subtilis Observed by Fluorescence Ratio Imaging Microscopy". In: *Applied and Environmental Microbiology* 78.10, pp. 3706–3714. ISSN: 0099-2240. DOI: 10.1128/AEM.00354-12. eprint: https://aem.asm.org/content/78/10/3706.full.pdf. URL: https://aem.asm.org/content/78/10/3706.

Maruyama, Koscak (1991). "The discovery of adenosine triphosphate and the establishment of its structure". In: *Journal of the History of Biology* 24.1, pp. 145–154. ISSN: 1573-0387. DOI: 10.1007/BF00130477.

Maskevich, A. A. et al. (2015). "Spectral Manifestations of Thioflavin T Aggregation". In: *Journal of Applied Spectroscopy* 82.1, pp. 33–39. ISSN: 1573-8647. DOI: 10.1007/s10812-015-0060-9. URL: https://doi.org/10.1007/s10812-015-0060-9.

Maskevich, Alexander A. et al. (2007). "Spectral Properties of Thioflavin T in Solvents with Different Dielectric Properties and in a Fibril-Incorporated Form". In: *Journal of Proteome Research* 6.4, pp. 1392–1401. DOI: 10.1021/pr0605567. eprint: https://doi.org/10.1021/pr0605567. URL: https://doi.org/10.1021/pr0605567.

Matsuura, Shusuke, Jun ichi Shioi, and Yasuo Imae (1977). "Motility in Bacillus subtilis driven by an artificial protonmotive force". In: *FEBS Letters* 82.2, pp. 187 –190. ISSN: 0014-5793. DOI: https://doi.org/10.1016/

0014-5793(77)80581-4. URL: http://www.sciencedirect.com/science/article/pii/0014579377805814.

McDougald, Diane et al. (1998). "Nonculturability: adaptation or debilitation?" In: *FEMS Microbiology Ecology* 25.1, pp. 1–9. ISSN: 0168-6496. DOI: 10.1111/j.1574-6941.1998.tb00455.x.

McManus, Patricia S. et al. (2002). "ANTIBIOTIC USE IN PLANT AGRICULTURE". In: *Annual Review of Phytopathology* 40.1, pp. 443–465. DOI: 10.1146/annurev.phyto.40.120301.093927.

Meister, M. and H. C. Berg (1987). "The stall torque of the bacterial flagellar motor." In: *Biophys J* 52.3, pp. 413–419. ISSN: 0006-3495. URL: http://www.ncbi.nlm.nih.gov/pmc/articles/PMC1330006/.

Mitchell, PETER (1961). "Coupling of Phosphorylation to Electron and Hydrogen Transfer by a Chemi-Osmotic type of Mechanism". In: *Nature* 191, 144 EP –.

Morf, W.E. (1981). *The Principles of Ion-selective Electrodes and of Membrane Transport*. Studies in analytical chemistry. New York. ISBN: 9780444419415. URL: https://books.google.co.uk/books?id=2ZwRAQAAIAAJ.

Mukamolova, Galina V. et al. (2003). "Adoption of the transiently non-culturable state — a bacterial survival strategy?" In: vol. 47. Advances in Microbial Physiology. Academic Press, pp. 65 –129. DOI: https://doi.org/10.1016/S0065-2911(03)47002-1.

Neher, Erwin and Bert Sakmann (1976). "Single-channel currents recorded from membrane of denervated frog muscle fibres". In: *Nature* 260, p. 799. URL: http://dx.doi.org/10.1038/260799a0.

Neidhardt, F. C., P. L. Bloch, and D. F. Smith (1974). "Culture medium for enterobacteria". In: *Journal of bacteriology* 119.3, pp. 736–747. ISSN: 0021-9193.

Neidhardt, Frederick C. (Frederick Carl), Moselio Schaechter, and John L Ingraham (1990). *Physiology of the bacterial cell : a molecular approach*. Sunderland, Mass. : Sinauer Associates. ISBN: 0878936084 (alk. paper).

Nelson, P. (2003). *Biological Physics (Updated Edition)*. W. H. Freeman. Chap. 11, "409–413". ISBN: 9781429280754. URL: https://books.google.co.uk/books?id=85NymKCGa8kC.

Nicholls, DG and SJ Ferguson (2002). *Bionergetics 3*. Academic Press.

Nichols, Wright W. (2017). "Modeling the Kinetics of the Permeation of Antibacterial Agents into Growing Bacteria and Its Interplay with Efflux".

In: *Antimicrobial Agents and Chemotherapy* 61.10. ISSN: 0066-4804. DOI: 10.1128/AAC.02576-16.

Nicoloff, Hervé et al. (2019). "The high prevalence of antibiotic heteroresistance in pathogenic bacteria is mainly caused by gene amplification". In: *Nature Microbiology* 4.3, pp. 504–514. ISSN: 2058-5276. DOI: 10.1038/s41564-018-0342-0.

Nikaido, Hiroshi and Yumiko Takatsuka (2009). "Mechanisms of RND multidrug efflux pumps". In: *Biochim Biophys Acta* 1794.5, pp. 769–781. ISSN: 0006-3002. DOI: 10.1016/j.bbapap.2008.10.004. URL: https://www.ncbi.nlm.nih.gov/pubmed/19026770.

Niven, Gordon W. et al. (2008). "Influence of environmental stress on distributions of times to first division in Escherichia coli populations, as determined by digital-image analysis of individual cells". In: *Applied and environmental microbiology* 74.12, pp. 3757–3763. ISSN: 1098-5336. DOI: 10.1128/AEM.02551-07.

Orelle, Cédric et al. (2018). "A multidrug ABC transporter with a taste for GTP". In: *Scientific reports* 8.1, pp. 2309–2309. ISSN: 2045-2322. DOI: 10.1038/s41598-018-20558-z.

Orman, Mehmet A. and Mark P. Brynildsen (2013). "Dormancy Is Not Necessary or Sufficient for Bacterial Persistence". In: *Antimicrobial Agents and Chemotherapy* 57.7, pp. 3230–3239. ISSN: 0066-4804. DOI: 10.1128/AAC.00243-13.

Oró, J. and A.P. Kimball (1961). "Synthesis of purines under possible primitive earth conditions. I. Adenine from hydrogen cyanide". In: *Archives of Biochemistry and Biophysics* 94.2, pp. 217 –227. ISSN: 0003-9861. DOI: https://doi.org/10.1016/0003-9861(61)90033-9.

Otsu, N. (1979). "A Threshold Selection Method from Gray-Level Histograms". In: *IEEE Transactions on Systems, Man, and Cybernetics* 9.1, pp. 62–66. ISSN: 0018-9472. DOI: 10.1109/TSMC.1979.4310076.

Page, Rebecca and Wolfgang Peti (2016). "Toxin-antitoxin systems in bacterial growth arrest and persistence". In: *Nature Chemical Biology* 12, 208 EP –.

Pao, Stephanie S., Ian T. Paulsen, and Milton H. Saier (1998). "Major Facilitator Superfamily". In: *Microbiology and Molecular Biology Reviews* 62.1, pp. 1–34. ISSN: 1092-2172.

Papanastasiou, Malvina et al. (2013). "The Escherichia coli peripheral inner membrane proteome". In: *Molecular & cellular proteomics : MCP* 12.3, pp. 599–610. ISSN: 1535-9484. DOI: 10.1074/mcp.M112.024711.

Parry, Bradley R. et al. (2014). "The bacterial cytoplasm has glass-like properties and is fluidized by metabolic activity". In: *Cell* 156.1-2, pp. 183–194. ISSN: 1097-4172. DOI: 10.1016/j.cell.2013.11.028.

Patterson, George H. and Jennifer Lippincott-Schwartz (2002). "A Photoactivatable GFP for Selective Photolabeling of Proteins and Cells". In: *Science* 297.5588, pp. 1873–1877. ISSN: 0036-8075. DOI: 10.1126/science.1074952.

Perry, Thomas O. (1971). "Dormancy of Trees in Winter". In: *Science* 171.3966, pp. 29–36. ISSN: 0036-8075. DOI: 10.1126/science.171.3966.29.

Petersen, Carsten and Lisbeth Birk Møller (2000). "Invariance of the Nucleoside Triphosphate Pools ofEscherichia coli with Growth Rate". In: *Journal of Biological Chemistry* 275.6, pp. 3931–3935. DOI: 10.1074/jbc.275.6.3931.

Pilizota, Teuta and Joshua W. Shaevitz (2012). "Fast, multiphase volume adaptation to hyperosmotic shock by Escherichia coli". In: *PloS one* 7.4, e35205–e35205. ISSN: 1932-6203. DOI: 10.1371/journal.pone.0035205.

Pin, Carmen and József Baranyi (2008). "Single-cell and population lag times as a function of cell age". In: *Applied and environmental microbiology* 74.8, pp. 2534–2536. ISSN: 1098-5336. DOI: 10.1128/AEM.02402-07.

Prachayasittikul, Virapong et al. (2007). "EDTA-induced Membrane Fluidization and Destabilization: Biophysical Studies on Artificial Lipid Membranes". In: *Acta Biochimica et Biophysica Sinica* 39.11, pp. 901–913. ISSN: 1745-7270. DOI: 10.1111/j.1745-7270.2007.00350.x. eprint: http://oup.prod.sis.lan/abbs/article-pdf/39/11/901/1076/39-11-901.pdf. URL: https://doi.org/10.1111/j.1745-7270.2007.00350.x.

Prebble, John N. (2001). "The Philosophical Origins of Mitchell's Chemiosmotic Concepts". In: *Journal of the History of Biology* 34.3, pp. 433–460. ISSN: 1573-0387. DOI: 10.1023/A:1012946715673.

Prindle, Arthur et al. (2015). "Ion channels enable electrical communication in bacterial communities". In: *Nature* 527.7576, pp. 59–63. ISSN: 1476-4687. DOI: 10.1038/nature15709.

Pu, Yingying et al. (2016). "Enhanced Efflux Activity Facilitates Drug Tolerance in Dormant Bacterial Cells". In: *Molecular cell* 62.2, pp. 284–294. ISSN: 1097-4164. DOI: 10.1016/j.molcel.2016.03.035.

Raghunandanan, Sajith et al. (2019). "Comparative label-free lipidomic analysis of Mycobacterium tuberculosis during dormancy and reactivation". In: *Scientific reports* 9.1, pp. 3660–3660. ISSN: 2045-2322. DOI: 10.1038/s41598-019-40051-5.

Rajendran, Megha et al. (2016). "Imaging Adenosine Triphosphate (ATP)". In: *The Biological bulletin* 231.1, pp. 73–84. ISSN: 1939-8697. DOI: 10.1086/689592.

Ramisetty, Bhaskar C. M. et al. (2016). "What Is the Link between Stringent Response, Endoribonuclease Encoding Type II Toxin–Antitoxin Systems and Persistence?" In: *Frontiers in Microbiology* 7, p. 1882. ISSN: 1664-302X. DOI: 10.3389/fmicb.2016.01882.

Ramos, Sofia and H. Ronald Kaback (1977). "The relation between the electrochemical proton gradient and active transport in Escherichia coli membrane vesicles". In: *Biochemistry* 16.5, pp. 854–859. DOI: 10.1021/bi00624a007. eprint: https://doi.org/10.1021/bi00624a007. URL: https://doi.org/10.1021/bi00624a007.

Rhoads, D B and W Epstein (1978). "Cation transport in Escherichia coli. IX. Regulation of K transport." In: *The Journal of General Physiology* 72.3, pp. 283–295. ISSN: 0022-1295. DOI: 10.1085/jgp.72.3.283.

Rimmele, Theresa S. and Jean-Yves Chatton (2014). "A novel optical intracellular imaging approach for potassium dynamics in astrocytes". In: *PloS one* 9.10, e109243–e109243. ISSN: 1932-6203. DOI: 10.1371/journal.pone.0109243.

Rittershaus, Emily S.C., Seung-Hun Baek, and Christopher M. Sassetti (2013). "The Normalcy of Dormancy: Common Themes in Microbial Quiescence". In: *Cell Host Microbe* 13.6, pp. 643 –651. ISSN: 1931-3128. DOI: https://doi.org/10.1016/j.chom.2013.05.012.

Roberts, R. B. et al. (1955). *Studies of biosynthesis of Escherichia coli. ID - 19562202756*. Studies of biosynthesis of Escherichia coli. 607. Washington, D.C.: Carnegie Institution of Washington. Publ., xiv + 521 pp.

Rondelez, Yannick et al. (2005). "Highly coupled ATP synthesis by F1-ATPase single molecules". In: *Nature* 433.7027, pp. 773–777. ISSN: 1476-4687. DOI: 10.1038/nature03277.

Rosano, Germán L. and Eduardo A. Ceccarelli (2014). "Recombinant protein expression in Escherichia coli: advances and challenges". In: *Frontiers in Microbiology* 5, p. 172. ISSN: 1664-302X. DOI: 10.3389/fmicb.2014.00172.

Rosko, Jerko (2017). "Osmotaxis in Escherichia coli". PhD thesis. University of Edinburgh.

Rosko, Jerko et al. (2017). "Osmotaxis in Escherichia coli through changes in motor speed". In: *Proceedings of the National Academy of Sciences*. ISSN: 0027-8424. DOI: 10.1073/pnas.1620945114.

Russell, James T. (2011). "Imaging calcium signals in vivo: a powerful tool in physiology and pharmacology". In: *British journal of pharmacology* 163.8, pp. 1605–1625. ISSN: 1476-5381. DOI: 10.1111/j.1476-5381.2010.00988.x.

Rybak, S.L., F. Lanni, and R.F. Murphy (1997). "Theoretical considerations on the role of membrane potential in the regulation of endosomal pH". In: *Biophysical Journal* 73.2, pp. 674 –687. ISSN: 0006-3495. DOI: https://doi.org/10.1016/S0006-3495(97)78102-5. URL: http://www.sciencedirect.com/science/article/pii/S0006349597781025.

Ryu, William S., Richard M. Berry, and Howard C. Berg (2000). "Torque-generating units of the flagellar motor of Escherichia coli have a high duty ratio". In: *Nature* 403, p. 444. URL: http://dx.doi.org/10.1038/35000233.

Sakmann, B and E Neher (1984). "Patch Clamp Techniques for Studying Ionic Channels in Excitable Membranes". In: *Annual Review of Physiology* 46.1, pp. 455–472. DOI: 10.1146/annurev.ph.46.030184.002323.

Scharf, Birgit E. et al. (1998). "Control of direction of flagellar rotation in bacterial chemotaxis". In: *Proceedings of the National Academy of Sciences* 95.1, pp. 201–206. ISSN: 0027-8424. DOI: 10.1073/pnas.95.1.201.

Schneider, David A. and Richard L. Gourse (2004). "Relationship between Growth Rate and ATP Concentration in Escherichia coli: A BIOASSAY FOR AVAILABLE CELLULAR ATP". In: *Journal of Biological Chemistry* 279.9, pp. 8262–8268. DOI: 10.1074/jbc.M311996200.

Schulz, Sarah et al. (2013). "A New Type of Na+-Driven ATP Synthase Membrane Rotor with a Two-Carboxylate Ion-Coupling Motif". In: *PLOS Biology* 6, pp. 1–12. DOI: 10.1371/journal.pbio.1001596.

Schwarz, S., C. Kehrenberg, and T.R. Walsh (2001). "Use of antimicrobial agents in veterinary medicine and food animal production". In: *International Journal of Antimicrobial Agents* 17.6, pp. 431 –437. ISSN: 0924-8579. DOI: https://doi.org/10.1016/S0924-8579(01)00297-7.

Scott, Matthew et al. (2010). "Interdependence of Cell Growth and Gene Expression: Origins and Consequences". In: *Science* 330.6007, pp. 1099–1102. ISSN: 0036-8075. DOI: 10.1126/science.1192588.

Scott, Matthew et al. (2014). "Emergence of robust growth laws from optimal regulation of ribosome synthesis". In: *Molecular systems biology* 10.8, pp. 747–747. ISSN: 1744-4292.

Shan, Yue et al. (2017). "ATP-Dependent Persister Formation in Escherichia coli". In: *mBio* 8.1. Ed. by Karen Bush, Helen Zgurskaya, and Eduardo Groisman. DOI: 10.1128/mBio.02267-16.

Shikama, Keiji (1971). "Standard free energy maps for the hydrolysis of ATP as a function of pH, pMg and pCa". In: *Archives of Biochemistry and Biophysics* 147.1, pp. 311 –317. ISSN: 0003-9861. DOI: https://doi.org/10.1016/0003-9861(71)90338-9.

Shinoda, Wataru (2016). "Permeability across lipid membranes". In: *Biochimica et Biophysica Acta (BBA) - Biomembranes* 1858.10, pp. 2254 –2265. ISSN: 0005-2736. DOI: https://doi.org/10.1016/j.bbamem.2016.03.032. URL: http://www.sciencedirect.com/science/article/pii/S0005273616301316.

Sims, Peter J. et al. (1974). "Mechanism by which cyanine dyes measure membrane potential in red blood cells and phosphatidylcholine vesicles". In: *Biochemistry* 13.16, pp. 3315–3330. DOI: 10.1021/bi00713a022. eprint: https://doi.org/10.1021/bi00713a022. URL: https://doi.org/10.1021/bi00713a022.

Slonczewski, J L et al. (1981). "pH homeostasis in Escherichia coli: measurement by 31P nuclear magnetic resonance of methylphosphonate and phosphate". In: *Proceedings of the National Academy of Sciences* 78.10, pp. 6271–6275. ISSN: 0027-8424. DOI: 10.1073/pnas.78.10.6271.

Sowa, Yoshiyuki and Richard M. Berry (2008). "Bacterial flagellar motor". In: *Quarterly Reviews of Biophysics* 41.2, 103–132. DOI: 10.1017/S0033583508004691.

Srivastava, Lalit M. (1973). "Cambial Activity in Trees". In: *Arnoldia* 33.1, pp. 46–66. ISSN: 00042633.

Stock, J B, B Rauch, and S Roseman (1977). "Periplasmic space in Salmonella typhimurium and Escherichia coli." In: *Journal of Biological Chemistry* 252.21, pp. 7850–61. eprint: http://www.jbc.org/content/252/21/7850.full.pdf+html. URL: http://www.jbc.org/content/252/21/7850.abstract.

Strahl, Henrik and Leendert W. Hamoen (2010). "Membrane potential is important for bacterial cell division". In: *Proceedings of the National Academy of Sciences* 107.27, pp. 12281–12286. ISSN: 0027-8424. DOI: 10.1073/pnas.1005485107. eprint: http://www.pnas.org/content/107/27/12281.full.pdf. URL: http://www.pnas.org/content/107/27/12281.

Stubbendieck, Reed M. and Paul D. Straight (2016). "Multifaceted Interfaces of Bacterial Competition". In: *Journal of Bacteriology* 198.16. Ed. by W. Margolin, pp. 2145–2155. ISSN: 0021-9193. DOI: 10.1128/JB.00275-16.

Sulatskaya, Anna I. et al. (2017). "Thioflavin T fluoresces as excimer in highly concentrated aqueous solutions and as monomer being incorporated in amyloid fibrils". In: *Scientific Reports* 7.1, pp. 1–11. ISSN: 20452322. DOI: 10.1038/s41598-017-02237-7.

Svenningsen, Mikkel Skjoldan et al. (2019). "Birth and Resuscitation of (p)ppGpp Induced Antibiotic Tolerant Persister Cells". In: *Scientific Reports* 9.1, p. 6056. ISSN: 2045-2322. DOI: 10.1038/s41598-019-42403-7.

Svoboda, Karel et al. (1993). "Direct observation of kinesin stepping by optical trapping interferometry". In: *Nature* 365, 721 EP –.

Taber, H. W. et al. (1987). "Bacterial uptake of aminoglycoside antibiotics". In: *Microbiological reviews* 51.4, pp. 439–457. ISSN: 0146-0749.

Taheri-Araghi, Sattar et al. (2015). "Cell-Size Control and Homeostasis in Bacteria". In: *Current Biology* 25.3, pp. 385–391. ISSN: 0960-9822. DOI: 10.1016/j.cub.2014.12.009.

Tantama, Mathew, Yin Pun Hung, and Gary Yellen (2011). "Imaging Intracellular pH in Live Cells with a Genetically Encoded Red Fluorescent Protein Sensor". In: *Journal of the American Chemical Society* 133.26, pp. 10034–10037. ISSN: 0002-7863. DOI: 10.1021/ja202902d.

Tantama, Mathew et al. (2013). "Imaging energy status in live cells with a fluorescent biosensor of the intracellular ATP-to-ADP ratio". In: *Nature Communications* 4, 2550 EP –.

Te Winkel, J. Derk et al. (2016). "Analysis of Antimicrobial-Triggered Membrane Depolarization Using Voltage Sensitive Dyes". In: *Frontiers in cell and developmental biology* 4, pp. 29–29. ISSN: 2296-634X. DOI: 10.3389/fcell.2016.00029.

"The value of G for the hydrolysis of ATP" (1972). In: *Biochimica et Biophysica Acta (BBA) - Bioenergetics* 267.2, pp. 275 –290. ISSN: 0005-2728. DOI: https://doi.org/10.1016/0005-2728(72)90116-8.

Tsutsui, Hidekazu et al. (2008). "Improving membrane voltage measurements using FRET with new fluorescent proteins". In: *Nature Methods* 5.8, pp. 683–685. ISSN: 15487091. DOI: 10.1038/nmeth.1235.

Tuomanen, E. et al. (1986). "The rate of killing of Escherichia coli by β-lactam antibiotics is strictly proportional to the rate of bacterial growth". In: *Journal of General Microbiology* 132.5, pp. 1297–1304. ISSN: 00221287.

Turner, Linda, William S. Ryu, and Howard C. Berg (2000). "Real-Time Imaging of Fluorescent Flagellar Filaments". In: *Journal of Bacteriology* 182.10, pp. 2793–2801. ISSN: 0021-9193. DOI: 10.1128/JB.182.10.2793-2801.2000.

Vaara, M. (1992). "Agents that increase the permeability of the outer membrane". In: *Microbiological reviews* 56.3, pp. 395–411. ISSN: 0146-0749. URL: https://www.ncbi.nlm.nih.gov/pubmed/1406489.

Varma, Sameer, Dubravko Sabo, and Susan B. Rempe (2008). "K+/Na+ selectivity in K channels and valinomycin: over-coordination versus cavity-size constraints". In: *Journal of molecular biology* 376.1, pp. 13–22. ISSN: 1089-8638. DOI: 10.1016/j.jmb.2007.11.059.

Vermeulen, Natasha et al. (2008). "The bactericidal effect of ultraviolet and visible light onEscherichia coli". In: 99, pp. 550–6.

Vulin, Clément et al. (2018). "Prolonged bacterial lag time results in small colony variants that represent a sub-population of persisters". In: *Nature Communications* 9.1, p. 4074. ISSN: 2041-1723. DOI: 10.1038/s41467-018-06527-0.

Wang, Liang and Michael J. Wise (2011). "Glycogen with short average chain length enhances bacterial durability". In: *Naturwissenschaften* 98.9, p. 719. ISSN: 1432-1904. DOI: 10.1007/s00114-011-0832-x.

Wang, Yao-Kuan et al. (2019). "Comparison of Escherichia coli surface attachment methods for single-cell, in vivo microscopy". In: *bioRxiv*. DOI: 10.1101/648840. eprint: https://www.biorxiv.org/content/early/

2019/07/25/648840.full.pdf. URL: https://www.biorxiv.org/content/early/2019/07/25/648840.

Wilmaerts, Dorien et al. (2018). "The Persistence-Inducing Toxin HokB Forms Dynamic Pores That Cause ATP Leakage". In: *mBio* 9.4. Ed. by Gisela Storz. DOI: 10.1128/mBio.00744-18.

Wood, Janet M. (2015). "Bacterial responses to osmotic challenges". In: *The Journal of General Physiology* 145.5, pp. 381–388. ISSN: 0022-1295. DOI: 10.1085/jgp.201411296. eprint: http://jgp.rupress.org/content/145/5/381.full.pdf. URL: http://jgp.rupress.org/content/145/5/381.

Wood, Thomas K., Stephen J. Knabel, and Brian W. Kwan (2013). "Bacterial Persister Cell Formation and Dormancy". In: *Applied and Environmental Microbiology* 79.23, pp. 7116–7121. ISSN: 0099-2240. DOI: 10.1128/AEM.02636-13.

Wältermann, Marc and Alexander Steinbüchel (2005). "Neutral lipid bodies in prokaryotes: recent insights into structure, formation, and relationship to eukaryotic lipid depots". In: *Journal of bacteriology* 187.11, pp. 3607–3619. ISSN: 0021-9193. DOI: 10.1128/JB.187.11.3607-3619.2005.

Xu, Yongxian, Peng Zou, and Adam E Cohen (2017). "Voltage imaging with genetically encoded indicators". In: *Current Opinion in Chemical Biology* 39, pp. 1 –10. ISSN: 1367-5931. DOI: https://doi.org/10.1016/j.cbpa.2017.04.005.

Yaginuma, Hideyuki et al. (2014). "Diversity in ATP concentrations in a single bacterial cell population revealed by quantitative single-cell imaging". In: *Scientific Reports* 4, 6522 EP –.

Yip, Tai-Tung and T. William Hutchens (1992). "Immobilized Metal Ion Affinity Chromatography". In: *Practical Protein Chromatography*. Ed. by Andrew Kenney and Susan Fowell. Totowa, NJ: Humana Press, pp. 17–31. ISBN: 978-1-59259-498-6. DOI: 10.1385/0-89603-213-2:17.

Yoshida, Tomoki, Akira Kakizuka, and Hiromi Imamura (2016). "BTeam, a Novel BRET-based Biosensor for the Accurate Quantification of ATP Concentration within Living Cells". In: *Scientific Reports* 6, 39618 EP –.

Zhang, Shanshan et al. (2018). "Small Non-coding RNA RyhB Mediates Persistence to Multiple Antibiotics and Stresses in Uropathogenic Escherichia coli by Reducing Cellular Metabolism". In: *Frontiers in Microbiology* 9, p. 136. ISSN: 1664-302X. DOI: 10.3389/fmicb.2018.00136.

Zhao, Xilin and Karl Drlica (2014). "Reactive oxygen species and the bacterial response to lethal stress". In: *Current opinion in microbiology* 21, pp. 1–6. ISSN: 1879-0364. DOI: 10.1016/j.mib.2014.06.008.

Zilberstein, D et al. (1984). "Escherichia coli intracellular pH, membrane potential, and cell growth." In: *Journal of Bacteriology* 158.1, pp. 246–252. ISSN: 0021-9193.

Zimmermann, U., G. Pilwat, and F. Riemann (1974). "Dielectric breakdown of cell membranes". In: *Biophysical journal* 14.11, pp. 881–899. ISSN: 0006-3495. DOI: 10.1016/S0006-3495(74)85956-4.